Sofia University "Sv. Kliment Ohridski"

P H D T H E S I S

to obtain the title of

Ph.D. in Physics

of the Sofia University "Sv. Kliment Ohridski"
Specialty : THEORETICAL PHYSICS

Analytical and numerical methods for studying astrophysical objects

Denitsa STAICOVA

Thesis Advisor: Plamen FIZIEV

Submitted: January, 2012

Jury :

Prof. D. Sc. Todor MISHONOV	-	Faculty of Physics, Sofia University
Assoc. Prof. Dr. Plamen FIZIEV	-	Faculty of Physics, Sofia University;JINR
Prof. D. Sc. Svetlana PACHEVA	-	INRNE, Bulgarian Academy of Sciences
Assoc. Prof. Dr. Mikhail STOILOV	-	INRNE, Bulgarian Academy of Sciences
Assoc. Prof. Dr. Ludmil HADJIIVANOV	-	INRNE, Bulgarian Academy of Sciences

Analytical and numerical methods for studying astrophysical objects

Abstract:

The main objective of this thesis is study the spectrum of rotating compact massive objects using the linearized perturbation theory developed by Teukolsky.
To achieve this goal, we use the exact analytical solutions of the Teukolsky Angular and Teukolsky Radial Equation, written in terms of confluent Heun functions. Then we impose the appropriate boundary conditions directly on the solutions of those differential equations. The advantages of this new approach is that by working with the exact solutions, one has more control over the parameters of the problem, compared with the various approximate methods.
Using the numerical realization of the confluent Heun functions in the software package MAPLE, we obtain the quasi-normal modes spectrum of electromagnetic and gravitational perturbations in the case of rotating and non-rotating black holes (the gravitational case is studied only in the latter case). We are able to reproduce the calculated trough other methods results, and additionally, we are able to study for the first time the dependence of those numerical results on small changes in the argument of the complex radial variable.
Furthermore, we study the spectrum of primary jets of rotating black holes. This is achieved by imposing new, polynomial condition on the solutions of the Teukolsky angular equation. The so-obtained spectrum is qualitatively different from the quasi-normal spectrum. Using the polinomiality property of the confluent Heun functions, we are able to obtain an analytical formula fitting the numerical results for the two lowest modes with high precision.

Keywords: quasinormal modes, QNM, Schwarzschild metric, Kerr metric, Regge-Wheeler equation, Teukolsky radial equation, Teukolsky angular equation, Heun functions, primary jets, GRB

Dedication

Science is not for the faint hearted. It means hardship, seemingly fruitless efforts, and painful processes, to reach a goal you believe in.

This thesis became possible thanks to many people. First, I want to thank my thesis supervisor Prof. Dr. Plamen Fiziev for everything he did for me. He not only shared with me his knowledge and experience and took me trough the difficulties and the pitfalls in science, but also he helped me in a moment when my life was in real danger. I could hardly express my gratitude to him, for his reaction during the incident in Russia, and also for his patience during my recovery and subsequent treatment. For me it's a real honor and inspiration to know and work with a first-class scientist and human like Plamen.

When it comes to the incident in Russia, I must thank all the doctors who looked after me and thanks to whom I am alive and well – most notably Dr. Oleg Durov and the entire team in Russia, but also the people from JINR (or anyone else) who contributed to my treatment. Also I thank Dr. Karzhina, and Dr. Sanchez and Dr. Quero and the entire team in Madrid, who had the courage to act. Special thanks to the anesthetist who made sure I have one unpleasant memory less.

Back to science, I thank everyone who supported me in my path during those four years. Prof. D.Sc. Ana Proykova and Prof. D.Sc. Nikolay Vitanov for the contracts in which I participated, for helpful discussions as part of the IRC-CoSIM, and for the financial support for my trip to Mexico (GR-19). I thank all my professors at the Faculty of Physics and all colleagues who have supported my development as a scientist and a person. Also I'd like to thank the TCPA Foundation for the financial support.

I want to thank all my friends for the good moments we shared, and also all the people I met on the conferences I participated for the helpful discussions and the unforgettable time, especially in Mexico (GR-19) and Madrid (ERE2011).

Last but not least, I thank my family: Mama, Aunt and my cousin Nikolay, without who nothing would be possible. Because of them, science had its chance. I also thank Juan Carlos for his hospitality, and Clive, for everything he has done for us. I thank my life companion, Vasil (Koki), who was always there for me, no matter what.

I'd like to dedicate this thesis to two people who left us, but whose imprint is still in our lives and who always supported me in my desire to do science.

Grandma, Grandpa, this is for YOU.

Acknowledgments

This thesis was supported by the Foundation "Theoretical and Computational Physics and Astrophysics", by the National Science Fund of Bulgaria under contracts DO-1-872, DO-1-895, DO-02-136, and Sofia University Science Fund, contract 185/26.04.2010.

Contents

Chapter 1

Introduction

1.1 GRB observations – the reality check for the theory

The formation of astrophysical jets is one of the frontiers in our understanding of physics of compact massive objects. Collimated outflows are observed in many types of objects: brown dwarfs, young stars, binary systems ([1]), neutron stars (NS) and active-galactic nuclei (AGN) (for a brief review see [2]), and observational data continue to surprise us with the universality of jet formation in the Universe (for example according to [3], observations surprisingly hint for independence of AGN jet-formation from the type of their host galaxy). Despite the differences in the temporal and dimensional scales and the suggested emission mechanisms of the jets, evidences imply that there is some kind of common process serving as an engine for their formation. The true nature of this engine, however, remains elusive.

An example of the difficulties in front of models of such engine, can be seen in gamma-ray burst (GRB) physics. GRBs are cosmic explosions whose jets are highly collimated ($\theta_{jet} \sim 2^\circ - 5^\circ$), highly variable in time ($\sim$ seconds), extreme in their energy output ($\sim 10^{51} - 10^{56}$ erg) and appearing on different redshifts (currently, up to $z^{obs}_{max} = 8.2$) ([4], [5], [6]). Although there are already several hundred GRBs observed by current missions and a lot of details are well studied, the theory of GRBs remains incomplete.

Currently GRBs are divided into two classes – short and long – based on their duration (with a limit $T_{90} \simeq 2s$). This temporal division seemed to correlate with their origin and spectral characteristics, leading to the theory that short GRBs are likely products of binary mergers of compact objects (black hole (BH) and neutron star (NS) or NS and NS), while long GRBs are outcome of the collapse of massive stars [1]. This clear distinction, however, is questioned by observations of bursts with common for the two classes properties (for latest observation of such GRB: [7] suggesting the existence of an intermediate, third class of GRBs and by statistical analysis suggesting that the two classes are not qualitatively different ([8], [9] and [10]) – both evidences of common producing mechanism for the two classes. Furthermore, the possibility to explain short GRBs by merger of binary systems of BH-NS or NS-NS was recently refuted by the lack of detection of gravitational waves in 22 cases of short GRBs ([11], [12]).

[1] The major evidence for the collapsar model, the connection of long GRBs with supernovae (SN) was confirmed with the observations of GRB 980425/SN 1998bw and GRB060218/SN2006aj – events that started as a GRB and then evolved spectrally into a SN. But the question remains why not every long GRB is accompanied by SN.

The dominating theoretical model in the GRB physics describing the evolution of already formed jet is the "fireball model" introduced by [13]. In this model series of shells of relativistic particles are accelerated by unknown massive object called the "central engine". The observed lightcurve is produced by internal collisions of the shells and by their propagation in the circumburst medium. This model, however, doesn't explain the process behind the formation of the shells or the collimation of the jet.

The discrepancies between this model and the observational data were outlined recently in [14], most important of them – the yet unexplained afterglow decay plateaus (and the sharp decay of the light curve afterwards) and the discovered by the mission SWIFT flares (additional sharp maximums superimposed over the decaying afterglow lightcurve) observed in different epochs of the burst and with different fluences (for detailed study of flares see [15]). Although both plateaus and flares imply energy injections by the central engine, the flares that may appear up to $10^6 s$ after the trigger with fluences sometimes comparable with that of the prompt emission, question the very nature of this energy injections. Different theories and simulations are being explored to explain these problems (for recent studies see [16],[17], [18], [19]), but the obvious conclusion is that we still lack a clear understanding of the central engine of GRB.

Theoretically, the most exploited models of central engines include a Kerr black hole (KBH) in super-radiant mode([20], [21]) – the wave analogue of the Penrose process or the Blandford-Znajek process ([22], [23]) based on electromagnetic extraction of energy from KBH – the electromagnetic analogue of Penrose process. Both processes have their strong and weak sides, but the main problem is that they cannot provide enough energy for the GRB – the Penrose process seems to be not efficient enough (it offers significant acceleration only for already relativistic matter), as shown long time ago by Wald ([24]). This problem is also discussed in [25], who argue that the energy gap between a bound stable orbit around a KBH and an orbit plunging into the ergo region is so big, "energy extraction cannot be achieved unless hydrodynamical forces or superstrong radiation reactions can accelerate fragments to speed more than $0.5c$ during the infall". As for the Blandford-Znajek process which offers a good explanation of the collimation we observe, it requires extremely intensive magnetic fields to accelerates the jets to the energies observed in GRBs (theoretical estimations show that $B \sim 10^{15} \div 10^{16}$ G is needed for a jet with $E \geq 10^{51}$ erg). Even when the magnetic fields are sufficiently strong (as in [26]), numerical simulations imply that the BZ process is not efficient enough ([27]) for the formation of the powerful jets seen in GRBs ([28], Barkov, Komissarov: [29], [30] , [31] , [32], [33]).

Furthermore, the most speculated in the theory GRB engines include a rotating black hole, but the observational data on GRBs do not provide definitive clarification on this assumption for now. The main problem is that we cannot observe the central engine directly. The usual techniques to study its strong gravitational field are not applicable for the GRB case, because of the properties of their physical progenitors and their highly non-trivial behavior:

1) We are not able to observe the motion of objects in vicinity of the very central engine of GRB.

2) Instead of quite phase after the hypothetical formation of the KBH, we observe late time engine activity (flares) which is hardly compatible with the KBH model.

3) The visible jets are formed at distance of 20-100 event horizon radii ([34]) where one cannot distinguish the exterior fields of a Kerr black hole from the exterior field of another rotating massive compact matter object solely by measuring the parameters of the metric – M and a (for a detailed discussion see [35], [36]).

In this situation, the only way to find the true nature of the physical object behind the central engine is to study the spectra of perturbations of the Kerr metric. Different types of central engines are described trough different boundary conditions and different boundary conditions generate different spectra specific for the object. Thus finding appropriate spectra to fit our observations enables us to uncover the true nature of the central engine. Similar method to discover the BH horizon was proposed for the first time in [37], and studied more recently in [38], [39], [40], [41]. In present article we give a theoretical basis for application of the same idea for studying the nature of central engine of GRBs based on the spectra of their jets. ([35]).

The study of the spectra of some types of perturbations of rotating black holes has already serious theoretical and numerical basis, particularly concerning the quasi-normal modes (QNM) of a black hole. The QNM case examines linearized perturbations of a Kerr metric described by the Teukolsky angular and radial equations (TAE and TRE accordingly)[2] with boundary condition as follows:

A. Boundary condition on the solutions to the TRE: only ingoing waves in the horizon, only outgoing waves to radial infinity – the so called *black hole boundary condition* (BHBC).

B. Regularity condition is usually imposed on the solutions to the TAE (see in [42] and also in [43]).

The complex frequencies obtained in the case of QNM are the solutions of the eigenvalue problem corresponding to these boundary conditions, they represent the "ringing" which governs the behavior of the black hole in late epochs and they depend only on the two metric parameters (M and a). A major technical difficulty when searching for QNM is that one solves connected problem with two complex spectral parameters. This was first done by [44] and later developed trough the mechanism of continued fractions by [45].

1.2 The ringing of the black holes

The study of the quasi-normal modes (QNMs) of a black hole (BH) has long history ([46, 47, 48, 25, 49, 42, 50, 51, 52, 53, 54, 55, 56, 37, 43, 45, 57, 58, 59, 60, 61, 62, 63, 64, 65, 66, 67, 68, 69, 70]). The case of electromagnetic (EM) perturbations,

[2]TAE and TRE will be discussed in more details in chapter "Perturbation theory"

however, has been often ignored because of their perceived irrelevance to the problem of finding gravitational waves. The reasons behind this are that:

1. The expected luminosity of the gravitational output in the most often studied process of BH binary merger is much bigger than the electromagnetic one ([71]).

2. The EM waves strongly interact with the surrounding medium. This may lead to essential deviation of the observed spectrum from the one expected from the no-hair theorem and it makes the object's fingerprint harder to detect.

3. Most importantly, because of this interaction, the electromagnetic perturbations are strongly absorbed by the interstellar medium, thus making the detection of the signal almost impossible at the predicted low frequencies for the electromagnetic QNMs.

On the other hand, the gravitational waves (GW) interact very weakly with matter and thus they can be detected at big distances, without getting absorbed or scattered, i.e. without obscuring the signature of the body that emitted them. It is, therefore, reasonable to expect that the GW should be much better suited for studying the central engine of astrophysical events, such as gamma-ray bursts (GRBs), while the EM waves should be seriously influenced by its environment.

For now, however, there are no gravitational waves detected. Although both LIGO and VIRGO detectors already work at design sensitivity, both detectors still fail to "see" gravitational waves ([72, 73, 74, 75, 76, 77, 78]). Particularly puzzling is the lack of GW detection from short GRBs ([79, 80]) whose progenitors are expected to emit GWs in the range of sensitivity of the detectors.

The simplest explanation of those negative results may be a new mechanism of generation of short GRBs which in good approximation preserves the spherical symmetry of the process in the central engine and admits only significant dipole radiation. As a result, no significant gravitational waves will be generated during the short GRBs, since the gravitational waves have a quadrupole character. A similar situation is observed in the long GRBs. Such a new hypothesis for short GRBs is supported by the strong observational indications that both types of GRBs may have the same nature and differ only in their time scales ([8, 10]). If so, we may expect that most of the energy release from GRBs is in the form of electromagnetic radiation.

A more traditional point of view is a physical process which yields both electromagnetic and gravitational radiation from GRBs. Actually, the ratio of the energy release in the form of electromagnetic waves and in the form of gravitational waves is still an open problem. Its solution strongly depends on the details of the hypothetical mechanism of GRBs which is still far from being well established. For example, the expected (but not yet observed) energy output in the case of GWs from a BH merger is $\sim 10^{53} erg$, which coincides (up to a factor due to collimation) with the *observed* electromagnetic energy output of GRBs.

While hopes are laid on the Advanced LIGO and Advanced VIRGO which should start operating in the next years, this situation offers a good motivation for optimizing the GW search strategy and understanding better the physics of the GW sources. Particularly, this points to the advantages of studying the EM counterpart

of the GW emission, which can help the localization of the source (improving on the big error box of the GW detector) and also it may give additional clues to the physics of the event ([81, 71]). Numerical simulations already explore the detectability of the EM counterpart in different cases (for the case of supermassive black holes mergers, for example, see [82, 83], for neutron stars mergers [81, 84]). The first results of LIGO and VIRGO searches using such a multimessenger approach were also published [85]. The idea behind those searches (for details, see [86, 85]) is to use the GRBs as the EM counterparts of the GW, since the suspected GRB progenitors (collapsars for long GRBs and binary system mergers of neutron stars and/or black holes for the short GRBs) should emit GWs as well as EM and there is already a well working mechanism for observing the extremely EM luminous GRBs. Although the theoretical results from the multimessenger approach are still being analyzed, the intensive activity in this field shows that the EM counterpart of the GW emission can both facilitate and improve the information obtained from the GW observations.

The discrete spectrum of complex frequencies called QNMs describes only the linearized perturbations of the metric. Hence, they cannot describe completely the dynamics of the process during the early, highly intensive period of those events when the linearized theory is not applicable. On the other hand, it is known from full numerical simulations that it is the QNMs which dominate the late-time evolution of the object response to perturbations [59]. Thus, from an observational point of view, the QNM are important, since we may observe only the tails from the corresponding events, being far from them. This conclusion is supported by the recent numerical observation of two lowest gravitational modes of QNMs in the spectrum of the signal obtained from the full 3d general relativistic head-on collision of non-spinning BH (see [87], and for further information [88]). This result is not isolated – there are number of works in which the QNMs approximate well the signal of full 3d general relativistic simulations of mergers (for example [89, 90, 91, 92, 93] and also the pioneer works discussed in [65]). This clearly implies that studying QNMs can bring new insights to the physics in the processes which include strong-field regime.

Those numerical results also point to another possible use of the QNMs in astrophysical observations. The QNMs correspond to particular boundary conditions characteristic for the object in question, and since in the case of BH the no-hair theorem states that they should depend only on the parameters of the metric (the mass M and the rotation a for the case of Kerr BH), measuring those frequencies observationally can be used to test the nature of the object – a black hole or other compact massive objects like super-spinars (naked singularities), neutron stars, black hole mimickers etc. [94, 95, 40, 41, 96, 97]. It also can constrain additionally the no-hair theorem which was recently put into question in the case of black holes formed as a result from the collapse of rotating neutron stars [98]. An interesting possibility is to find a way to use the damping times of the EM quasi-normal modes for comparison with observations. While the frequencies are subject to interaction with the surrounding matter which can significantly change the spectra, their damping times should be much less prone to deviation. A suggestion for such use can be found in simulations of jet propagation, which imply that the short-scale variability of the

light-curve should be due to the central engine and not to the interaction of the jet with the surrounding medium (see [99] and reference therein).

One more important application of the QNM spectrum can be found in the study of the central engines of the GRBs, whose extreme luminosity($\sim 10^{51} - 10^{53} erg/s$) and peculiar time-variability cannot yet be fully explained in the frames of current models. Even though numerical simulations proved to be capable of describing *some* of the features of the GRBs light curves (for a recent review on GRBs, see [100]), the biggest stumbling stone seems to be the lack of proper understanding of the central engine of the GRBs.

Common ingredients of the existing GRB models include a compact massive object (black hole or a milli-second magnetar) and extreme magnetic field ($\sim 10^{15} G$) which accelerate and collimate the matter via different processes. Although those processes are still an open question for both theory and numerical simulations, the very central engine can be studied approximately by the linearized EM (and also GW if data is available) perturbations of the Kerr metric. When finding the electromagnetic QNMs, one does not care for the origin of the perturbation, but only for its spin and the parameters of the compact massive object. In the idealized EM case, the perturbation is described by free EM waves in vacuum. While the astrophysical black holes are thought to be not charged, they are immersed into EM waves with different energy and origin. The black hole response to such EM perturbations in linear approximation will be then the QNM spectrum defined by the appropriate boundary conditions.

Studying the so obtained electromagnetic spectrum can give important insights into the key parameters of the physics occurring during high-energy events as GRBs. In particular, the electromagnetic QNMs are subject to resonant amplification (the idea of the black hole bomb, [68, 70, 51]) and additionally, it is known from previous evaluations of the spectrum, that they exhibit very low damping in the limit $a \to M$. For the moment, there are no observations of the rotations of the GRB progenitors, but the theoretical expectations are that they should be highly rotating in order to produce jets with such luminosity and collimation. Available observationally measured rotations of astrophysical compact massive objects show that there are many cases of near extremal values thus studying the extremal limit could be relevant to such objects. For example, recent evaluations of the spin parameter of astrophysical black holes give for the spin parameter $a = 0.63, 0.90$ and $a = 0.89, 0.99$ for $M = 1, 0.1 M_{\odot}$ for Sw J1644+57 and Sw J2058+05 respectively (most probable values, see [101]), and also $a > 0.98$ for GRS 1915+105 ([102]) and $a = 0.989$ for MCG-6-30-15 ([103]).

Moreover, because of the relatively good coverage of the GRBs observations, there is a great amount of data, in a wide energy range (from optical to GeV energies) and from different epochs of the bursts which can be used to test the eventual applicability of the QNM spectrum in the late-time epoch of the burst. It may be hard to extract EM QNM spectra from the existing crude GRB spectra since the basic EM QNM frequencies are very low (from a small part of Hz — for supermassive BH to several kHz – for stellar mass BH) and the intensity of the higher EM QNM

may be very low. To the best of our knowledge such attempts haven't been made. A new space mission, which will additionally help the EM observations in the radio range – RadioAstron – will offer unprecedented resolution (up to 1μarcsec) in a wide range of high frequencies (from 0.3GHz to 18-25GHz) accompanied by continuum, polarized and spectral imaging (for details see RadioAstron website [3]). One may hope to use this new mission for a more detailed study of the spectra of EM radiation from the compact objects but its sensitivity is also far from the area of the basic EM QNMs.

Theoretical evaluations of the QNMs, however, are not simple. The linear perturbations of the rotating BHs are described by two second-order linear differential equations: the Teukolsky radial equation (TRE) and the Teukolsky angular equation (TAE) on which specific boundary conditions should be imposed ([53, 43]). Until recently, solving those equations analytically was considered impossible in terms of known functions, so approximations with simpler wave functions were used instead. The resulting system of spectral equations – a connected problem with two complex spectral parameters: the frequency ω and the separation constant E – has been solved using different methods ([65, 60, 63, 69]) with notably the most often used being the method of the continued fraction. This method was adapted by Leaver from the problem of the hydrogen molecule ion in quantum mechanics [45, 57]. While being successful in obtaining the QNMs spectra, Leaver's method has the disadvantage of not being directly connected with the physics of the problem, thus making it harder to further explore the spectra – for example studying its dependence on the choice of the branch cuts of the exact solutions of the radial equation. In addition, one has some specific numerical problems in calculation of particular modes, for example, in calculation of the 9^{th} one in the gravitational case [65, 60, 58].

The analytical solutions of the TRE and the TAE can be written in terms of the confluent Heun function (for $a \neq M$) as done for the first time in [62, 67, 104, 66]. Those functions are the unique local Frobenius solutions of the second-order linear ordinary differential equation of the Fuchsian type [105, 106, 107, 108] with 2 regular singularities ($z = 0, 1$) and one irregular ($z = \infty$) (for details see [67]) and in the MAPLE notation, they are denoted as: HeunC$(\alpha, \beta, \gamma, \delta, \eta, z)$ (normalized to HeunC$(\alpha, \beta, \gamma, \delta, \eta, 0) = 1$). While the theory of the Heun functions is still far from being complete, they are implemented in the software package MAPLE and despite the problems in that numerical realization (see the discussion in [109]), the confluent Heun function was used successfully in a number of works [62, 97, 109, 110]. The advantage of using the analytical solutions is that one can impose the boundary conditions on them *directly* (see [62, 97]), and thus be able to control all the details of the physics of the problem.

[3] http://www.asc.rssi.ru/radioastron

1.3 Plan of the thesis

The goal of this thesis, is to study the spectrum of compact massive objects using the methods of Teukolsky perturbation theory. In order to do that, we use a new approach, namely we use the exact solutions of the differential equations governing the linearized perturbations of the Schwarzschild and Kerr metrics, which are written in terms of confluent Heun functions. Considering the properties of those functions, one can impose different, interesting to the physics, boundary conditions directly on the exact solutions. Such direct approach so far has been used only for the case of QNMs of non-rotating BHs [62] and thus, it is important to check its applicability in the case of EM perturbations of rotating black holes. The latter can be particularly interesting considering the need of better understanding of the current astrophysical observations.

To this end, the following physical situations need to be examined:

1. Gravitational perturbations of non-rotating black holes in the case of quasi-normal boundary conditions.

2. Electromagnetic perturbations of rotating black holes in the cases of quasi-normal boundary conditions.

3. Electromagnetic perturbations of rotating black holes in the cases of primary jets boundary conditions.

Completing that program requires the extensive study of the observational data from GRBs and other astrophysical jets, as well as their theoretical models; the properties of the confluent Heun functions and their numerical realization in Maple; also the already published results on QNMs of rotating and non-rotating BHs, as well as the numerical methods used to obtain them.

From the problems stated above, the question of the EM spectrum of primary jets is studied here for the first time. The other two problems have been extensively analyzed using different, mostly approximate methods, but here, for the first time, they were studied using the *exact* solutions of the differential equations in question. This direct approach offers increased control over the branch cuts of the solutions of the radial equations and the possibility to study their effect on the numerically obtained spectrum.

Additionally, because the perturbations in the quasi-normal case are described by a the two-dimensional transcendental system, which cannot be effectively solved using standard root-finding algorithms, a new method for solving numerically two-dimensional systems featuring the Heun functions needed to be developed. To do so, various root-finding algorithms were reviewed and the new algorithm was tested on both simple test problems and physical problems. Ultimately, it has been applied to the case of gravitational perturbation $s = -2$ of the Schwarzschild metric and also electromagnetic perturbation $s = -1$ of the Kerr metric.

Completing the formulated above program has further applications to physics:

- It will test the applicability of the confluent Heun functions in real physical problems by comparing the numerical results with other already established but approximate methods.
- It also should expand further the understanding of the physics which can be examined in linear approximation and also the limitations of the linear theory.
- The numerically obtained spectrum can then be compared with the observational data and trough it, to confirm or reject the nature of the central engine.

Chapter 2

The confluent Heun equation and its solutions

The Heun functions appear with increasing frequency in modern physics. For example, they arise in the Schrödinger equation with anharmonic potential, in water molecule, in the Stark effect, in different quantum phenomena related with repulsion and attraction of levels, in the theory of lunar motion, in gravitational physics of scalar, spinor, electromagnetic and gravitational waves in Schwarzschild and Kerr metric, in crystalline materials, in three-dimensional waves in atmosphere, in Bethe anzatz systems, in Collogero-Moser-Sutherland systems, e.t.c., just to mention a few. Because of the wide range of their applications ([111],[105])– from quantum mechanics to astrophysics, from lattice systems to economics – they can be considered as the 21^{st} century successors of the hypergeometric functions encountered in relatively simpler physical problems of 20^{th} century.

It is not hard to explain this situation. In natural sciences, in particular, in physics we usually study the different phenomena starting from some equilibrium state. Then we study small deviations from it in linear approximation, and at the end, going far away from the equilibrium we are forced to take into account nonlinear phenomena. It is well known that to describe the wave processes (like those in quantum mechanics), related with some linear phenomenon in classical physics (like classical mechanics), we have to use hypergeometric functions. Therefore these functions were well studied in 19^{th} and 20^{th}centuries and today one can find the corresponding codes in all good computer packages. According to the theorem by Slavyanov [105], if we study nonlinear classical phenomena, described by elliptic functions, or even by the solutions of any of Painlevé type equations, the corresponding wave problems can be solved exactly in terms of the Heun functions. Since the Painlevé equations can be considered as Hamilton ones for a very large class of nonlinear classical problems, one can expect a fast increase in the applications of the Heun functions in physics and other natural sciences of 21^{th} century.

Their mathematical complexity, however, makes working with them a significant challenge both analytically and numerically. The Heun functions are unique local Frobenius solutions of a second-order linear ordinary differential equation of the Fuchsian type [105, 106, 107, 108] which in the general case have 4 regular singular points. Two or more of those regular singularities can coalesce into an irregular singularity leading to differential equations of the confluent type and their solutions: confluent Heun function, biconfluent Heun function, double confluent Heun function and triconfluent Heun function. The Heun functions generalize the hypergeometric

function (and also include the Lamé function, Mathieu function and the spheroidal wave functions [105, 108]) and some of their uses can be found in [105] and also in the more recent [112]. Clearly, the Heun functions will be encountered more and more in modern physics, hence, there is a need of better understanding of those functions and new, more adequate algorithms working with them.

Despite the growing number of articles which use equations from the Heun type and their solutions, the theory of those functions is far from complete. There are some analytical works on the Heun functions, but they were largely neglected until recently. Some recent progress can be found in [104], but as a whole there are many gaps in our knowledge of those functions. Particularly, the connection problem for the Heun functions is not solved – one cannot connect two local solutions at different singular points using known constant coefficients ([105]). Another example of a serious gap in the general theory of the Heun functions is the absence of integral representations analogous to the one for the hypergeometric functions.

Numerically, the only software package currently able to work with the Heun functions is MAPLE. Alternative ways for evaluations of those functions do not exist (to the best of our knowledge) and there are no known projects aiming to change this situation, an admittedly immense task by itself. This means that the use of the Heun functions is limited to the routines hidden in the kernel of MAPLE, which the user cannot change or improve – a situation that makes understanding the numerical problems or avoiding them adequately very difficult. On the positive side, those routines were found by the team to work well enough in many cases (an example of the match between theory and numerical results will be demonstrated in section 4.3). Yet, there are some peculiarities – there are values of the parameters where the routines break down leading to infinities or to numerical errors. The situation with the derivatives of the Heun functions in MAPLE is even worst – for some values they simply do not work, for example outside the domain $|z| < 1$, where their precision is much lower than that of the Heun function itself. Also, in some cases there are no convenient power-series representations and then the Heun functions are evaluated in MAPLE using numerical integration. Therefore the procedure goes slowly in the complex domain (compared to the hypergeometric function) which means that the convergence of the root-finding algorithm is essential when one solves equations including Heun's functions.

Despite all the numerical set-backs, the Heun functions clearly offer many opportunities to modern physics. They occur in the problem of quasi-normal modes (QNM) of rotating and non-rotating black holes, which is to some extent the gravity analogue of the problem of the hydrogen atom. Finding the QNMs is critical to understanding observational data from gravitational wave detectors and proving or refuting the black holes existence. In this case, one has to solve a two-dimensional connected spectral problem with two complex equations in each of which one encounters the confluent Heun functions. The solution of this system is highly non-trivial and the root-finding algorithm we used is discussed in the Appendix: "Numerical methods".

In the current chapter, we introduce the confluent Heun functions and some

of their most important properties, which have been used to obtain the numerical results presented in this work.

2.1 The Confluent Heun Equation

Explicitly, the confluent Heun equation (CHE) is a second-order linear ordinary differential equation of the Fuchsian type [105, 106, 107, 108] with 2 regular singularities ($z = 0, 1$) and one irregular ($z = \infty$) (for details see [67]):

$$\frac{d^2}{dz^2}H(z) + \left(\alpha + \frac{\beta+1}{z} + \frac{\gamma+1}{z-1}\right)\frac{d}{dz}H(z) + \left(\frac{\mu}{z} + \frac{\nu}{z-1}\right)H(z) = 0. \quad (2.1)$$

Its unique local Frobenius solutions, regular in the vicinity of the regular singular point $z = 0$ and normalized to be equal to 1 at this point ($\mathrm{HeunC}(\alpha, \beta, \gamma, \delta, \eta, 0) = 1$) are called the confluent Heun functions. For more details, see the monograph [105] and some additional references in [35], [104].

With those functions, one can write the general solution of Eq. (2.1) in MAPLE notation, as:

$$H(z) = C_1\,\mathrm{HeunC}(\alpha, \beta, \gamma, \delta, \eta, z) + C_2\, z^{-\beta}\mathrm{HeunC}(\alpha, -\beta, \gamma, \delta, \eta, z), \quad (2.2)$$

where $\delta = \mu + \nu - \alpha\frac{\beta+\gamma+2}{2}$ and $\eta = \frac{\alpha(\beta+1)}{2} - \mu - \frac{\beta+\gamma+\beta\gamma}{2}$.

Using s-homotopic transformations (such that conserve the canonical form of CHE), one can obtain 16 classes of exact local Frobenius type solutions in the form:

$$H = e^{\sigma_\alpha \frac{\alpha_\pm z_\pm}{2}} z_\pm^{\sigma_\beta \frac{\beta_\pm}{2}} z_\mp^{\sigma_\gamma \frac{\gamma_\pm}{2}} \mathrm{HeunC}(\sigma_\alpha\alpha_\pm, \sigma_\beta\beta_\pm, \sigma_\gamma\gamma_\pm, \delta_\pm, \eta\pm, z_\pm), \quad (2.3)$$

where $\sigma_\alpha, \sigma_\beta, \sigma_\delta = \pm 1$, and the parameters change as: $\alpha_+, \beta_+, \gamma_+, \delta_+, \eta_+ \to \alpha_-, \beta_-, \gamma_-, \delta_-, \eta_-$ for $z_+ \to z_-$ (more details can be found in [107, 108, 105, 67]).

2.2 Power-series expansion around the regular singularities $z = 0, 1$

In the unit sphere $|z| < 1$, the so defined confluent Heun function is evaluated using the power-series expansion:

$$y(z) = \sum_{\nu\geq 0} c_\nu z^{\nu+\rho}. \quad (2.4)$$

When plugged into the differential equation Eq. (2.1), this expansion gives the following three-term recurrence ([108]):

$$\begin{aligned}
&\rho(\rho+\beta)=0\\
&c_1(\rho+1)(\beta+\rho+1)-c_0(\eta+\frac{\beta}{2}+\frac{1}{2}(\gamma-\alpha)(\beta+1)+\rho(\rho+1+\beta+\gamma-\alpha))=0\\
&c_{\nu+2}C_2-c_{\nu+1}C_1+c_\nu C_0=0,\nu\geq 0 \qquad (2.5)\\
&\text{where}\quad C_2=(\rho+\nu)(\rho+\nu+\beta),\quad C_0=(\rho+\nu)\alpha+\delta+\frac{1}{2}\alpha(\beta+\gamma+2)\\
&C_1=\eta+\frac{\beta}{2}+\frac{1}{2}(\gamma-\alpha)(\beta+1)+(\rho+\nu+1)(\rho+\nu+2+\beta+\gamma-\alpha).
\end{aligned}$$

If β is not integer, then one denotes with $\text{HeunC}(\alpha,\beta,\gamma,\eta,z)$ the solution corresponding to $\rho=0$ and for which $c_0=1$. For $\rho=-\beta$, one obtains another linearly independent solution of the same equation, namely $z^{-\beta}\text{HeunC}(\alpha,-\beta,\gamma,\delta,\eta,z)$. Using those two solutions, one obtains the general solution of the CHE – Eq.(2.2).

This expansion can be used, however, only in the unit-circle $|z|<1$. Outside of this circle, there is no appropriate convergent series expansion and thus in MAPLE, the confluent Heun functions are evaluated with numerical integration in the complex z-plane, which additionally slows down their evaluation.

2.3 Asymptotics at $z\to\infty$

Even though in our work, we will use the numerical realization of the confluent Heun function in MAPLE, the asymptotics at infinity is important for imposing the boundary conditions defining the physics of the problem.

Again following [108], one finds that the asymptotics is:

$$H^1(\alpha,\beta,\gamma,\eta,z)\sim z^{-(\frac{\beta+\gamma+2}{2}+\frac{\delta}{\alpha})}\sum_{\nu\geq 0}\frac{a_\nu(\alpha)}{z^\nu} \qquad (2.6)$$

$$H^2(\alpha,\beta,\gamma,\eta,z)\sim z^{-(\frac{\beta+\gamma+2}{2}-\frac{\delta}{\alpha})}e^{-\alpha z}\sum_{\nu\geq 0}\frac{e_\nu(\alpha)}{z^\nu} \qquad (2.7)$$

in the domain $-\pi-arg(\alpha+\eta)\leq arg(z)\leq\pi-arg(\alpha-\eta)$.

The coefficients $a_\nu(\alpha)$ and $e_\nu(\alpha)$ are given by the recurrence:

$$\begin{aligned}
&a_0=1,-\alpha a_1+m(\alpha)a_0=0\\
&-\alpha(\nu+2)a_{\nu+2}+(m(\alpha)+(\nu+1)\left(\nu+2+\alpha+\frac{2\delta}{\alpha}\right)a_{\nu+1}+\\
&\left(\frac{\beta^2}{4}-\left(\frac{\gamma+2}{2}+\frac{\delta}{\alpha}\right)^2+\nu(\nu+1)-\nu\left(\frac{2\delta}{\alpha}+\gamma+1\right)\right)a_\nu=0,\nu\geq 0
\end{aligned}$$

where $e_\nu(\alpha)=a_\nu(-\alpha),\nu\geq 0$ and $m(\alpha)=\eta-\frac{\gamma^2}{4}-\frac{\beta^2}{4}+\frac{\alpha}{2}(\gamma+1)+\frac{\delta}{\alpha}(\frac{\delta}{\alpha}+1+\alpha)$.

In this thesis, unless stated otherwise, we will use only the first term of this power-series asymptotics (≈ 1).

2.4 Polynomial solutions – δ_N and Δ_{N+1} conditions

For certain values of the parameters $\alpha, \beta, \gamma, \delta, \eta$, the confluent Heun function reduces to a polynomial. Since this significantly simplifies the evaluation of the function and also it imposes specific boundary conditions, corresponding to a physical situation which may describe the astrophysical jets, this case is of particular importance to our studies.

The polynomiality condition reads:

$$\begin{aligned} &\frac{\delta}{\alpha} + \frac{\beta+\gamma}{2} + N + 1 = 0, \\ &\Delta_{N+1}(\mu) = 0. \end{aligned} \tag{2.8}$$

Here, the integer $N \geq 0$ is the degree of the polynomial and $\Delta_{N+1}(\mu)$ is the three-diagonal determinant specified in [35], [104]:

$$\begin{vmatrix} \mu-q_1 & 1(1+\beta) & 0 & \dots & 0 & 0 & 0 \\ N\alpha & \mu-q_2+1\alpha & 2(2+\beta) & \dots & 0 & 0 & 0 \\ 0 & (N-1)\alpha & \mu-q_3+2\alpha & \dots & 0 & 0 & 0 \\ \vdots & \vdots & \vdots & \ddots & \vdots & \vdots & \vdots \\ 0 & 0 & 0 & \dots & \mu-q_{N-1}+(N-2)\alpha & (N-1)(N-1+\beta) & 0 \\ 0 & 0 & 0 & \dots & 2\alpha & \mu-q_N+(N-1)\alpha & N(N+\beta) \\ 0 & 0 & 0 & \dots & 0 & 1\alpha & \mu-q_{N+1}+N\alpha \end{vmatrix} \tag{2.9}$$

where $q_n = (n-1)(n+\beta+\gamma)$ and the parameter μ comes from the self-adjoint form of the Heun equation:

$$e^{-\alpha z} z^{-\beta} (z-1)^{-\gamma} \frac{d}{dz}\left(e^{\alpha z} z^{1+\beta} (z-1)^{1+\gamma} \frac{dH(z)}{dz} \right) + \alpha \left(\frac{\delta}{\alpha} + \frac{\beta+\gamma}{2} + 1 \right) zH(z) = \mu H(z).$$

The first condition will be called δ_N-condition and it is equivalent to the equation $C_0 = 0$ (Eq. 2.5, for $\rho = 0$ and $\nu = N$). The second condition is equivalent to $c_{\nu+1}(\alpha, \beta, \gamma, \delta, \eta) = 0$. Fulfilling both conditions, means that the power-series expansion is being cut after its N^{th} terms – all the terms with $n > N$ are zero – and thus one obtains a polynomial of a degree N. Note that the name "polynomial" here is used in its wider meaning of solutions in the form of finite Taylor series expansion multiplied by elementary functions [35].

Another form of the second polynomial condition $\Delta_{N+1}(\mu) = 0$ can be found in [104] and it reads $(N+1)! c_{N+1}(\alpha, \beta, \gamma, \delta_N, \eta)$, where c_{N+1} are the terms in the series expansion Eq. (2.4).

2.5 Derivatives of the confluent Heun function

The formulas for the series expansion and the asymptotics of the confluent Heun function were obtained in the 70s and can be found in [107, 108, 105], along with other properties. A significant leap in the theory of the confluent Heun functions occurred recently, in the works by Fiziev [104]. One important novelty is the analytical relation obtained in [104] which allows the evaluation of the derivative of the

confluent Heun function in some specific cases without relying on the problematic in MAPLE numerical differentiation.

This formula can be used for parameters of the confluent Heun function obeying the δ_N condition:

$$\frac{\delta}{\alpha}+\frac{\beta+\gamma}{2}+N+1=0$$

. According to [104], if one considers two unique solutions of the Heun's differential equation, which are regular at $z=0$ and normalized to 1 at that point, then those two solutions are the confluent Heun functions: $\mathrm{HeunC}(\alpha,\beta,\gamma,\delta_N,\eta,z)$ and $\mathrm{HeunC}(\alpha(N{+}1),\beta(N{+}1),\gamma(N{+}1),\delta_N(N{+}1),\eta(N{+}1),z)$. For those two functions, one has the novel relation:

$$\begin{aligned}&\frac{d^{N+1}}{dz^{N+1}}\mathrm{HeunC}(\alpha,\beta,\gamma,\delta_N,\eta,z)=(N+1)!v_{N+1}(\alpha,\beta,\gamma,\delta_N,\eta)\times\\&\times\mathrm{HeunC}(\alpha(N+1),\beta(N+1),\gamma(N+1),\delta_N(N+1),\eta(N+1),z)\end{aligned}\tag{2.10}$$

Here, v_{N+1} is the (N+1)-th coefficient in the Taylor series expansion 2.4 and $\delta_N=-\alpha((\beta+\gamma)/2+N+1)$. We have also used the transformation $\{\alpha,\beta,\gamma,\delta_N,\eta\}\rightarrow\{\alpha(n),\beta(n),\gamma(n),\delta_N(n),\eta(n)\}$ and $\alpha(n)=\alpha,\beta(n)=\beta+n,\gamma(n)=\gamma+n,\delta(n)=\delta+n\alpha,\eta(n)=\eta+\frac{n}{2}(n-\alpha+\beta+\gamma)$ for $n=N+1$.

Clearly, this relation can be used only for certain specific values of the parameters $\alpha,\beta,\gamma,\delta,\eta$ and thus one cannot avoid the numerical evaluation of the derivative in the general case. Still, since in some cases the functions we deal with fulfill those conditions, it offers a valuable alternative way to evaluate the derivatives and to control the error in the derivative of the confluent Heun function in MAPLE due to numerical differentiation and integration.

Chapter 3

Equations of the perturbation theory and their solutions

In this chapter, the differential equations describing the linear perturbations of rotating and non-rotating black holes will be introduced. The boundary conditions used to fix the physics of the problem will be discussed in the chapter "Numerical results".

3.1 Rotating black holes

A compact massive rotating body such as rotating black hole, is described by the Kerr metric ([113]): exactly when the object is a black hole, and approximately – for other objects. This approximation differs for different objects – for example, it is known that the Kerr metric describes well slowly rotating neutron stars (to second order of the angular moment). For rapidly rotating neutron stars, the two metrics differ considerably at higher order in a (or J), since their multipole moments differ [114]. For example in [115], it is demonstrated that for various equations of state of slowly rotating stars, the quadrupole moment of the Kerr metric already deviates from the metric of the star. According to [116], this happens for neutron stars rotating with spin frequencies above 400Hz.

In terms of the lowest order multipole moments (M and $J = aM$), however, the Kerr metric can describe any rotating compact massive body[1] and thus it can be used to study approximately various astrophysical objects. Furthermore, by comparing the observationally measured quadrupole moment of such body with the theoretically expected for a KBH ($Q = -J^2/M = -a^2$) along with M and J, one can test the yet not-proved no-hair theorem for the KBH, which requires that the only stationary, axisymmetric, asymptotically flat non-charged vacuum black hole solution to the Einstein field equations – the Kerr metric is described completely by two parameters – a and M.

[1] Here, we discuss the vacuum solution in the region outside the event horizon. The search for interior Kerr solution with equation of state describing realistic source which can be connected with the exterior Kerr solution is still ongoing. This, however, doesn't affect the exterior solution discussed above.

3.1.1 The Kerr Metric

In Boyer-Lindquist coordinates, for $c = G = 1$ the Kerr metric is:

$$ds^2 = (1 - 2Mr/\Sigma)dt^2 + 4Mar\sin^2(\theta)/\Sigma dt d\phi - (\Sigma/\Delta)dr^2 - \Sigma d\theta^2 - \sin^2(\theta)\left[r^2 + a^2 + 2Ma^2 r\sin(\theta)/\Sigma\right] d\phi^2 \quad (3.1)$$

where $\Delta = r^2 - 2Mr + a^2, \Sigma = r^2 + a^2\cos^2\theta$ and r is the area radius. Here M is the mass of the object and a is a rotational parameter, related with the angular momentum of the object by $a = J/M$ and the Kerr metric depends only on those two parameters – a and M. The monopole moment of this metric is M, a is the dipole moment and all the higher multipole moments are obtained trough $M_l + iJ_l = M(ia)^l$ (the real quantities are the mass moments, the imaginary: the current moments), which is another definition of the no-hair theorem.

For $a < M$, the Kerr metric has two *real* horizons defined by $r_\pm = M \pm \sqrt{M^2 - a^2}$ and in our studies, we focus on the outer region $r > r_+$ which is linearly stable. This definition holds for $a < M$ (KBH). For the Kerr naked singularity (KNS) $a > M$ and $r_\pm$ are complex. When black hole boundary conditions are imposed, for $a < M$ the Kerr metric describes a rotating black hole. The extremal limit is reached when $a = M$ and in this case, $r_+ = r_- = M$. For $a > M$ the Kerr black hole turns into a KNS. In our work, we will discuss only jets from KBH or KNS.

The change of the metric due to the change of the parameter a can be seen also in the change of the topology of ergosurfaces of the Kerr metric (Fig. 3.1). The ergosurfaces are defined by $g_{tt} = -\left(1 - \frac{2Mr}{r^2 + a^2\cos^2(\theta)}\right) = 0$ which gives the stationary limit surface $r_E^\pm$, where $r_E^\pm = M \pm \sqrt{M^2 - a^2\cos(\theta)^2}$. As seen on the Fig. 3.1, for a from $a < M$ to $a > M$ we observe a clear transition form ergosphere to ergotorus. The ergosphere marks the region where no test-object can stand still (since in order to stand still one has to have $g_{tt} > 0$) – it has to rotate with the KBH. Note that $r_E^+ \geq r_+ \geq r_- \geq r_E^-$, which dictates the behavior of the time-variable in those intervals: for $\Delta < 0$ and $g_{tt} < 0$ the radial variable becomes time and the time-variable becomes space-like. For $\Delta > 0$ and $g_{tt} < 0$ (i.e. for $r \in (r_-, r_E^-)$ and $r \in (r_+, r_E^+)$), both r and t are space-variables and the only time variable comes

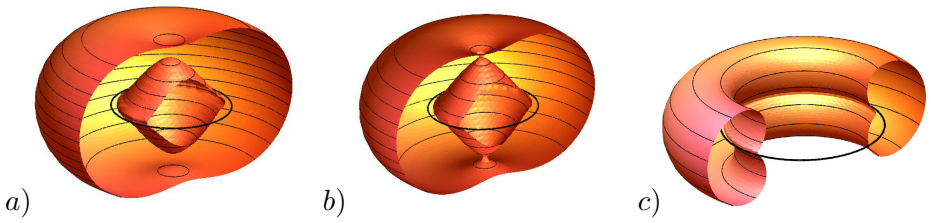

Figure 3.1: A plot of the ergo surfaces for a) KBH: $a < M$, b) extremal case: $a = M$ and c) KNS: $a > M$. One can clearly see the ring singularity of the Kerr metric and the change of topology due to the transition from ergospheres to ergo torus.

from the term $g_{t\phi}$ which leads to the frame-dragging effect: time-like vectors must have non-zero ϕ-component.

From mathematical point of view, it is more natural to work with a dimensionless parameter $b = M/a \in [0, \infty)$. Obviously the point $b = 1$ is a *bifurcation* point. When the bifurcation parameter increases from 0 to ∞, the ergo-torus ($b \in (0, 1)$) bifurcates at the point $b = 1$ to two ergo-spheres ($b = (1, \infty)$). The point $b = 0$ corresponds to the ring singularity. At the point $b = \infty$ the outer ergosphere transforms to Schwarzschild event horizon and the inner ergosphere degenerates to the well-known singularity $r = 0$ of the Schwarzschild metric.

Another feature of the Kerr metric can be seen, following [117], if one considers the 3D surfaces formed by fixing $r = r_c$ and leaving the other coordinates unchanged.By setting in Eq. (3.1), $dr \to 0, r \to r\star$, one obtains for the induced metric:

$$ds^2_{3d} = -dt^2 + (r_c^2 + a^2\cos(\theta)^2)d\theta^2 + (r_c^2 + a^2)\sin(\theta)^2 d\phi^2 + \frac{2M}{r_c}\frac{(dt - a\sin(\theta)^2 d\phi)^2}{1 + a^2\cos(\theta)^2/r_c^2)}. \tag{3.2}$$

Knowing the determinant of the full 4D metric $-\sin^2(\theta)(r^2 + a^2\cos^2(\theta))^2$, one can obtain the determinant of the metric of the 3-surfaces: $-\sin^2(\theta)(r_c^2+a^2\cos(\theta)^2)(r_c^2-2Mr_c+a^2)$. Clearly, unlike the full determinant which remains always negative, in this case, the determinant is negative for $r_c > r_+$ and $r_c < r_-$, indicating that the 3-surfaces are (2+1) dimensional. For $r_c \in (r_-, r_+)$, however, the determinant is positive meaning that there is no dimension corresponding to time for those surfaces. For $r_c = r_-$ and $r_c = r_+$, the determinant is zero, meaning that the corresponding matrix g^{3d}_{ij} is singular for such r. Then, if one defines a 3-vector L^i lying in the 3-surfaces $r = r_\pm$ (and defined only there), that vector will be null (since the scalar product will be $g^{3d}_{ij}L^iL^j = 0$, because of the singular matrix). Then if one promotes this vector to 4-dimensions: $L^i \to L^\alpha(L^t, 0, L^\theta, L^\phi)$ in the (3+1)space time, for $r = r\pm$, one will have $g_{ab}L^aL^b = 0$ which indicates that there is a set of null curves that remain forever on the 3-surfaces $r = r\pm$. The vector field L^α corresponds to the photon "orbits" which never leave the two horizons – the light is trapped there.

3.1.2 Derivation of the Teukolsky Master Equation

The evolution of linear perturbations with different spin ($\mid s \mid = 0, 1/2, 1, 3/2, 2$) on the background of a Kerr metric was pioneered by Teukolsky in the 70s and lead to the famous Teukolsky Master Equation (TME) ([42]):

$$\begin{aligned} L = &\left[\frac{(r^2+a^2)^2}{\Delta} - a^2\sin^2\theta\right]\frac{d^2}{dt^2} + \frac{4Mar}{\Delta}\frac{d^2}{dtd\phi} + \left[\frac{a^2}{\Delta} - \frac{1}{\sin^2\theta}\right]\frac{d^2}{d\phi^2} - \\ &\Delta^{-s}\frac{d}{dr}\left(\Delta^{s+1}\frac{d}{dr}\right) - \frac{1}{\sin(\theta)}\frac{d}{d\theta}\left(\sin\theta\frac{d}{d\theta}\right) - 2s\left[\frac{a(r-M)}{\Delta} - \frac{i\cos\theta}{\sin^2\theta}\right]\frac{d}{d\phi} - \\ &2s\left[\frac{M(r^2-a^2)}{\Delta} - r - ia\cos\theta\right]\frac{d}{dt} + \left(s^2\cot^2\theta - s\right). \end{aligned} \tag{3.3}$$

This differential equation unifies all physically interesting perturbations ${}_s\Psi(t, r, \theta, \phi)$ written in terms Newman-Penrose (NP) scalars and it is able to describe completely multitude of physical phenomena ([49]). The most important spins, in view of the current astrophysical observations are: $s = \pm 1$ describing electromagnetic perturbations and $s = \pm 2$ describing gravitational perturbations[2].

In the derivation of TME below we follow closely Teukolsky ([42, 50, 51]). The Teukolsky Master Equation can be derived from the linearization of the Einstein equations around a known stationary background solution – the Kerr metric (The same procedure, however, has been successfully applied to the Schwarzschild metric as well, rendering the Regge-Wheeler equation and the Zerilli equation). Using the Newman-Penrose scalars, one projects the Einstein equations on convenient tetrads. In the so obtained equations, one finds as variables some of the decoupled components of the tensors of Weyl and Riemann (which coincide in the vacuum case which we consider in this work) or the EM field tensor. It has been proved, however, that those decoupled components describe all the nontrivial properties of the full perturbed field ([118],[119]) .

The decoupled EM components are:

$$\phi_0 = F_{\mu\nu} l^\mu m^\nu, \phi_1 = \frac{1}{2} F_{\mu\nu}(l^\mu n^\nu + m^{*\mu} m^\nu), \phi_2 = F_{\mu\nu} m^{\mu *} n^\nu, \tag{3.4}$$

where $l, n, m, m*$ are the tetrads discussed below and $F_{\mu\nu}$ is the EM field tensor characterized by the complex quantities ϕ_0, ϕ_1, ϕ_2:

$$F_{\mu\nu} = 2[\phi_1(n_{[\mu} l_{\nu]} + m_{[\mu} m^*_{\nu]}) + \phi_2(l_{[\mu} m_{\nu]} + \phi_0(m^*_{[\mu} n_{\nu]}] + c.c.$$

For the gravitational field one obtains:

$$\psi_0 = -C_{\alpha\beta\gamma\delta} l^\alpha m^\beta l^\gamma m^\delta, \quad \psi_4 = -C_{\alpha\beta\gamma\delta} n^\alpha m^{*\beta} n^\gamma m^{*\delta},$$

where $C_{\alpha\beta\gamma\delta}$ are the components of the Weyl tensor.

The method used to linearize the equations of the perturbation differs from the standard one. Because of the complexity of the equations, here, one uses more formal approach consisting of adding to the non-perturbed metric $g_{\mu\nu}$ a perturbed part, i.e. $g_{\mu\nu} = g^A_{\mu\nu} + h^B_{\mu\nu}$ (where the indexes A and B correspond to the background and perturbed part of the metric, respectively). This procedure is performed on *all* the quantities in the equations and then the linear field equations are obtained by keeping only the terms to first order in $h^B_{\mu\nu}$.

The complicated algebra involved can be somewhat simplified by the use of the Newman-Penrose formalism ([120]). In this formalism one introduces four null vectors: n, l, m and $m*$ (where n, l are real and m and $m*$ – complex conjugated one to the other). All the tensors are projected on the so-defined tetrad. The full system of equation is a system of differential equations of first order connecting the tetrads, the spin coefficients, the Weyl tensor and the scalar curvature. Then, one

[2]The sign of spin-weight parameter s is defined by the field quantities Ψ satisfying the equation $L\Psi = 4\pi\Sigma T$ for different values of the source term T. For more details, see [49].

applies the formal linearization procedure on all the quantities described above and ignores all the quantities of order higher than first with respect to the index B. The detailed derivation of these equations can be found [42], here we only demonstrate some of the steps needed to get to the TME.

The Einstein-Maxwell Equations on the NP tetrad

The derivation is valid for every vacuum metric of the type D (Petrov classification[3]). If one choses the vectors l and n of the non-perturbed tetrad along the repeated principal null directions of the Weyl tensor, some of the background quantities vanish (for notations[4], see [120]):

$$\psi_0^A = \psi_1^A = \psi_4^A = \kappa^A = \sigma^A = \nu^A = \lambda^A = 0 \tag{3.5}$$

Then, one considers the following 3 non-vacuum NP equations ([42]):

$$(\delta^* - 4\alpha + \pi)\psi_0 - (D - 4\rho - 2\varepsilon)\psi_1 - 3\kappa\psi_2 = (\delta + \pi^* - 2\alpha^* - 2\beta)\Phi_{00} \tag{3.6}$$

$$(\Delta - 4\gamma + \mu)\psi_0 - (\delta - 4\tau - 2\beta)\psi_1 - 3\sigma\psi_2 = \tag{3.7}$$

$$= (\delta + 2\pi^* - 2\beta)\Phi_{01} - (D - 2\varepsilon - 2\varepsilon^*)\Phi_{02} - \lambda^*\Phi_{00} + 2\sigma\Phi_{11} - 2\kappa\Phi_{12} \tag{3.8}$$

$$(D - \rho - \rho^* - 3\varepsilon + \varepsilon^*)\sigma - (\delta - \tau + \pi^2 - \alpha^* - 3\beta)\kappa - \psi_0 = 0 \tag{3.9}$$

where:

$$\Phi_{00} = -\frac{1}{2}R_{\mu\nu}l^\mu l^\nu = 4\pi T_{\mu\nu}l^\mu l^\nu = 4\pi T_{ll},\ \Phi_{01} = -\frac{1}{2}R_{\mu\nu}l^\mu m^\nu = 4\pi T_{lm},\ \Phi_{02} = 4\pi T_{mm} \tag{3.10}$$

are the Ricci tensor terms given by the Einstein field equations for $R_{\mu\nu}$ and $T_{\mu\nu}$ – the Ricci tensor and the stress-energy tensor, respectively. In vacuum, some of the quantities vanish ($\psi_o^A, \psi_1^A, \sigma^A, \kappa^A$ and the Φ^As) and the next step is to expand all the values in the two indexes (A and B) and to remove all the terms where the index A repeats twice (since the background metric satisfies the field equations) and also all the terms where the index B repeats twice (we linearize). Accounting also for all the vanishing terms and that the background metric satisfies $D\psi_2 = 2\rho\psi_2$, $\delta\psi_2 = 3\tau\psi_2$, one should eliminate ψ_1^B from the first two equations. This is done by using the commutation relation, which is true for any D-type metric ([120]):

$$[D-(p+1)\varepsilon+\varepsilon^*+q\rho-\rho^*](\delta-p\beta+q\tau)-[\delta-(p+1)\beta-\alpha^*+\pi^*+q\tau](D-p\varepsilon+q\rho) = 0, \tag{3.11}$$

where p, q are any two constants. Then if one multiplies with $(D-3\varepsilon+\varepsilon^*-4\rho-\rho^*)$ the equation obtained from Eq. (3.8) and with $(\delta+\pi^*-\alpha^*-3\beta-4\tau)$ the equation

[3] The Petrov classification describes the symmetries of the Weyl tensor on certain Lorentzian manifold at each point of the space-time trough the eigenbivectors of the Weyl tensor [121]. The eigenbivector is defined as $C_{abcd}F^{cd} = \lambda F_{ab}$, where λ is the eigenvalue, F^{ab} is the eigenbivector and the Weyl tensor C_{abcd} is considered as the linear map: $H_{ab} = C_{abcd}H^{cd}$. For metric of the type D, there are two double principal null directions (two linearly independent eigenbivectors), which means that the Weyl tensor is specified by only one complex scalar.

[4] $D, \Delta, \delta, \delta^*$ are the tetrad vectors as differential operators and $\kappa = \Gamma_{mll}, \tau = \Gamma_{mln}, \sigma = \Gamma_{mlm}, \rho = \Gamma_{mlm^*}, \pi = \Gamma_{nm^*l}, \nu = \Gamma_{nm^*n}, \lambda = \Gamma_{nm^*m^*}, \mu = \Gamma_{nm^*m}, \varepsilon + \varepsilon^* = \Gamma_{nll}, \varepsilon - \varepsilon^* = \Gamma_{mm^*l}, \gamma + \gamma^* = \Gamma_{nln}, \gamma - \gamma^* = \Gamma_{mm^*n}, \alpha^* + \beta = \Gamma_{nlm}, \beta - \alpha^* = \Gamma_{mm^*m}$

obtained from Eq. (3.6) and one subtracts the one equation from the other, then for $p = 2, q = -4$, one can eliminate σ^B and κ^B.

Thus the equation becomes:

$$[(D-3\varepsilon+\varepsilon^*-4\rho-\rho^*)(\Delta-4\gamma+\mu)-(\delta+\pi^*-\alpha^*-3\beta-4\tau)(\delta^*-\pi-4\alpha)-3\psi_2]\psi_0^B = 4\pi T_0, \tag{3.12}$$

where all the indexes A are omitted and

$$T_0 = (\delta+\pi^*-\alpha^*-3\beta-4\tau)(D-2\varepsilon-2\rho^*)T^B_{lm} - (\delta+\pi^*-2\alpha^*-2\beta)T^B_{ll} + \\ +(D-3\varepsilon+\varepsilon^*-4\rho-\rho^*)[(\delta+2\pi^*-2\beta)T^B_{lm} - (D-2\varepsilon+2\varepsilon^*-\rho^*)T^B_{mm}.$$

This equation is separable for ψ_0^B. The complete set of NP equations is invariant under the change $l \leftrightarrow n$ and $m \leftrightarrow m*$, valid for the choice of $n, l, m, m*$ used here. Then one can derive the equations for ψ_4^B, using this transformation on the last two equations. One has:

$$[(\Delta+3\gamma-\gamma^*+4\mu+\mu^*)(D+4\varepsilon-\rho)-(\delta^*-\tau^*+\beta^*+3\alpha+4\pi)(\delta-\tau+4\beta)-3\psi_2]\psi_4^B = 4\pi T_4,$$

where

$$T_4 = \Delta+3\gamma-\gamma^*+4\mu+\mu^*)[(\delta^*-2\tau*+2\alpha)T_{nm^*} - (\Delta+2\gamma-2\gamma^*+\mu^*)T_{m^*m^*}] + \\ +(\delta^*-\tau^*+\beta^*+3\alpha+4\pi)[(\Delta+2\gamma+2\mu^*)T_{nm^*} - (\delta*-\tau*+2\beta+2\alpha)T_{nn}].$$

Above is the decoupled equation for gravitational perturbations. Now we will focus on the EM equations. They are particularly important considering the lack of detection of gravitational waves and the rich EM data from different astrophysical objects. The use of the linearized equations in those cases is discussed in the next chapter. Here, we will outline the derivation of those equations. Because the amplitude of the EM stress-energy tensor is of second order in the EM field, a change in the background metric by EM perturbation is also of second order and it can be ignored in the linearized Maxwell equations. Then one obtains a test-field approximation of the interactions close to a rotating non-charged black hole.

In details, the NP equations in this case are (where Eqs. (3.5) still hold):

$$(D-2\rho)\phi_1 - (\delta^*+\pi-2\alpha)\phi_0 = 2\pi J_l \tag{3.13}$$
$$(\delta-2\tau)\phi_1 - (\Delta+\mu-2\gamma)\phi_0 = 2\pi J_m \tag{3.14}$$
$$(D-\rho+2\varepsilon)\phi_2 - (\delta^*+2\pi)\phi_1 = 2\pi J_{m^*} \tag{3.15}$$
$$(\delta-\tau+2\beta)\phi_2 - (\Delta+2\mu)\phi_1 = 2\pi J_n \tag{3.16}$$

where J_μ is the 4-current density projected on the tetrads and the ϕ's is a first order test fields.

To reach the decoupled equations, one multiplies Eq. (3.13) with $(\delta-\beta-\alpha^*-2\tau+\pi^*)$ and Eq. (3.14) with $(D-\varepsilon+\varepsilon^*-2\rho-\rho^*)$ and subtract them. Then from the identity (3.11), for $p = 0, q = -2$ one can eliminate ϕ_1:

Next step in the derivations is to choose appropriate values for the parameters so that one can separate the equation for ϕ_0:

$$[(D-\varepsilon+\varepsilon^*-2\rho-\rho^*)(\Delta+\mu-2\gamma)-(\delta-\beta-\alpha^*-2\tau+\pi^*)(\delta^*+\pi-2\alpha)]\phi_0 = 2\pi J_0,$$
$$[(\Delta+\gamma-\gamma^*+2\mu+\mu^*)(D+2\varepsilon-\rho)-(\delta^*-\tau^*+\beta^*+\alpha+2\pi)(\delta-\tau+2\beta)]\phi_2 = 2\pi J_2, \tag{3.17}$$

where

$$J_0 = (\delta-\beta-\alpha^*-2\tau+\pi^*)J_l-(D-\varepsilon+\varepsilon^*-2\rho-\rho^*)J_m \tag{3.18}$$
$$J_2 = (\Delta+\gamma-\gamma*+2\mu+\mu*)J_{m*}-(\delta*+\alpha+\beta*+2\pi-\tau*)J_n. \tag{3.19}$$

Again, the equation for ϕ_2 is obtained by interchanging l and n and m and $m*$ in the equation for ϕ_0 in Eq. (3.17).

The next step is to write those equations in special a coordinate system. One uses the Boyer-Lindquist coordinates for $c = G = 1$ for which the Kerr metric is in the form written above Eq. (3.1).

Every NP tetrad must satisfy the orthogonality conditions: $l\cdot n = 1, m\cdot m^* = -1$, with all other scalar products equal to zero. The orthogonal relations do not change under the action of the 6-parameter group of the Lorenz transformations in every point of the space-time. Then the metric is:

$$g^{\mu\nu} = l^\mu n^\nu + n^\mu l^\nu m^\mu m^{*\nu} - m^{*\mu} m^\nu, \tag{3.20}$$

and

$$\eta_{\alpha\beta} = \begin{pmatrix} 0 & 1 & 0 & 0 \\ 1 & 0 & 0 & 0 \\ 0 & 0 & 0 & -1 \\ 0 & 0 & -1 & 0 \end{pmatrix} \tag{3.21}$$

We choose the direction of l and n so that the equation Eq. (3.5) and this uses 4 degrees of freedom. Then following [122], cited in [42], one can use the other 2 degrees of freedom so one ensures that $\varepsilon = 0$. The components of the so obtained tetrad (for t, r, θ, ϕ) are:

$$l^\mu = [(r^2+a^2)/\Delta, 1, 0, a/\Delta],$$
$$n^\nu = [r^2+a^2, -\Delta, 0, a]/(2\Sigma),$$
$$m^\mu = [ia\,\sin(\theta), 0, 1, \frac{i}{\sin(\theta)}]/[\sqrt{2}(r+ia\cos(\theta)].$$

The non-zero spin-coefficients are:

$$\rho = -1/(r-ia\cos(\theta), \quad \beta = -\rho^*\cot(\theta)/2\sqrt{2}, \quad \pi = ia\rho^2\sin(\theta)/2\sqrt{2},$$
$$\tau = -ia\rho\rho^*\sin(\theta)/\sqrt{2}, \quad \mu = \rho^2\rho^*\Delta/2, \quad \nu = \mu+\rho\rho^*(r-M)/2,$$
$$\alpha = \pi-\beta^*, \quad \psi_2 = -M\rho^3.$$

More details on the quantities in those equations can be found in [42].

Using the Kerr metric and the fact that $D = l^\mu d/dx^\mu, \Delta = n^\mu d/dx^\mu$ and $\delta = m^\mu/dx^\mu$, the equations can be written as one Master equation, valid for scalar test-fields (s=0), EM test-fields (s=1), neutrino test-fields ($s = \pm\frac{1}{2}$) and gravitational test-fields ($s = \pm 2$):

$$[\frac{\left(r^2-a^2\right)^2}{\Delta} - a^2\left(\sin\left(\theta\right)\right)^2]\frac{d^2}{dt^2}\psi + 4\,\frac{Mar\frac{d^2}{dtd\phi}\psi}{\Delta} + [\frac{a^2}{\Delta} - \left(\sin\left(\theta\right)\right)^{-2}]\frac{d^2}{d\phi^2}\psi -$$
$$-\Delta^{-s}\frac{\partial}{\partial r}\left(\Delta^{\varepsilon+1}\frac{d}{dr}\psi\right) - \frac{\frac{\partial}{\partial\theta}\left(\sin\left(\theta\right)\frac{d}{d\theta}\psi\right)}{\sin\left(\theta\right)} - 2\,s[\frac{a\left(r-M\right)}{\Delta} + \frac{i\cos\left(\theta\right)}{\left(\sin\left(\theta\right)\right)^2}]\frac{d}{d\phi}\psi -$$
$$-2\,s[\frac{M\left(r^2-a^2\right)}{\Delta} - r - ia\cos(\theta)]\frac{d}{dt}\psi + \left(s^2\left(\cot\left(\theta\right)\right)^2 - s\right)\psi = 4\,\pi\,\Sigma\,T.$$

s is the spin-weight, which can be positive or negative (or zero). For positive spin-weights, the quantity in the TME can be χ_0, ϕ_0, or ψ_0 (for $s = 1/2, 1, 2$ respectively). For negative spin-weights, the quantities in TME are χ_1, ϕ_2, ψ_4 each with a factor ρ^{2s} ($s = -1/2, -1, -2$). The source terms T also get modified with the same factor and the same index. This difference in Ψ appear in order to separate the variables. They are connected with the zero rotation used to obtain $\varepsilon = 0$. For other choices of rotation, the factors will change, but the main equation will remain the same. This equation is separable under the substitution

$$\Psi = e^{i(\omega t + m\phi)}S(\theta)R(r)$$

(see below) and one can find $S(\theta)$ and $R(r)$ – the angular and the radial parts of the solutions.

The physical information that one can obtain can be seen from:

$$4\,\pi\,T_{\mu\,\nu}{}^{scalar} = \Phi_{;\mu}\Phi_{;\nu} - 1/2\,g_{\mu\,\nu}\Phi_{;\alpha}\Phi^{;\alpha}$$
$$4\,\pi\,T_{\mu\,\nu}{}^{EM} = \Big\{\varphi_0\varphi_0^* n_\mu n_\nu + 2\,\varphi_1\varphi_1^*[l_{(\mu}n_{\nu)} + m_{(\mu}m_{\nu)}] + \varphi_2\varphi_2^* l_\mu l_\nu -$$
$$4\,\varphi_0^*\varphi_1 n_{(\mu}m_{\nu)} - 4\,\varphi_1^*\varphi_2 l_{(\mu}m_{\nu)} + \varphi_2\varphi_0^* m_\mu m_\nu\Big\} + c.c.,$$

where one can solve the TME with respect to Φ_2 and to find Φ_1 and Φ_0 from the equations (3.13–3.16), which are integrable Pfaffian equations for r and θ.

When there is a source term, one can use the eigenfunctions $S(\theta)$ to expand:

$$4\pi\Sigma T = \int d\omega \sum_{l,m} G(r)_s S_l^m(\theta) e^{im\phi} e^{i\omega t}, \tag{3.22}$$

$$\psi = \int d\omega \sum_{l,m} R(r)_s S_l^m(\theta) e^{im\phi} e^{i\omega t}, \tag{3.23}$$

where $R(r)$ will satisfy the radial equation (3.33) with $G(r)$ as a source term on the right-hand side.

If one solves the Teukolsky radial and angular equations, then in principle, it is possible to evaluate the energy emitted from the KBH during those EM perturbations:

$$\frac{d^2}{dtd\Omega}E^{EM} = \lim_{r\to\infty} r^2 T_t^r = \lim_{r\to\infty}\frac{r^2\left(|\phi_2|\right)^2}{2\pi} \tag{3.24}$$

For going to infinity waves, the components of the electromagnetic field satisfy: $E_{\hat{\theta}} = B_{\hat{\phi}}, E_{\hat{\phi}} = -B_{\hat{\theta}}$, therefore from (3.4), one obtains $\phi_2 \sim E_{\hat{\theta}} - iE_{\hat{\phi}}$. Thus energy will be proportional to the squares of the real and imaginary parts of ϕ_2 with two polarizations in direction of $e_{\hat{\theta}}$ and $e_{\hat{\phi}}$ [42].

For gravitational waves, the equations are much more complicated, but in two cases, the energy can be estimated – on infinity and on the horizon.

On infinity, the energy flux for outgoing waves with frequency ω is given by ([42]):

$$\frac{\partial^2}{\partial t \partial \omega} E^{out} = \lim_{r\to\infty} \frac{r^2\omega^2[\left(h_{\theta\theta}{}^B\right)^2 + \left(h_{\theta\,\phi}{}^B\right)^2]}{16\,\pi} = \lim_{r\to\infty} \frac{r^2\left(\left|\psi_4{}^B\right|\right)^2}{16\,\pi\,\omega^2} \tag{3.25}$$

For incoming waves, the formula reads:

$$\frac{d^2}{dtd\omega} E^{in} = \lim_{r\to\infty} \frac{r^2\left(\left|\psi_0{}^B\right|\right)^2}{64\,\pi\,\omega^2} \tag{3.26}$$

Before continuing with the solutions of the TRE and the TAE, it is important to discuss the problems in front of the linearized theory. It is well known that the strict meaning of the solutions, obtained by separation of the variables in TME has not been rigorously justified mathematically ([67]). The frequencies ω_n which are solutions of TME are infinite set, but they do not form a *complete* set of solutions (for more rigorous definition of the completeness, see [123]). This means that knowing the frequencies is not enough to describe the complete behavior of the system (One example of model of relativistic star with complete set of quasi-normal modes has been given by Price and Husain in [124].). Additionally, those modes grow on spacial infinity and they don't lead to square integrable solutions. Despite these mathematical "defects" of the QNMs, however, they have been proved to be useful in physics. More precisely, they have been observed in the spectra obtained by the full 3d general relativity simulations as discussed in the next chapter. Thus, although there are still problems in front of the theory, the spectra obtained from the linearized equations can give interesting physical information and is worth to be researched.

3.1.3 Teukolsky Radial equation and Teukolsky Angular equation

The TME in Boyer-Lindquist coordinates is separable under the substitution:

$$\Psi = e^{i(\omega t + m\phi)} S(\theta) R(r)$$

where $m = 0, \pm 1, \pm 2 \ldots$ for integer spins and $\omega = \omega_R + i\omega_I$ is a complex frequency (note that in this work we are using the Chandrasekhar notations in which the sign of ω is opposite to the one Teukolsky used). This frequency and the parameter E are the two complex constants of the separation. The stability condition requires $\omega_I > 0$ ensuring that the initial perturbation will damp with time. Making the separation, we obtain the Teukolsky angular (TAE) and the Teukolsky radial (TRE) equations,

which govern the angular and the radial evolutions of the perturbation accordingly. Key property of those equations is the fact that they both can be solved in terms of the confluent Heun function as first written by [35].

Explicitly, the TAE and the TRE are:

$$\left[\left(1-u^2\right) S_{lm,u}\right]_{,u} + \left[(a\omega u)^2+2a\omega s u+{}_sE_{lm}-s^2-\frac{(m+su)^2}{1-u^2}\right] S_{lm} = 0, \quad (3.27)$$

and

$$\frac{d^2R_{\omega,E,m}}{dr^2}+(1+s)\left(\frac{1}{r-r_+}+\frac{1}{r-r_-}\right)\frac{dR_{\omega,E,m}}{dr}+ \\ +\left(\frac{K^2}{(r-r_+)(r-r_-)}-is\left(\frac{1}{r-r_+}+\frac{1}{r-r_-}\right)K-\lambda-4\,is\omega r\right)\frac{R_{\omega,E,m}}{(r-r_+)(r-r_-)}=0 \quad (3.28)$$

where $\Delta = r^2 - Mr + a^2 = (r-r_-)(r-r_+)$, $K = \omega(r^2+a^2) - ma$, $\lambda = E - s(s+1) - a^2\omega^2 - 2am\omega$ and $u = \cos(\theta)$.

In general, these equations are ordinary linear second-order differential equations with 3 singularities, two of which regular, while $r = \infty$ is irregular singularity obtained via confluence of two regular singular points. For the TRE, the regular singularities $r_\pm$ are different if $a \neq M$. In the bifurcation point, $a = M$, $r_+ = r_-$ and the TRE has another irregular singularity ($r = M$) instead of the two regular ones. Hence this is the double confluent case. Note that the ring singularity $r = 0$, $\theta = \pi/2$ is not a singularity of the TME and does not play any role in its solutions (easily seen from Eq. (3.27) and Eq. (3.28)).

The two horizon $r_\pm$ are usually considered as coordinate singularities which can be avoided under certain choice of coordinates. This comes from the fact that the horizons are not singular points for the scalar invariants of the Riemann curvature tensor, where only the ring singularity occurs. This perception, however, was questioned by the evaluation of some of the differential invariants of the Weyl tensor required to fix completely the geometry. In the study by Fiziev in [67]), it is demonstrated that both the Cauchy and the event horizon are found to be coordinate independent geometrical objects, being at the same time singular points of the TRE and having the same mathematical nature. This result indicates that for any choice of coordinates, the number and the type of the singular points in the TRE do not change in the considered physical domain.

When $a \neq M$, these equations can be reduced to the confluent Heun equation and they can be solved in terms of confluent Heun functions (for the electromagnetic case $s = -1$, [35], [66], [67], [125, 126], [127]):

$$R_1(r) = C_1 e^{\frac{\alpha z}{2}}\left(r-r_+\right)^{\beta/2+1/2}\left(r-r_-\right)^{\gamma/2+1/2}\mathrm{HeunC}\left(\alpha,\beta,\gamma,\delta,\eta,-\frac{r-r_+}{r_+-r_-}\right)$$

and

$$R_2(r) = C_2 e^{\frac{\alpha z}{2}}\left(r-r_+\right)^{-\beta/2+1/2}\left(r-r_-\right)^{\gamma/2+1/2}\mathrm{HeunC}\left(\alpha,-\beta,\gamma,\delta,\eta,-\frac{r-r_+}{r_+-r_-}\right)$$

for the case, $r > r_+$, where:
$\alpha = -2\,i\left(r_+ - r_-\right)\omega$, $\beta = -\frac{2\,i(\omega\,(a^2+{r_+}^2)+am)}{r_+-r_-} - 1$,
$\gamma = \frac{2\,i(\omega\,(a^2+{r_-}^2)+am)}{r_+-r_-} - 1$, $\delta = -2i\big(r_+ - r_-\big)\omega\big(1 - i\left(r_- + r_+\right)\omega\big)$,
$\eta = \frac{1}{2}\frac{1}{\left(r_+-r_-\right)^2}\Big[4\omega^2{r_+}^4 + 4\left(i\omega - 2\omega^2 r_-\right){r_+}^3 + \big(1 - 4a\omega\,m - 2\omega^2a^2 - 2E\big)\times$
$\big({r_+}^2+{r_-}^2\big) + 4\left(i\omega\,r_- - 2i\omega\,r_+ + E - \omega^2a^2 - \frac{1}{2}\right)r_-\,r_+ - 4a^2\,(m+\omega\,a)^2\Big]$

For the angular function $S(\theta)$, we obtain for the solutions:

$$S_{\pm,s,m}(\theta) = \mathrm{e}^{\alpha\,z_\pm(\theta)}\,(z_\pm(\theta))^{\beta/2}\,(z_\mp(\theta))^{\gamma/2}\,\mathrm{HeunC}\,(\alpha,\beta,\gamma,\delta,\eta,z_\pm(\theta))$$

where

$$\alpha = \pm 4\,a\omega, \beta = s \mp m, \gamma = s \pm m, \delta = \mp 4\,a\omega s, \eta = \frac{m^2 - s^2}{2} \pm 2\,a\omega s - (a\omega)^2 - E + s^2,$$
$$z_+(\theta) = \cos^2\left(\frac{\theta}{2}\right), z_-(\theta) = \sin^2\left(\frac{\theta}{2}\right) = 1 - z_+(\theta).$$

Note, the confluent Heun function depends on 5 parameters (here α, β, γ, δ and η), but those parameters differ for the TAE and the TRE!

In general, these are two linearly independent solutions of the TAE. They arise from the properties of the Heun functions. A special attention is required in the case $s \in Z$ – when $|s-m| \in Z$ and the second linearly independent solution includes an integral of the confluent Heun function.

To fix the physical problem we want to study, we impose appropriate boundary conditions on the TRE and the TAE. These boundary conditions yield the spectrum – E and ω.

The spectrum of discrete frequencies ω that one obtains after imposing the boundary conditions are the quasi-normal modes of the black hole – its late-time ringing.

3.2 Non-rotating black holes

Although the focus of this work is on rotating black holes, the non-rotating case offers a useful way to check the applicability of the method in terms of a simpler problem, which was already studied extensively with other methods.

The linearized perturbations of the Schwarzschild metric are described by the Regge-Wheeler equation (RWE) and the Zerilli equation (ZE) or by the Teukolsky radial equation (TRE) in the limit $a \to 0$. In this work, we will consider only the spectrum obtained from the RWE and the TRE.

The angular equation for both cases is the solution of the Teukolsky angular equation when there is no rotation ($a = 0$):

$$S(\theta) = (\cos(\theta)-1)(\cos(\theta)+1)\mathrm{LegendreP}(l, 2, \cos(\theta)) = 0 \tag{3.29}$$

where $\theta \in [0, \pi]$ is the angle.

With the standard substitution, $\Phi = R(r)_{\omega,s,l}e^{i\omega t}$, for $M = 1/2$, the RWE can be written as [62]:

$$\frac{d^2}{dr^2}R(r)_{\omega,s,l} + (\omega^2 - V_{s,l})R(r)_{\omega,s,l} = 0, \tag{3.30}$$

where one has the potential: $V_{s,l} = \left(1 - \frac{1}{r}\right)\left(\frac{l(l+1)}{r^2} + \frac{1-s^2}{r^3}\right)$. The RWE has 3 singularities, two regular: the origin $r = 0$ and the BH horizon $r = 1$, and one irregular: infinity $r = \infty$.

The solutions of this equation in terms of confluent Heun functions for the case of gravitational perturbations ($s = -2$ and also $M = 1/2$) are [67]):

$$\begin{aligned} R(r) =& C_1 r^{\gamma/2+1}(r-1)^{\beta/2}e^{\frac{\alpha z}{2}}\,\mathrm{HeunC}(\alpha,\beta,\gamma,\delta,\eta,z) + \\ & C_2 r^{\gamma/2+1}(r-1)^{-\beta/2}e^{\frac{\alpha z}{2}}\,\mathrm{HeunC}(\alpha,-\beta,\gamma,\delta,\eta,z) \end{aligned} \tag{3.31}$$

where the values of the parameters $\alpha, \beta, \gamma, \delta, \eta$ are ([67, 66]):

$$\begin{aligned} &\alpha = -2\,i\omega, \beta = 2\,i\omega, \gamma = 4, \\ &\delta = -2\,\omega^2, \eta = 4 - l - l^2 + 2\,\omega^2, \\ &z = 1 - r \end{aligned}$$

Using the same standard substitution, $\Phi = R(r)e^{i\omega t}$, for $M = 1/2$, we find that for the gravitational perturbations $s = -2$, when there is no rotation, the TRE becomes:

$$\begin{aligned} (r-r_+)\,(r-r_-)\,\frac{d^2}{dr^2}R\,(r) + (1-2\,r)\frac{d}{dr}R\,(r) + \\ + \left(\frac{\omega^2 r^4 - 2i\omega\,r^2\,(2\,r - r_- - r_+)}{(r-r_+)\,(r-r_-)} + 8\,i\omega\,r - A\right)R\,(r) = 0 \end{aligned}$$

Its solutions in terms of confluent Heun functions are:

$$R(r) = C_1 r^{\gamma}(r-1)^{\beta/2+1}e^{\frac{\alpha z}{2}}\,\mathrm{HeunC}(\alpha,\beta,\gamma,\delta,\eta,z) + \tag{3.32}$$

$$C_2 r^{\gamma}(r-1)^{-\beta/2+1}e^{\frac{\alpha z}{2}}\,\mathrm{HeunC}(\alpha,-\beta,\gamma,\delta,\eta,z) \tag{3.33}$$

where the values of the parameters are:

$$\begin{aligned} &\alpha = -2\,i\omega, \beta = -2 - 2\,i\omega, \gamma = 2, \\ &\delta = -4i\omega - 2\,\omega^2, \eta = 2\,\omega^2 + 4i\omega - A, \\ &z = 1 - r \end{aligned}$$

and $A = E - s(s+1) = l(l+1) - s(s+1)$ is the separation constant. Those parameters were obtained by solving the Teukolsky radial equation and substituting $a = 0$ and they are clearly different from those in the Regge-Wheeler case. Whether the two spectral equations (the equations obtained after imposing the appropriate boundary conditions) give the same spectrum, will be checked in the next chapter.

Chapter 4

Numerical Results

4.1 Quasi-normal modes of nonrotating black holes

The study of quasi-normal modes (QNMs) of a black hole (BH) has long history [53, 43, 63, 37, 69, 60, 65]. The reason behind this interest is that the QNMs offer a direct way of studying the key features of the physics of compact massive objects, without the complications of the full 3D general relativistic simulations. For example, by comparing the theoretically obtained gravitational QNMs with the frequencies of the gravitational waves, one can confirm or refute the nature of the central engines of many astrophysical objects, since those modes differ for the different types of objects – black holes, superspinars (naked singularities), neutron stars, black hole mimickers etc. [94, 95, 40, 41, 96, 97].

To find the QNMs, one needs to solve the second-order linear differential equations describing the linearized perturbations of the metric: the Regge-Wheeler equation (RWE) and the Zerilli equation (ZE) for the Schwarzschild metric or the Teukolsky radial equation (TRE) for the Kerr metric and to impose the appropriate boundary conditions – the so-called black-hole boundary conditions (waves going simultaneously into the horizon and into infinity)[53, 43]. Additionally, one requires regularity condition for the angular part of the solutions. And then, one needs to solve a connected problem with two complex spectral parameters – the frequency ω and the separation constant E ($E = l(l+1)$ – real for a nonrotating BH with l the angular momentum of the perturbation) . This system was first solved by Chandrasekhar & Detweiler[53] and Teukolsky & Press [51] and later developed through the method of continued fractions by Leaver [45]. For more recent results, see also [65, 60, 63, 69].

Because of the complexity of the differential equations, until now, those equations were solved either approximately or numerically meeting an essential difficulties [53]. The indirect approaches like continued fractions method have some limitations and are not directly related with the physics of the problem. The RWE, the ZE and the TRE, however, can be solved analytically in terms of confluent Heun functions as done for the first time in [62, 67, 104, 66]. Imposing the boundary conditions on those solutions *directly* (see [62, 97]) one obtains a system of spectral equations ((3.29) and (4.1)) featuring the confluent Heun functions which can be solved numerically.

In this section, we present a new method for finding l and ω *directly* in the case for gravitational perturbation $s = -2$ in a Schwarzschild metric, i.e. we solve the RWE and the TRE analytically in terms of confluent Heun functions and we use the two-dimensional generalization of the Müller method described in the Appendix:

"Numerical Methods" to solve the system of two transcendental equations with two complex variables. Then we use the epsilon-method to study the dependence of the solutions and the spectrum with respect to small variations in the phase condition. Additionally, with this method we demonstrate that the so-called algebraically special mode $n = 8$ has a nonzero real part with precision of more than 6 digits. This firmly refutes the hypothetical relation of this mode with the algebraically special one.

4.1.1 General form of the equations

To find the QNMs one needs to solve a system of two transcendental spectral equations. One of them is the TAE for $a = 0$, Eq. (3.29). The results for the QNMs should be independent of the choice of θ in the spectral conditions. In our numerical experiments, we use $\theta = \pi - 10^{-7}$.

The general form of the radial equations is obtained from the solutions of the RWE and the TRE written in terms of the confluent Heun functions (Eq. (3.31) and Eq. (3.33)), on which the black hole boundary conditions have been imposed [67]. Those boundary conditions coincide with the conditions for the rotating black hole with $a = 0$, so they will be considered in detail in the next section. Here, they simplify to the choice of local solution in terms of the Heun function (from the boundary condition on the horizon). For the two cases in question, the solution R_1 is valid for the RWE (Eq. (3.31)) and the solution R_2 is the valid one for the TRE (Eq. (3.33)).

Then, it remains to impose the following boundary condition on the space infinity (for details see [97, 67] and the next section):

$$R = r_\infty^p \text{HeunC}(\alpha, \beta, \gamma, \delta, \eta, 1 - r_\infty) = 0, \tag{4.1}$$

where HeunC is the confluent Heun functions as defined in MAPLE and the parameters $\alpha, \beta, \gamma, \delta, \eta$ and p are as follows:

1. For the solutions of the Regge-Wheeler Equation:

$$\alpha = -2\,i\omega, \beta = 2\,i\omega, \gamma = 4, \delta = -2\,\omega^2, \eta = 4 - l - l^2 + 2\,\omega^2,$$
$$r_\infty = 20\,\mathrm{e}^{-i(1/2\,(1+\varepsilon)\pi + arg(\omega))}, p = 3$$

2. For the solutions of the Teukolsky Radial Equation:

$$\alpha = -2\,i\omega, \beta = 2 + 2\,i\omega, \gamma = 2, \delta = -4i\omega - 2\,\omega^2, \eta = 2\,\omega^2 + 4i\omega - A,$$
$$r_\infty = 20\,\mathrm{e}^{-i(1/2\,(1+\varepsilon)\pi + arg(\omega))}, p = 5$$

where $A = l(l+1) - s(s+1)$ is the separation constant($s = -2$). Here the radial variable is chosen to be $|r_\infty| = 20$ which turns out to be large enough to simulate numerically the actual infinity ([67, 66]). Also, here the parameter β is chosen to reflect the local solution being used. ε is defined below.

4.1.2 The epsilon-method for nonrotating black holes

For values of the parameters α, β, γ, δ, η of general type, the confluent Heun function HeunC$(\alpha, \beta, \gamma, \delta, \eta, z)$ has branching points in the complex z-plane at the singular points $z = 1$ and $z = \infty$. In the MAPLE package, as a branch cut is chosen the semi-infinite interval $(1, \infty)$ on the real axis. The presence of the branch cut may lead to the disappearance of some modes or their translation, since by changing the phase of the complex variable r, we may make a transition to another sheet of the multivalued function.

In this section, we begin introducing the *epsilon*-method, with which one can control the sheet of the multivalued function. This is done using a small variation ($|\,\varepsilon\,| < 1$) in the phase condition $\arg(r) + \arg(\omega) = -\pi/2$ (defined by the direction of steepest descent, see [62] or the next section). Because of the gaps in the analytical theory of the confluent Heun functions, the only way to examine the effect of the branch cuts on the spectrum is numerically. An additional problem is the lack of documentation of the branch cuts in the numerical realization of the confluent Heun function in MAPLE. A more detailed study on some of the branch cuts can be found in the next section "Electromagnetic QNMs of rotating black holes".

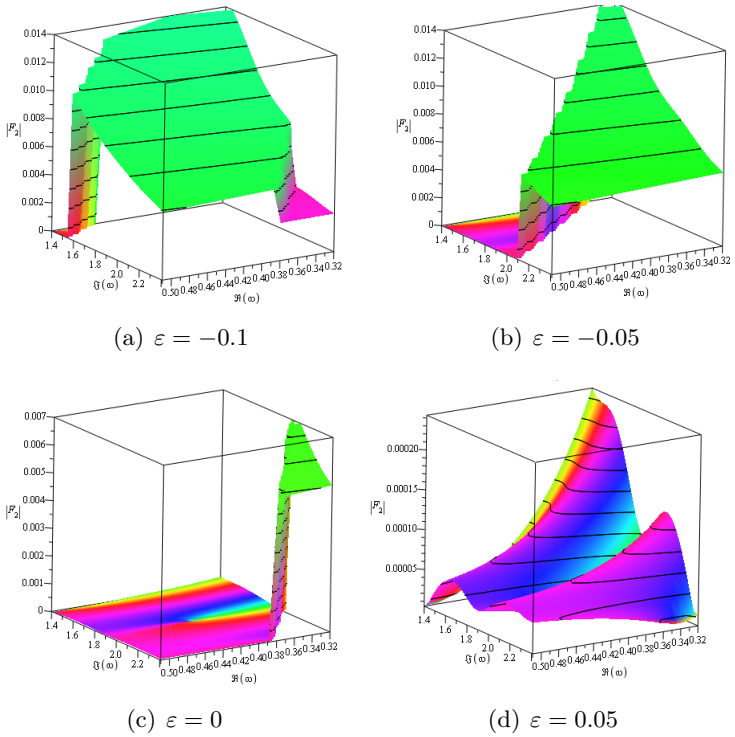

(a) $\varepsilon = -0.1$ (b) $\varepsilon = -0.05$

(c) $\varepsilon = 0$ (d) $\varepsilon = 0.05$

Figure 4.1: 3d plots of the function $F_2 = |R(\omega, \varepsilon)^{RWE}|$ in the complex interval $\omega = 0.32 + 1.4i..0.5 + 2.4i$ for $\varepsilon = 0.05, 0, -0.05, -0.1$ (the colors encode the phase of the complex function F_2.). The wall characteristic of the branching of the multivalued function is moved by ε either to the left ($\varepsilon < 0$) or to the right ($\varepsilon > 0$)

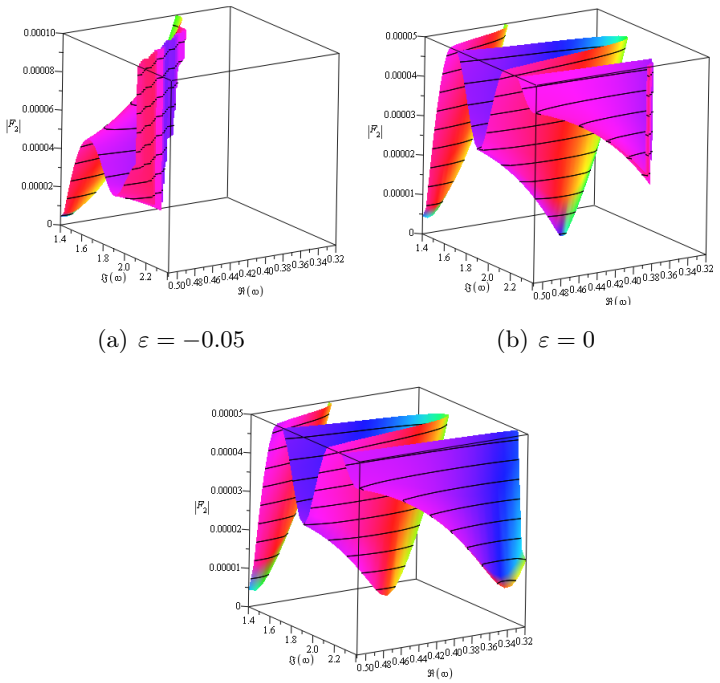

(a) $\varepsilon = -0.05$ (b) $\varepsilon = 0$

(c) $\varepsilon = 0.05$

Figure 4.2: 3d plots of the function $F_2 = |R(\omega, \varepsilon)^{RWE}|$ for $\varepsilon = -0.05$,$\varepsilon = 0$ and $\varepsilon = 0.05$ in the same interval for the complex ω as in 4.1 scaled near the expected roots. The different ε lead to different profiles of the roots

Here, we present an illustration of the way the branch cuts of the solutions of the radial equation move for different values of ε. Such an illustration cannot be easily obtained in the case of rotating black holes, where the radial function depends not on one complex parameter (ω), but on two (ω, E). On Fig. 4.1, Fig. 4.2 and Fig. 4.3, we have plotted the function $R(\omega, \varepsilon)$ in the case of solutions of the TRE and the RWE for different values of ε . From them, it is clear that the movement of the branch cuts affects the radial function and its *roots*, something which requires more serious study.

4.1.3 The numerical spectra

From the angular equation (3.29), it is clear that it can be solved explicitly without solving the system (3.29) and (3.33) and the values of l are known: $l = 2, 3, \ldots$. Here, only the first value, $l = 2$, is used to find the QNMs with both radial equations. One can then either solve only the radial equations or to solve the system [(3.29), (3.33)] with the appropriate values of the parameters. If one solves the problem as a two-dimensional system, for calculations with 15 digits of precision (and 32 software floating-point digits), one obtains as expected $l = 1.99(9) + 1 \times 10^{-17} i$. In the so obtained numerical value for l, the first different from 9 digit is the 17^{th}.

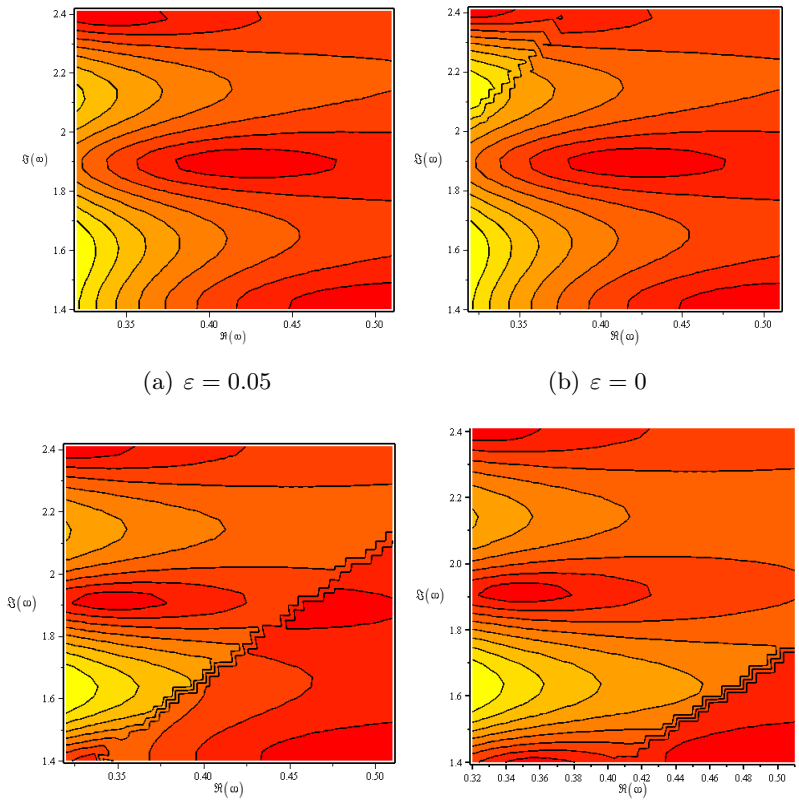

(a) $\varepsilon = 0.05$ (b) $\varepsilon = 0$

(c) $\varepsilon = -0.05$ (d) $\varepsilon = -0.08$

Figure 4.3: Plot of the level curves of the function $F_2 = |R(\omega, \varepsilon)^{TRE}|$ for $\varepsilon = 0.05, 0, -0.05, -0.08$ for $\omega = 0.32 + 1.4i..0.55 + 2.4i$. The movement of the branch cut due to the change of ε can be clearly seen.

The numerical results for the frequencies are summed in Table (4.1).

From the table, one can see that the frequencies from the two types of equations coincide with at least 6 digits. A comparison between the RWE frequencies and the ones published by Andersson ([58]), published in [128] shows that the difference between the two results is smaller than 5×10^{-8} in most cases and is due to the numerical reasons.

There are two important results from this study.

First, as seen from the table 4.1 for both the RWE and the TRE, the mode number 8 has small but nonzero real part. According to Leaver's evaluations this mode should be equal to $0 + 3.998000i$ [45], with an exactly zero real part and imaginary part $4i$, if it is to correspond to the so-called *algebraically special mode*.

Algebraically special (AS) modes have a special place in the QNM studies [53]. The Andersson method is not applicable for them and these are excluded from his consideration. Berti, Cardoso and Starinets ([65, 60]) make a review on the results so far concerning these modes. Theoretically the 9th mode ($n = 8$) should be purely imaginary with value $4i$, if it indeed corresponds to the AS case. In our results, even

n	ω from the Regge-Wheeler Eq.	ω from the Teukolsky Eq.
0	0.7473433688+0.1779246316i	0.7473433676+0.1779246260i
1	0.6934219937+0.5478297504i	0.6934219698+0.5478298839i
2	0.6021069092+0.9565539668i	0.6021069568+0.9565538786i
3	0.5030099245+1.4102964056i	0.5030097036+1.4102966442i
4	0.4150291600+1.8936897821i	0.4150291670+1.8936897747i
5	0.3385988052+2.3912161094i	0.3385987682+2.3912160831i
6	0.2665046794+2.8958212549i	0.2665047149+2.8958212406i
7	0.1856446653+3.4076823515i	0.1856446394+3.4076823843i
8	-0.0306490371+3.9968237195i	-0.0306490242+3.9968236554i
9	0.1265269702+4.6052896060i	0.1265270059+4.6052895329i
10	0.15310679658+5.1216534769i	0.1531069231+5.1216532271i

Table 4.1: A list of the frequencies obtained for the QNMs of Schwarzschild black hole using the Regge-Wheeler equation and the Teukolsky equation. The modes with $n < 5$ are found for $\varepsilon = 0$, modes from $n \geq 5$ – with $\varepsilon = -0.3$. The first 5 frequencies ($n = 0 - 4$) were obtained also by Fiziev in [62] using exact solutions of the RWE in the Heun functions

though purely imaginary modes do not pose a problem for the method, the real part of 9th mode is distinctly not zero and it has at least 7 stable digits when changing ε in the interval discussed below for both the RWE and the TRE. This clearly shows that this mode does not agree with the hypothesis for the AS mode, which is to be expected since the AS mode should correspond to different boundary conditions – those of the so-called totally-transmission modes ([129]).

The second important result is the dependence of the frequencies ω_n on ε. The direction of steepest descent is supposed to be the optimal direction in which the solutions satisfy the black hole boundary conditions on infinity in the first term approximation for asymptotic series for the Heun functions.([62]). The validity of steepest descent method in its simplest form for the radial equations (4.1) in both cases under variations in this condition, however, is still an open problem studied here for the first time.

Using the ε-method one can explore the intervals for ε in which each mode can be found. The results for both the RWE and the TRE as expected coincide. Generally, the intervals into which each mode can be found narrow down when increasing n. While for the first 5 modes it is possible to find $\omega_n = \pm|\Re(\omega_n)| + \Im(\omega_n)i$ for positive and negative values of ε in certain interval [1], for $n > 4$, (but $n \neq 8$) the modes with positive real part can be found only for negative values of ε and the dependence becomes $\omega_n(\varepsilon) = -\mathrm{sgn}(\varepsilon)|\Re(\omega_n)| + \Im(\omega_n)i$.

For $n = 8$, the mode has different behavior with respect to ε – for $\varepsilon \in [-0.75, -0.1]$, one finds a mode with *negative* real part and vice versa: $\omega_{n=8} = \mathrm{sgn}(\varepsilon)\, 0.030649006 + 3.996823690i$.

[1] The ranges where each mode is found depend on ε as follows: for $n = 0$: $\varepsilon \in [\mp 0.8, \pm 0.75]$, for $n = 1$: $\varepsilon \in [\mp 0.8, \pm 0.45]$, for $n = 2$: $\varepsilon \in [\mp 0.8, \pm 0.25]$, for $n = 3$: $\varepsilon \in [\mp 0.8, \pm 0.1]$, for $n = 4$: $\varepsilon \in [\mp 0.8, 0]$, where the first sign corresponds to frequencies with a positive real part and the second sign – to those with negative real parts. The imaginary parts for each mode n coincide.

The so found relation $\omega_n(\varepsilon)$ needs to be examined further. For the case $n = 8$, similar to some extent behavior was mentioned also in [129, 130] (and discussed in [60]), where it is suggested that there are two AS modes which are symmetrical to the imaginary axis and which are related with the branch cut in the asymptotic of the RWE potential when ω is purely imaginary. Using the ε-method applied on the asymptotics of the confluent Heun functions, one can directly obtain the place of the branch cut on the real axis as a function of ε and they can be easily visualized plotting the solution $R^{\pm}$. Therefore, the use of the confluent Heun functions and the ε-method offers a direct way to examine the solutions and their properties in relation to the branch cut in the complex r-plane, something that cannot be readily done in the continued fraction method generally used to obtain the QNMs.

Further exploration of the dependence $\Re(\omega_n)(\varepsilon)$ (or $\Im(\omega_n)(\varepsilon)$) in the intervals mentioned above shows that for both the RWE and the TRE, it bears some resemblance to a periodic function with amplitude A and period L which change with n in a nontrivial way (Fig.4.4 and Fig. 4.5). For $n < 4$, from the RWE and the TRE one obtains $A_{TRE} \approx 10^{-6} \approx 10^3 \times A_{RWE}$, $L_{RWE} \approx L_{TRE} \approx 0.4$ and those values remain approximately constant with respect to n ($n < 4$). For $n \geq 4$, the dependence of A and L on n becomes more pronounced: the amplitudes and the periods of the RWE increase with n until they reach $A_{RWE} \approx 10^{-6}$, $L_{WRE} \approx 0.6$ for $n = 10$. For the TRE the amplitude and the period decrease to $A_{TRE} \approx 10^{-8}$, $L_{TRE} \approx 0.05$. For $n = 8$, the two periodic behaviors have approximately equal amplitudes $\approx 10^{-7}$. Those results hint that although the so-obtained frequencies are stable with at least 6 digits with respect to ε, there is also some finer dependence the origin of which should be carefully investigated.

The visible change in the dependence of the QNMs on ε around $n = 4$ (see Fig. 4.4 and 4.5), is probably due to the fact that for the lower modes ($n \leq 4$), the branch cuts, $\Im(r) = 0$, are far from the roots we are trying to find and changing ε in any direction does not bring significantly closer the discontinuity. For the higher modes, where the branch cuts are much closer to the roots, the modes can be found only when ε pushes the discontinuity further from the mode, thus the symmetry with respect to ε is broken.

4.1.4 Summary of the results

- The gravitational QNMs for a Schwarzschild BH obtained from the RWE and the TRE were obtained, by solving the differential equations analytically in terms of confluent Heun functions. The QNMs from the TRE for the case $s = -2$ were calculated for the first time and were found to coincide with the well-known QNMs from the RWE with precision of 6 digits.

- Trough a new method for studying the dependence of the QNM spectra on the value of the complex radial variable, it was demonstrated that there is nontrivial dependence on small variation in the phase condition.

- For the first time, the mode $n = 8$ was obtained directly from the spectral

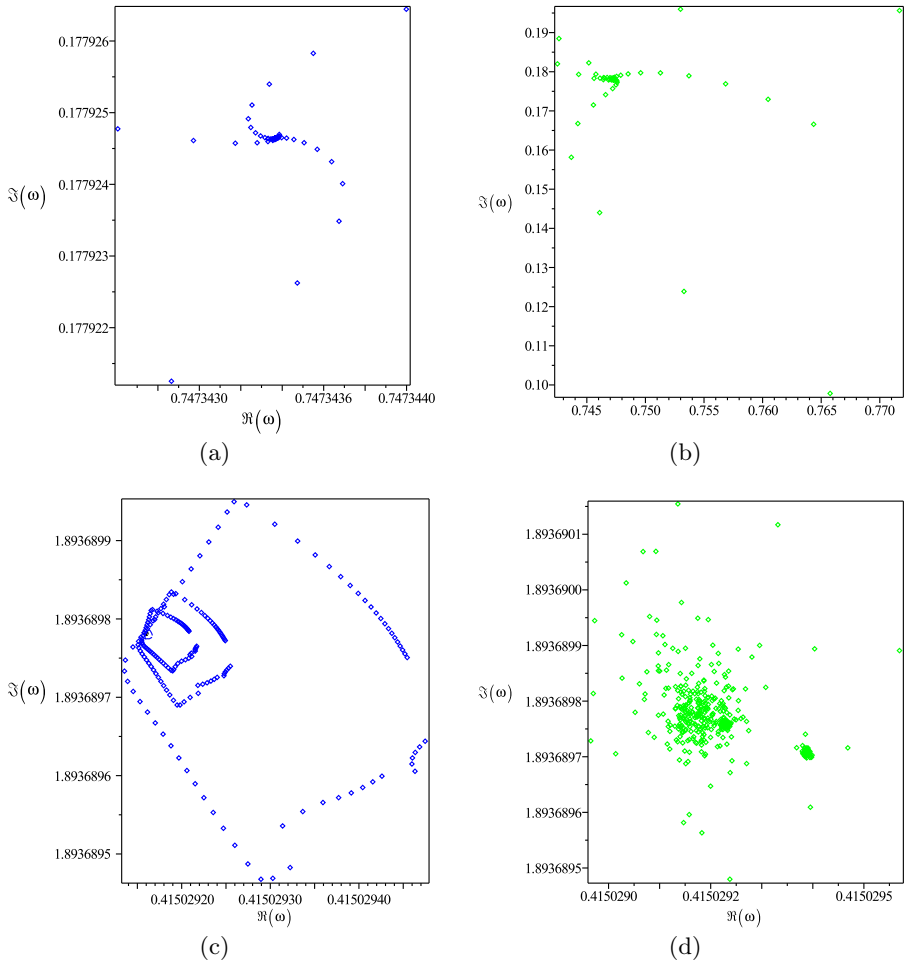

Figure 4.4: Complex plots of the *scaled* QNMs, ω, from the two equations in the appropriate intervals for ε a)ω_n^{RWE} for $n = 0..3$ b)ω_n^{TRE} for $n = 0..3$ c) ω_n^{RWE} for $n = 4..10$ d)ω_n^{TRE} for $n = 4..10$. Clearly while for $n = 0..3$ the QNMs from the two equations give similar results, for $n > 4$, the variations in the frequencies from TRE happen on a much smaller scale and appear chaotic

condition on the exact analytical solutions of the RWE and the TRE and was found to have a nonzero real part with at least 6 digits of precision (with respect to changes in ε). This proves that $n = 8$ is not an algebraically special mode.

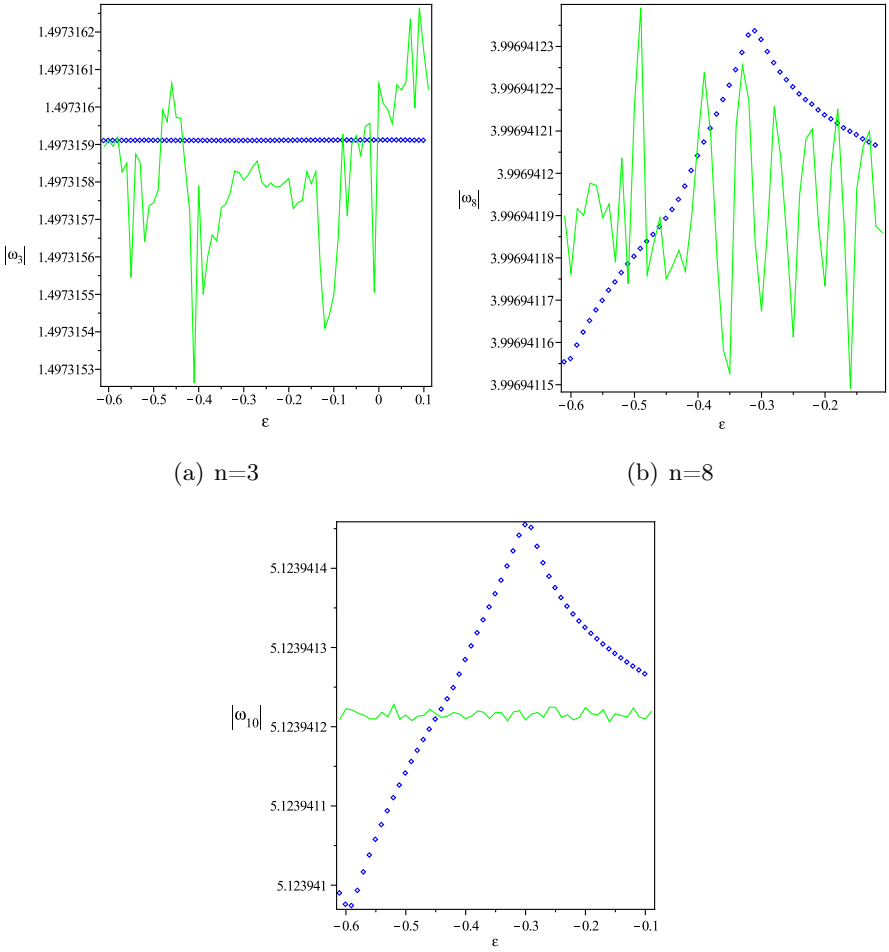

(a) n=3

(b) n=8

(c) n=10

Figure 4.5: Plots of $abs(\omega)(\varepsilon)$, where the solid line corresponds to the TRE modes and the dots – to the RWE modes for a) n=3, b) n=8, c) n=10. One can see the evolution of the so-called amplitudes and periods in both cases, when n increases from 3 to 10

4.2 Electromagnetic quasi-normal modes of the Kerr black hole

In this section we continue with the application of the new method for solving numerically two-dimensional systems featuring the Heun functions (the two-dimensional generalization of the Müller method described in [128]), this time in the considerably more complicated system describing the EM perturbations of rotating black holes. As we showed in the previous section, for the gravitational perturbation $s = -2$ of the Schwarzschild metric ([109]), this method gives interesting results, some of which repeat with high precision the results already published by other authors. Additionally, we were able to refute the 9^{th} mode as an algebraically special and showed its properties are related to the branch cuts in the solution of the radial equation. While the analysis of the potentials of the Regge-Wheeler equation (RWE) and the Zerilli equation (ZE) hinted of the importance of the branch cut on the imaginary axis for understanding this mode [129, 130], this result is directly obtainable from the actual solutions of the RWE and ZE in terms of the confluent Heun functions.

With respect to the branch cuts, our study is particularly important, since it cannot be done with the most often used continued fraction method, where the radial variable does not explicitly enter the equations being solved and which cannot be used for purely imaginary frequencies ([57], p.8). If one looks at the equations used by this method in detail, it turns out that the angular equation [45] in the continued fraction method coincides with the the three-term recurrence defining the confluent Heun function, solution of the TAE, in the neighborhood of the two regular singular points, $u = -1, 1$, where $u = \cos(\theta)$ ([107] Eq. (1.9-1.10). The radial equation in the continued fraction method, however, differs from the solution of the TRE in terms of the confluent Heun functions. This is because in Leaver's paper, the series from which the continued fraction are obtained are developed for the powers of $\frac{r-r_+}{r-r_-}$ (due to switching the places of the singular points, see [57], p.7), while the asymptotic three-term recurrence of the confluent Heun function at infinity is developed for $\frac{1}{r-r_-}$. Note that in MAPLE, for $r > r_+$, the evaluation of the confluent Heun functions at infinity is obtained by numerical integration from the second singularity $r = r_+$.

In this section, we continue the exploration of the application of the confluent Heun functions by studying the QNMs of the Kerr BH. Our results show that using the confluent Heun function, one can obtain the QNMs for a wide range of modes and rotational parameters, and that there is very good agreement between some of our results and those obtained within other methods. The use of the ε-method made it possible, for the first time to study the dependence of the so obtained frequencies on small deviations in the phase condition and it is shown how this nontrivial dependence evolves with n and a. In this case, some of the modes are independent of ε which should be expected since the frequencies should not depend on the radial variable. Other modes, however, depend critically on the value of ε and they can differ seriously from the already published results. Additionally, details

how the modes change in the interval of validity of the steepest descent method are presented.

4.2.1 The Teukolsky angular equations

In Chandrasekhar's notation, the Teukolsky Master Equation ([51]), for $|s| = 1$ is separable under the substitution $\Psi = e^{i(\omega t + m\phi)} S(\theta) R(r)$, where $m = 0, \pm 1, \pm 2$ for integer spins and ω is the complex frequency. Because of the choice of this form of Ψ, the sign of ω differs from the one Teukolsky used, and the stability condition, guaranteeing that the perturbations will damp with time, reads $\Im(\omega) > 0$.

The TAE for EM perturbations ($s = -1$) has 16 classes of exact solutions $S(\theta)$ in terms of the confluent Heun functions (for full details see [67]). To fix the spectrum approximately, one requires an additional regularity condition for the angular part of the perturbation, which means that if we choose one solution, $S_1(\theta)$ regular around the one pole of the sphere ($\theta = 0$) and another, $S_2(\theta)$, which is regular around the other pole ($\theta = \pi$), then in order to ensure a simultaneous regularity, the Wronskian of the two solutions should become equal to zero, $W[S_1(\theta), S_2(\theta)] = 0$. This gives us one of the equations for the two-dimensional system that needs to be solved to obtain the QNMs of the Kerr BH.

In [67], there are four pairs of Wronskians, each pair being valid in a sector of the plane $\{s, m\}$. Ideally, using any of them should lead to the same spectrum. Numerically, the results obtained with the different Wronskians coincide within 11-13 digits of precision. The Wronskians used to obtain the spectrum are:

$$W[S_1, S_2] = \frac{\text{HeunC}'(\alpha_1, \beta_1, \gamma_1, \delta_1, \eta_1, (\cos(\pi/6))^2)}{\text{HeunC}(\alpha_1, \beta_1, \gamma_1, \delta_1, \eta_1, (\cos(\pi/6))^2)} + \frac{\text{HeunC}'(\alpha_2, \beta_2, \gamma_2, \delta_2, \eta_2, (\sin(\pi/6))^2)}{\text{HeunC}(\alpha_2, \beta_2, \gamma_2, \delta_2, \eta_2, (\sin(\pi/6))^2)} + p = 0 \tag{4.2}$$

where the derivatives are with respect to z and the values of the parameters for the two confluent Heun functions for each m are as follows:

For the case $m = 0$: $\alpha_1 = 4\,a\omega, \beta_1 = 1$,

$\gamma_1 = -1, \delta_1 = 4\,a\omega, \eta_1 = 1/2 - E - 2\,a\omega - a^2\omega^2$ and

$\alpha_2 = -4\,a\omega, \beta_2 = 1, \gamma_2 = 1, \delta_2 = -4\,a\omega, \eta_2 =, 1/2 - E + 2\,a\omega - a^2\omega^2$, $p = \frac{1}{(\sin(\pi/6))^2}$

For the case $m = 1$: $\alpha_1 = -4\,a\omega, \beta_1 = 2, \gamma_1 = 0, \delta_1 = 4\,a\omega, \eta_1 = 1 - E - 2\,a\omega - a^2\omega^2$ and

$\alpha_2 = -4\,a\omega, \beta_2 = 0, \gamma_2 = 2, \delta_2 = -4\,a\omega, , \eta_2 = 1 - E + 2\,a\omega - a^2\omega^2$ and $p = -4\,a\omega$

For the case m=2: $\alpha_1 = -4\,a\omega, \beta_1 = 3, \gamma_1 = -1, \delta_1 = 4\,a\omega, \eta_1 = 5/2 - E - 2\,a\omega - a^2\omega^2$ and

$\alpha_2 = -4\,a\omega, \beta_2 = 1, \gamma_2 = -3, \delta_2 = -4\,a\omega, \eta_2 = 5/2 - E + 2\,a\omega - a^2\omega^2$ and $p = 8 - 4a\omega$.

where we use $\theta = \pi/3$ (the QNMs should be independent of the choice of θ in the spectral conditions).

These Wronskians differ from those in [67], most notably by the presence of the term p. The reason for this is that they were constructed using different two solutions $[S_1(\theta), S_2(\theta)]$ of the TAE (note that the sign convention in this paper differs from the one in [67]), each of which still being regular on one of the poles. That was done to improve the numerical convergence of the root-finding algorithm and to avoid MAPLE's problems with the evaluation of the confluent Heun function and its derivative for certain values of the parameters.

4.2.2 The Teukolsky radial equation

The TRE differential equation is of the confluent Heun type, with $r = r_\pm$ regular singular points and $r = \infty$ – irregular one. As it was noted in [97], the point $r = 0, \theta = \pi/2$ is not a singularity for this equation and, therefore, it need not be considered when imposing the boundary conditions. The solutions of the TRE for $r > r_+$, are :

$$\begin{aligned} R(r) &= C_1 R_1(r) + C_2 R_2(r), \text{for} \\ R_1(r) &= e^{\frac{\alpha z}{2}} (r-r_+)^{\frac{\beta+1}{2}} (r-r_-)^{\frac{\gamma+1}{2}} \text{HeunC}(\alpha, \beta, \gamma, \delta, \eta, z) \\ R_2(r) &= e^{\frac{\alpha z}{2}} (r-r_+)^{\frac{-\beta+1}{2}} (r-r_-)^{\frac{\gamma+1}{2}} \text{HeunC}(\alpha, -\beta, \gamma, \delta, \eta, z), \end{aligned} \tag{4.3}$$

where $z = -\frac{r-r_+}{r_+-r_-}$ and the parameters are:

$$\alpha = -2\,i\left(r_+ - r_-\right)\omega,\ \beta = -\frac{2\,i(\omega\,({r_+}^2+{r_-}^2)+am)}{r_+-r_-} - 1,$$

$$\gamma = \frac{2\,i(\omega\,({r_+}^2+{r_-}^2)+am)}{r_+-r_-} - 1,$$

$$\delta = -2i\left(r_+ - r_-\right)\omega\left(1 - i\left(r_- + r_+\right)\omega\right),$$

$$\eta = \tfrac{1}{2}\frac{1}{\left(r_+-r_-\right)^2} \times \Big[4\omega^2 {r_+}^4 + 4\left(i\omega - 2\omega^2 r_-\right){r_+}^3 + \left(1 - 4a\omega\, m - 2\omega^2 a^2 - 2E\right) \times$$

$$\left({r_+}^2 + {r_-}^2\right) + 4\left(i\omega\, r_- - 2i\omega\, r_+ + E - \omega^2 a^2 - \tfrac{1}{2}\right) r_-\, r_+ - 4a^2\,(m+\omega\, a)^2\Big].$$

Here we have followed MAPLE's internal rules when constructing the general solution of the differential equation from the confluent Heun type. Accounting for the symmetries of the confluent Heun function, the solutions (4.4) coincide with those in [67] (for ω replaced with $-\omega$). [2]

The TRE has 3 singular points r_-, r_+, ∞ and in order to fix the spectrum, one needs to impose specific boundary conditions on two of those singularities (i.e. to solve the central two-point connection problem [105]). Different boundary conditions on different pairs of singular points will specify different physics of the problem. In our case, we impose the black hole boundary conditions (BHBC) – waves going simultaneously into the event horizon (r_+) and into infinity – following the same reasoning as in [97] where additional details can be found. Then, the BHBC read:

1. BHBC on the KBH event horizon r_+.

[2] It is important to emphasize that the so obtained solutions cannot be used for extremal KBH ($a = M$) since in this case the differential equation is of the double confluent type and its treatment differs, so it is outside the scope of this work.

For $r \to r_+$, from $r(t) = r_+ + e^{\frac{-\Re(\omega)t+const}{\Im(n_{1,2})}} \to r_+$, where $n_{1,2}$ are the powers of the factors $(r-r_+)^{n_{1,2}}$ in $R_{1,2}$, follows that for $m=0$, the only valid solution in the whole interval $(-\infty,\infty)$ is R_2, while for $m \neq 0$, the solution R_2 is valid for frequencies for which $\Re(\omega) \notin (-\frac{ma}{2Mr_+}, 0)$. This means that the rotation splits the area of validity of R_2 into two and if this condition is not fulfilled, then the spectrum corresponds to waves going out of the horizon – a white hole. We won't pursue the spectrum in the case of a white hole, but it is important to keep in mind that the boundary conditions correspond to a BH, only in the ranges of validity of each solution. In our numerical work we use only R_2 since the confluent Heun function in R_1 is numerically unstable in MAPLE.

2. BHBC at infinity.

   At $r \to \infty$, the solution is a linear combination of an ingoing ($R_{\leftarrow}$) and an outgoing ($R_{\rightarrow}$) wave: $R = C_{\leftarrow} R_{\leftarrow} + C_{\rightarrow} R_{\rightarrow}$, where $C_{\leftarrow}$, $C_{\rightarrow}$ are unknown constants and $R_{\leftarrow}, R_{\rightarrow}$ are found using the asymptotics of the confluent Heun function as defined in [105, 67].

   To ensure only outgoing waves at infinity, one needs to have $C_{\leftarrow} = 0$.

   To achieve this, first one finds the direction of steepest descent in the complex plane $\mathbb{C}_r$ for which $\lim_{r\to\infty} \frac{R_{\rightarrow}}{R_{\leftarrow}} = r^{-4i\,\omega\,M+2} e^{-2i\omega\,r} = 0$ tends to zero most quickly: $\sin(\arg(\omega)+\arg(r)) = -1$. This gives us a relation $r = |\,r\,|\; e^{3/2i\pi - i\,\arg(\omega)}$ ([62]) between ω and r which is exact only if one uses the first term of the asymptotic series for the confluent Heun function (i.e. HeunC ~ 1). More details about this approximation can be found in the next section.

   Then, it is enough to solve :

$$C_{\leftarrow} = r^{2+i\,\omega+\frac{2i\,m\,a+i\,\omega}{r_+-r_-}}\,\mathrm{HeunC}(\alpha,\beta,\gamma,\delta,\eta,z) = 0, \tag{4.4}$$

   in order to completely specify the spectra $\{\omega_{n,m}, E_{n,m}\}$, with $r = 110\,e^{3/2i\pi - i\,\arg(\omega)}$ (we use $|r| = 110$ as the actual numerical infinity and $M = 1/2$).

4.2.3 The epsilon-method

Equation (4.4) relies on the direction of steepest descent defined by the phase condition $\arg(r)+\arg(\omega) = 3/2\pi$. This approximate direction was chosen ignoring the higher terms in the asymptotic expansion of the solution around the infinity point, therefore, one can expect that the true path in the complex plane may not be a straight line but a curve. In principle, the spectrum should not depend on this curve, as long as r stays in the sector of the complex plane where $\lim_{r\to\infty} \frac{R_{\rightarrow}}{R_{\leftarrow}} = 0$, i.e. as long as $\pi < \arg(r)+\arg(\omega) < 2\pi$, with only the convergence of the algorithm being affected. Numerical exploration of that limit evaluated with the first 3 terms in the asymptotic expansion of the appropriate confluent Heun functions for the

modes ω_n, $n = 0..18$ when there is no BH rotation ($a = 0$), and for some modes when there is rotation, confirms that indeed the limit remains approximately zero in the whole interval $\pi + 0.1 < \arg(r) + \arg(\omega) < 2\pi - 0.1$.

The spectrum obtained numerically in this interval, however, depends in a non-trivial way on this curve. The complications are partially due to the appearance of branch cuts in the numerical realization of the confluent Heun functions in MAPLE, where as we mentioned, one of the branch cuts is fixed to be the semi-infinite interval $(1, \infty)$ on the real axis. In the case of QNMs of nonrotating BHs [109, 110], it was observed that when those branch cuts are found near a frequency (since the radial variable, r depends on the frequency ω, the branch cuts appear also in the complex ω-plane), they have serious effect on it, leading to the disappearance or translation of certain modes. Here we continue the study of the effect of the branch cuts on the spectra and we define the equation describing some of them.

Here introducing the parameter epsilon in the phase condition leads to:

$$\arg(r) + \arg(\omega) = \frac{3+\varepsilon}{2}\pi, \qquad \text{for } |\varepsilon| < 1, \tag{4.5}$$

which differs from the one used in the nonrotating case by the sign in front of ε. Using the ε-method, one can change the location of the branch cut with respect to the eventual roots of the system and this way try to minimize the effect of the jump discontinuity of the radial function [3]. Using ε, one can also explore the whole sector $\pi < \arg(r) + \arg(\omega) < 2\pi$, i.e. effectively moving $r = |r| e^{i \arg(r)}$ in the complex plane and this way test the numerical stability of the QNM spectrum with respect to the position of the branch cuts of the radial function.

Using the parameter ε, the observed branch cuts in the realization of the confluent Heun function in MAPLE are as follows:

1. For r–real, one encounters one of the branch cuts of the confluent Heun function. The equation of the line of this branch cut is: $\Im(\omega)/\Re(\omega) = \tan(3/2\pi + \varepsilon\pi/2) = -\cot(\varepsilon\pi/2)$. This line rotates when ε changes.

2. If $\Im(\omega) = 0$, then one encounters the branch cut of the argument-function. In this case the branch cut is defined for $\Re(\omega) = (-\infty, 0)$. This branch cut, however, affects the solutions only very close to $a = M$ where the frequencies can become almost real.

3. If $\Re(\omega) = 0$ and $\Im(\omega) = 2n$, $n = 1, 2, 3..$, then one can have $\Im(r) = 0$ for certain values of ε and thus reach the branch cut of the confluent Heun function on the real axis. This condition can affect modes which are very near the imaginary axis (for example, similar condition holds around the algebraically special mode for a nonrotating BH).

4. Additional branch cuts may appear in the cases where $\Im(r^k) = 0$, for k–noninteger or complex (where $z = 1 - r$). Those branch cuts depend on

[3] Here, the radial function refers to the solutions of the radial equation and not to the differential equation itself.

the numerical realization of the confluent Heun function in MAPLE and the equations of their lines can be obtained numerically from the values of the function for each ε. For example, one such branch cut was observed for $\Im(\omega)/\Re(\omega) \approx \tan(1.419 + \varepsilon\pi/2)$.

Although the study of the full effect from the movement of the branch cuts on the EM spectrum of KBH, as it was done in the case of gravitational perturbations of nonrotating black holes, is outside the scope of this work, some preliminary results on the issue can be found in the Appendix.

4.2.4 Numerical algorithms

The spectral equations we need to solve to find the spectrum $\omega_{n,m}(a)$ for $M = 1/2$ are Eqs.(4.2) and (4.4). This system represents a two-dimensional connected problem of two complex variables – the frequency ω and the separation parameter E – and in both of its equations one encounters the confluent Heun function and in the case of the TAE – their derivatives.

A system like that cannot be easily solved by conventional methods like the Newton method and the Broyden method, as outlined in [109] and [128], since they do not work well with the confluent Heun function in MAPLE. For this reason, our team developed a new method, namely the two-dimensional Müller algorithm which proved to be much better adapted to work with those functions. The details of the algorithm can be found in [128, 109, 110], but for completeness, we will mention only that it relies on the Müller method which is a quadratic generalization of the secant method having better convergence than the latter. The new algorithm does not need the evaluation of derivatives, thus avoiding one of the biggest problems when using the confluent Heun function in MAPLE. Clearly, in the system we solve the angular spectral equation (Eq. (4.2)) includes derivatives, but in this case, they remain in the domain $|z| < 1$, where they can be evaluated correctly (for most values of the parameters) and with precision comparable to that of the radial function. It is important to note that both ω, E are found directly from the spectral system (Eqs. [(4.2) and (4.4)]) and with equal precision. [4] [5]

4.2.5 Numerical results for electromagnetic QNMs

While the evaluation of QNMs is not new to physics, the actual numbers published for EM perturbations of KBH are scarce. Because of this, for comparison, we use

[4] The algorithm is realized in MAPLE code and the numbers presented below are obtained using MAPLE 13 on the computer cluster Physon. The software floating point number is set to 64 (unless stated otherwise), the precision of the algorithm – to 15 digits.

[5] An important precaution when working with the confluent Heun function in MAPLE is that its precision or over-all behavior may depend on different factors which are not always under user's control [109]. From our observations, it seems that one can trust around 11-12 digits of the frequencies at the worst, usually around 13 digits. The points we present are the maximum we could get out of MAPLE, but future improvements in MAPLE's code may significantly expand the area of application of the method and/or also its precision.

the numbers published by Berti et al. [65, 94], the numerical data can be found on http://www.phy.olemiss.edu/~berti/qnms.html. Those numbers were obtained using the continued fraction method which is still considered as the most accurate method for obtaining the QNMs from the KBH. The available control frequencies are $n = 0..6$ for $l = 1$ and $n = 0..3$ for $l = 2$. Using those "control" numbers denoted as $\omega^B_{n,m}, E^B_{n,m}$ one can easily check the precision of the method.

The first 10 modes of the spectrum obtained using the new method in the interval $a = [0, M)$ can be found on http://tcpa.uni-sofia.bg/conf/research. In the Appendix, one can find some of the QNMs for specific values of a.

4.2.5.1 Non-rotating BH

It is already well known that when there is no rotation ($a = 0$) the electromagnetic QNMs come in pairs symmetrical to the imaginary axis $\omega_{n,m} = \pm|\Re(\omega_{n,m})| + i\Im(\omega_{n,m})$ ($n = 0, 1..$ numbering the mode). In this case the system reduces to one equation – the radial function (4.4) (for $E = l(l+1), l = 1, 2..$) solved here using the one-dimensional Müller algorithm.

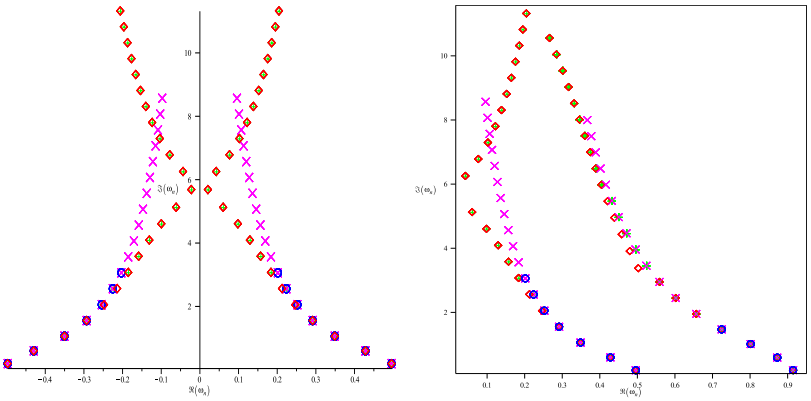

(a) l=1 (b) l=1,2

Figure 4.6: QNMs for $a = 0$, for $m = 0, 1, 2$. The red diamonds are obtained for $\varepsilon = 0$, the green crosses – for $\varepsilon = 0.05$, the magenta diagonal crosses – for $\varepsilon = 0.15$. With blue circles are the control frequencies $\omega^B_{n,m}$. Some points cannot be differed because for them, the numbers for different ε coincide with precision higher than 10 digits. Clearly, for the higher modes, one obtains different spectra for different ε

The results can be seen on Fig. 4.6 a) and b), where we plotted the QNMs for $m = 0, 1, 2$ and $l = 1, l = 2$. The behavior of the modes resembles the behavior of the gravitational QNMs. A numerical comparison with the frequencies obtained by Berti et al. shows that the average deviation is $|\omega^B_{n,m} - \omega_{n,m}| \approx 10^{-10}$ for the first 4 modes ($n = 0..3$, $l = 1, 2$). For modes with $n > 3$ (i.e. $n = 4..6$ for $l = 1$), however, there is an unexpected deviation which starts for $n = 4$ from $|\omega^B_{4,m} - \omega_{4,m}| \approx 0.007$ and grows to $|\omega^B_{6,m} - \omega_{6,m}| \approx 0.022$ for the last available control mode.

To study this systematic deviation, we employed the ε-method to test the stability of those frequencies with respect to small deviations in the phase-condition. The results for ε: $0, \pm 0.05, \pm 0.15$ are plotted on Fig. 4.6 a) and b). From there one can see that for $n > 3$ the best coincidence with the control frequencies $\omega^B_{n,m}$ occurs for $\varepsilon = \pm 0.15$, while for $n < 3$ the modes obtained for the different values of ε are equal and coincide with $\omega^B_{n,m}$.

Similarly to the gravitational perturbation for nonrotating BH ([109]), the dependence $\omega(\varepsilon)$ in the electromagnetic case is not a trivial one. Here, only the case when there is no rotation ($a = 0$) allows studying in detail this dependence, since when there is rotation finding the roots of the system in a whole interval for ε is strongly limited by the computational cost of the algorithm. Exploring $a = 0$, however, allow us to gather important intuition on the behavior of the QNMs under changes in ε.

A more detailed study on both this case and the case with rotation, can be found in the Appendix .1.2.

The most important results from this study are:

1. Each mode $\omega_{m,n}$ can be found in certain interval of ε: $\Delta^{\varepsilon}_{m,n} = [\varepsilon^{in}_n, \varepsilon^{fin}_n] \subseteq (-0.8, 0.8)$. Outside this interval, this mode is not a root of the system.

2. The modes $\omega_{m,n}$ with $n < N$ (N depends on $\{m, l\}$), with high precision do not depend on ε and both signs of their real parts are obtainable with any sign of ε.

3. The modes with $n \geq N$ depend on the sign of ε as: $\omega_{m,n}(\varepsilon) = \mathrm{sgn}(\varepsilon)|\Re(\omega_{m,n})| + i\Im(\omega_{m,n})$ (i.e. frequencies with positive real parts can be obtained only with positive epsilon)[6].

4. The interval for $\Delta^{\varepsilon}_{m,n}$, where a mode $\omega_{m,n}$ with certain sign of its real part can be found, shortens with the increase of n.

5. Studying $\omega_{m,n}(\varepsilon)$ for $\varepsilon \in \Delta^{\varepsilon}_{m,n}$ shows that the effect due to ε can be very small in certain ranges, but it is above the numerical error.

6. The dependence $\omega_{m,n}(\varepsilon)$ in the whole interval $(-0.8, 0.8)$ of applicability of the method, can be of two types – 1) step-wise change of the values of the frequency for ε crossing the left(right) end of the intervals $\Delta^{\varepsilon}_{m,n}$ for frequencies with positive(negative) real parts. This behavior has been observed also inside the intervals $\Delta^{\varepsilon}_{m,n}$ for some $\{m, n\}$ 2) smooth transition for $\varepsilon \in \Delta^{\varepsilon}_{m,n}$ (for the whole interval or parts of it) where the frequency remains stable with at least 9 digits of precision.

[6]The change of the sign in front of ε compared to the non-rotating GW case ($s = -2$) comes from the change of the sign in the phase condition

4.2.5.2 Rotating KBH

The results presented here were obtained for $a = [0..M)$ for 3 different values of $|\varepsilon| = 0, 0.05, 0.15$ (where the positive ε are used for frequencies with positive real part and vice versa, negative ε – for the frequencies with negative real parts).

The results can be seen on the figures below (Figs. 4.7-4.16).

When $a \neq 0$, the symmetry with respect to the imaginary axis $\omega^{1,2}_{m,n}(0) = \pm|\Re(\omega_{m,n})| + i\Im(\omega_{m,n})$ breaks down, but it is replaced by the symmetry:

$$\{\Re(\omega^j_{m,n}), \Im(E^j_{m,n}), m\} \rightarrow \{-\Re(\omega^j_{m,n}), -\Im(E^j_{m,n}), -m\},$$

where $j = 1, 2$ coincides with the upper index of $\omega^{1,2}_{m,n}(0)$. Thus, to study the complete behavior of the modes for $a \in [0, M)$, it is enough to trace both symmetric frequencies in the pair corresponding to each $\{m, n\}$ for $a = 0$, for only $m > 0$ (the index l here is omitted to simplify the notation, but everywhere in the text, if not explicitly stated otherwise, we compare only frequencies with the same l.)

The parameter ε, for rotating BH, has an even more significant role than the nonrotating case, since it does not merely translate modes with respect to each other, but for some modes, the frequencies obtained for the 3 values of ε have different behavior with respect to changes in the rotation. Some details can be found in the Appendix (.1.3).

As in the case $a = 0$, one sees that for modes with $n < N$, $\omega^0_{m,n}(a), \omega^{0.05}_{m,n}(a), \omega^{0.15}_{m,n}(a)$[7] coincide for equal $\{m, n\}$ (Fig. 4.7), while when $n \geq N$, the modes $\omega^{\varepsilon}_{m,n}$ obtained for different values of the parameter ε differ (Fig. 4.8). N depends on m, n and generally it is for $N = 2..4$ when one of the modes $(\omega^0_{m,n}, \omega^{0.05}_{m,n}, \omega^{0.15}_{m,n})$ splits up from the rest (Note, here we discuss mostly the frequencies, but the separation parameters $E_{m,n}$ also depend on ε as the figures show.).

It is important to note that for $m = 0$, in the modes $n \geq 3$, one observes loops. An example can be seen on Fig. 4.9. Those loops appear in all the higher modes, and their position depends on n. Because those loops require a finer structure of the plot (i.e. smaller step), on the plots Fig. 4.10, Fig. 4.11 and Fig. 4.14, we will plot only the points before the first loop observed in each curve. On Fig. 4.14 one can see the points for $l = 1, 2, m = 0, 1$ plotted together.

From the radial boundary conditions it follows that only frequencies for which $\Re(\omega) \notin (0, -m\frac{a}{2Mr_+})$ correspond to black hole boundary conditions. Figure 4.15 a) shows that the so obtained spectrum obeys this condition. A deviation from this condition was observed in [97], where some of the frequencies describing primary jets crossed the line defined by $-m\frac{a}{2Mr_+}$, thus corresponding to a white hole solution. For the QNM spectrum, however, this is not the case and the spectrum corresponds to perturbation of a black hole.

From the same figure one can see in the negative sector of the plot that the real parts of the QNMs for increasing n seem to tend to the line $-m\frac{a}{2Mr_+}$, which requires further investigation for $n > 10$. For the positive sector (i.e. the frequencies

[7] where $\omega_{m,n}(\varepsilon) = \omega^{\varepsilon}_{m,n}$ to avoid confusion with $\omega_{m,n}(a)$

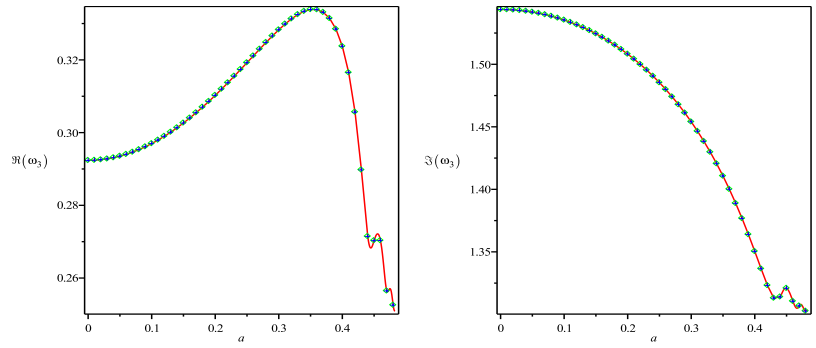

(a) $\Re(\omega_{0,3})(a)$ (b) $\Im(\omega_{0,3})(a)$

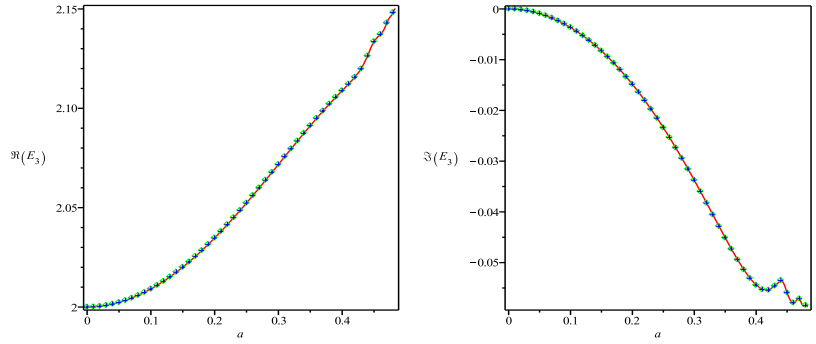

(c) $\Re(E_{0,3})(a)$ (d) $\Im(E_{0,3})(a)$

Figure 4.7: On the plots the real and imaginary parts of $\omega_{0,3}(a)$ and $E_{0,3}(a)$ when the rotation changes in the interval $a = [0, M)$. Here, with red line are denoted the points obtained for $\varepsilon = 0$, with blue crosses – those for $\varepsilon = 0.05$ and with green diamonds – those for $\varepsilon = 0.15$. The modes obtained for the 3 values of ε coincide

with positive real parts) we were not able to trace the frequencies with high n near $a \to M$, thus we cannot confirm the relation $\Re(\omega) = m$ for $a \to M$ observed in [59].

Finally, obtaining the modes in the limit $a \approx M$ could be of serious interest, if one is to compare the EM QNMs with the spectra obtained from astrophysical objects, but it is also technically challenging. This happens because for $a = M$ the TRE changes its type and near this limit the confluent Heun function becomes numerically unstable since these functions are transforming to the double confluent Heun ones. Because of this, the examination of the limit $a \to M$ for modes with high n is impossible with current numerical realization of that function in MAPLE. For the lowest modes, however, the function is stable enough in the interval $a \in [0.49, 0.4995]$ and the results of the numerical experiment for $m = 1$ are plotted on Fig. 4.16. As expected, for $n = 0$, for $a > 0.91M$ the imaginary part of the frequency quickly tends to zero, thus proving that for extremal objects, the perturbations damp very slowly. For the other two modes, it also seems to tend to zero, although somewhat slower than $n = 0$. In physical units, the difference between the 3 modes for $a =$

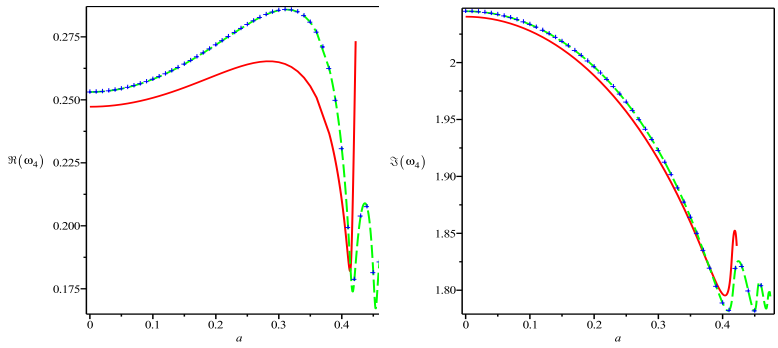

(a) $\Re(\omega_{0,4})(a)$ (b) $\Im(\omega_{0,4})(a)$

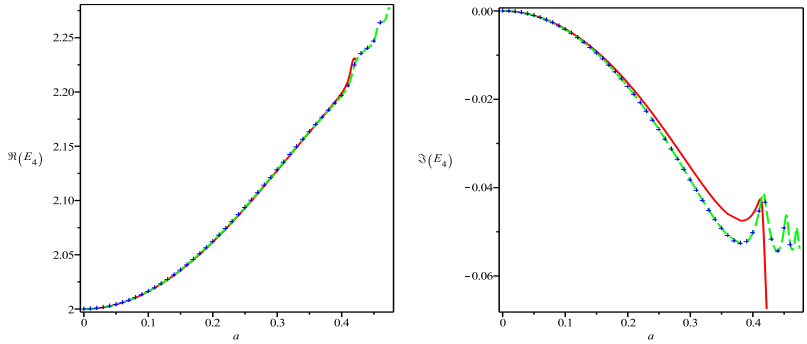

(c) $\Re(E_{0,4})(a)$ (d) $\Im(E_{0,4})(a)$

Figure 4.8: The plots depict the real and imaginary parts of $\omega_{0,4}(a)$ and $E_{0,4}(a)$ for $a = [0, M)$. With red lines are denoted the points obtained for $\varepsilon = 0$, with blue crosses – those for $\varepsilon = 0.05$ and with green dashed lines – those for $\varepsilon = 0.15$. The points obtained for the different values of ε differ

0.4995 is only 6Hz ($\omega_{1,1} \approx 1.582kHz$), but the damping times of the first mode is approximately 4.86 times bigger than that of the third and is $t_{1,1}^{damp} \approx 4.2ms$ for KBH with mass $M = 10M_{\odot}$. The frequencies in physical units, for some other values of the rotational parameter, can be found in the tables 2 in the Appendix .1.1.

While the analytical study of the extremal case is outside the scope of this work, one can find such analytical treatment of the issue in [61, 64]. In both articles, one deals with approximations of the exact solutions of the radial equation, obtained under certain assumptions – be it through the continued fraction method in the limit $a \to M$ ([61]) or through a particular case in which the solution of the radial equation for $a \to M$ can be written in terms of confluent hypergeometric functions ([64]). Both methods seem to describe well the numerical results, but further investigation through the exact solutions written in terms of double confluent Heun functions and their properties, is needed to properly understand this interesting from observational point of view case.

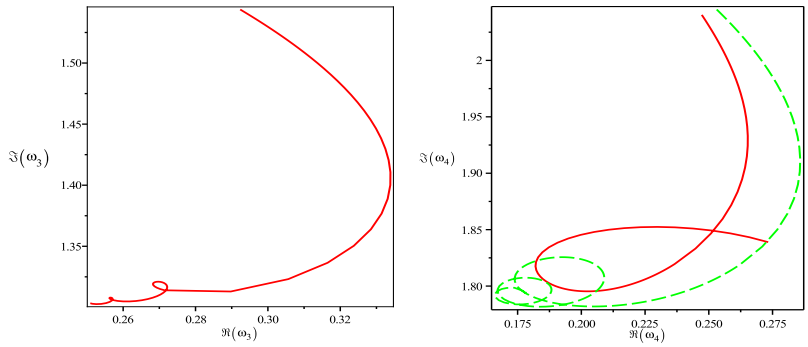

Figure 4.9: Example of the loops observed for $m = 0$. The figure shows the complex plots of $\omega_{0,3}(a)$ and $\omega_{0,4}(a)$ for $a = [0, M)$. The red lines are the points corresponding to $\varepsilon = 0$, the green dashed line – those to $\varepsilon = 0.15$. For $n = 3$, the results for $\varepsilon = 0, 0.15$ coincide and thus only the points for $\varepsilon = 0$ are plotted

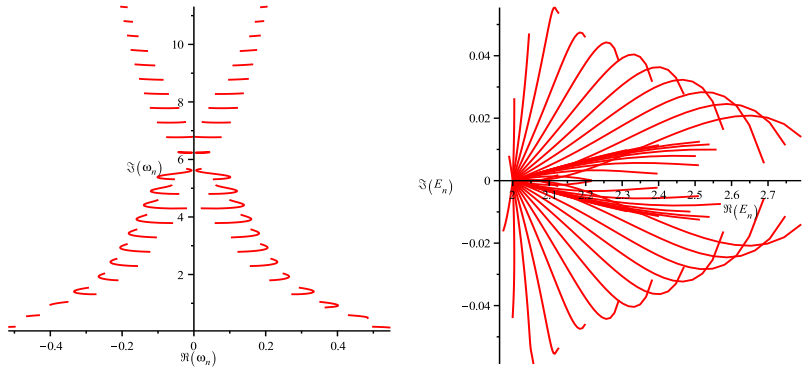

Figure 4.10: Complex plots of $\omega_{0,n}(a)$ and $E_{0,n}(a)$ for $a = [0, M)$, $l = 1$, $\varepsilon = 0$, $n = 0..21$

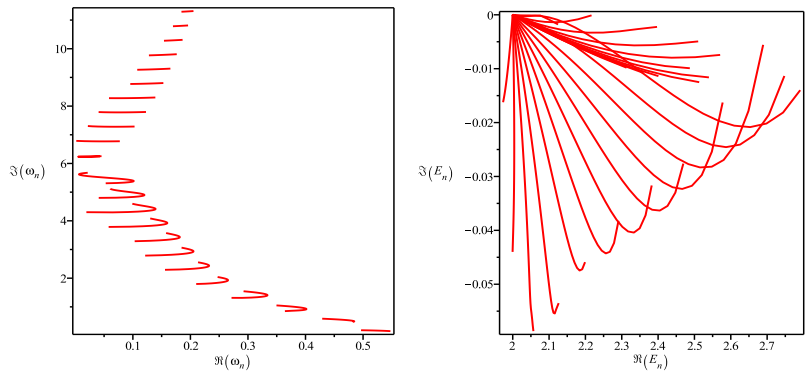

Figure 4.11: Complex plots of $\omega_{0,n}(a)$ and $E_{0,n}(a)$ for $a = [0, M)$, $l = 2$, $\varepsilon = 0$

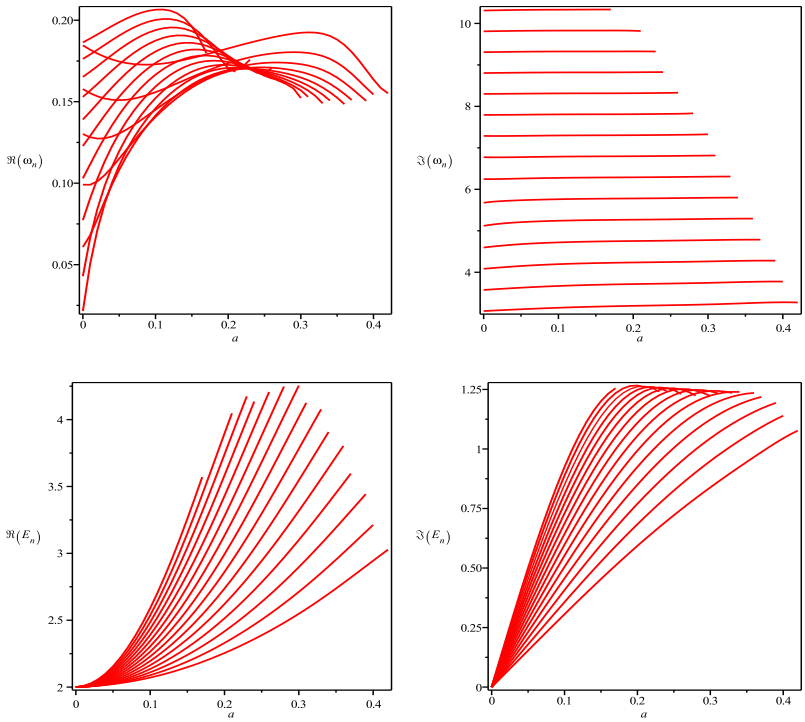

Figure 4.12: The plots show the real and the imaginary parts of $\omega_{1,n}(a)$ and $E_{1,n}(a)$ for $a = [0, M)$ for the modes $n = 6..20$

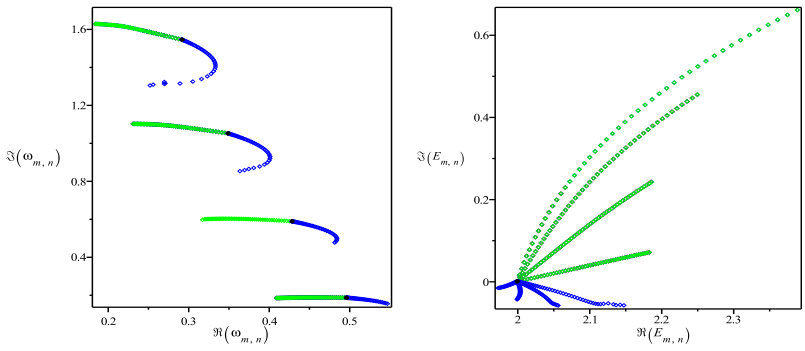

Figure 4.13: Complex plots of $\omega_{m,n}(a)$ and $E_{m,n}(a)$ for $a = [0, M)$, $n = 0..3$. With blue are the points with $m = 0$, with green – those with $m = 1$. The black solid circle denotes $a = 0$

4.2.5.3 Algebraically special modes and branch cuts

The algebraically special (AS) modes are obtained from the condition that the Starobinsky constant vanishes ([43]) and they correspond to the so called total transmission modes (TTM) – modes moving only in one direction: to the right or to the left. In the case of gravitational perturbations ($s = -2$) from nonrotating BH,

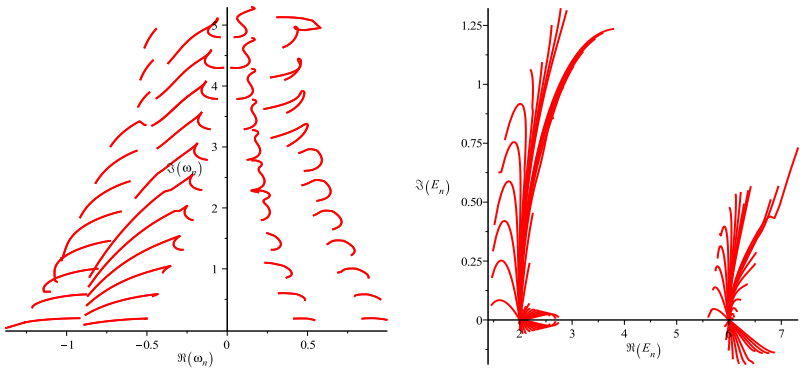

Figure 4.14: Complex plot of $\omega_{m,n}(a)$, $E_{m,n}(a)$ for $a=[0,M)$, $m=0,1$, $l=1,2$, $n=0..10$

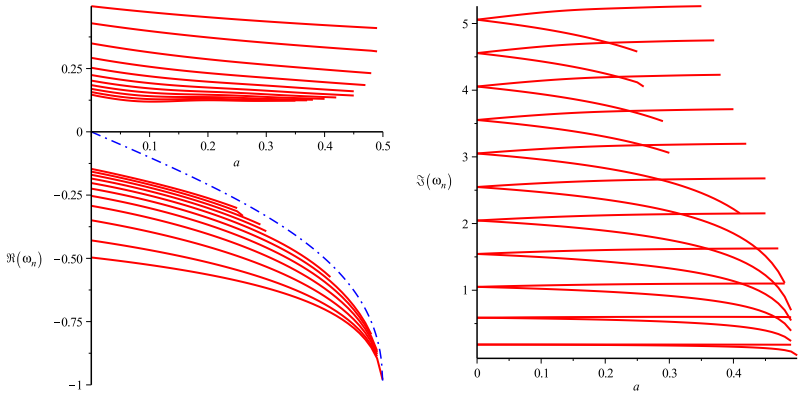

Figure 4.15: On the plots: with red lines – $\Re(\omega_{1,n})(a)$ and $\Im(\omega_{1,n})(a)$ for $a=[0,M)$, $n=0..10$ and with blue dashed line $-m\frac{a}{2Mr_+}$ for $m=1$

since the 9^{th} QNM coincides approximately with the theoretically expected purely imaginary AS mode, there were speculations that the two modes coincide (see [59] for a review, and also [129, 130]). A study of this mode in the case of gravitational perturbations of KBH showed numerical peculiarities as the "doublet" emerging from the "AS mode" for $m>0$ (see [59]) and also unexplained "spurious" modes, blamed to numerical inaccuracies.

For electromagnetic perturbations, the possibility of appearance of the algebraically special modes has not been discussed much, since in the limit $a\to 0$, the Starobinsky constant does not vanish for purely imaginary modes (in fact, for $a=0$, the Starobinsky constant does not depend on ω at all, see Eq. (60) [43] p.392) and there appears to be no correlation between TTM and QNM modes [131]. There is, however, one important parallel between the electromagnetic and the gravitational case. For the nonrotating gravitational case, Maassen van den Brink [129, 130] found that the peculiarities of the 9^{th} mode are due to the branch cut in the asymptotics of Regge-Wheeler potential, which the method of the continued fraction is not adapted

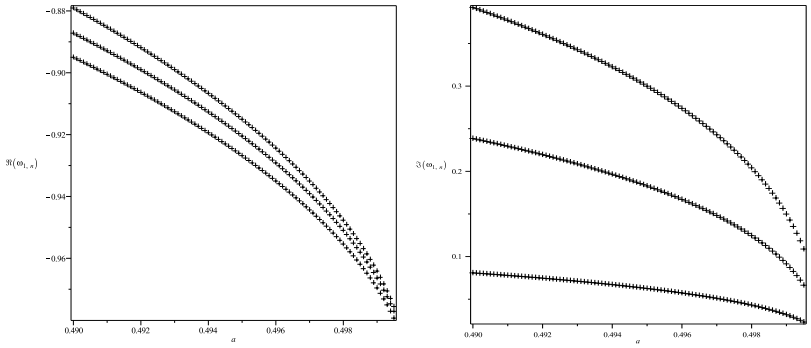

Figure 4.16: On the plot $\Re(\omega_{1,n})(a)$ and $\Im(\omega_{1,n})(a)$ for $a = [0.49, 0.4995]$ for the modes $n = 0, 1, 2$, $m = 1$

to handle. This result was confirmed by the use of the ε-method for GW perturbations of non-rotating BH where the AS character of the 9^{th} mode was disproved. Using the ε-method, one sees that this result is not limited to the gravitational case and the branch cuts play an important role for the electromagnetic QNMs as well.

If one considers ε as a parameter controlling the location of the branch cut with respect to certain QNM [8], using the equations of the branch cuts discussed in section "The epsilon-method", one can find how "close" a certain branch cut is in the complex ω-plane for each mode. In the gravitational case [110], the supposed AS mode is the one with the smallest real part and for it the value of ε for which one observes the jump discontinuity is also very small. Therefore, one can expect that for this mode, very small variations in the phase-condition can change the leaf of the multivalued function and thus to lead to a different ω from the expected.

In the EM case, one can also find a mode with a very small real part – $n = 11$ with $\Re(\omega_{0,11}) = .0215$ (evaluated for $\varepsilon = 0.15$), for which one encounters the jump discontinuity very close to the imaginary axis at $\varepsilon = 0.0024$. In this case, one observes particularly interesting dependence on ε – as showed on Fig. 4.6 a) – for $\varepsilon \leq 0.05$ the mode $n = 11$ separates the lower QNM branch from the upper branch similarly to the way the so-called AS mode separates the QNM branches in the gravitational case [60], but if one uses $\varepsilon = 0.15$ there is no such separation. Thus, for $\varepsilon = 0$ one finds a similarity between the EM and the gravitational cases. This similarity, however, is due to the appearance of branch cuts in the radial function in both cases and not to some special properties of the mode in question (i.e. $n = 11$ for $s = -1$ and $n = 8$ for $s = -2$). This is because in the EM case, there is no theoretical justification for $n = 11$ to be an AS mode. In fact when the real part of that mode is very small ($\varepsilon \leq 0.05$), its imaginary part deviates from the value of $6i$ and vice versa – when the real part is not so small ($\varepsilon = 0.15$), the imaginary part tends to $6i$, see Fig. 4.6. Therefore, for all values of ε, this mode deviates from a purely imaginary, integer number.

[8] Recall that $r \sim \exp(i \arg(\omega))$ and thus by changing $\omega_{m,n}$ and ε, one changes the position in the r-complex plane

An important note is that usually when studying purely imaginary frequencies, most methods do not work well, but in our case, there is no such problem, since we have a way to control some of the discontinuities in the solution of the radial function. If we are to continue the analogy with the gravitational case, studying how the mode $n = 11$ evolves with the increase of the rotation shows that it does no differ from the other modes. Although we didn't search specifically for doublets like the ones mentioned in [59], most of the modes with $n > N$ can be considered as doublets, since we obtain distinct curves in the complex $\omega-$plane for different ε. Furthermore, in certain ranges of ε we found two very close frequencies (i.e. corresponding to the same n) as roots of the system for the same ε. The details for one of those cases can be found in the Appendix, but this also resembles the doublet found in the gravitational case, here found for $n = 10$.

Focusing on the other peculiarity observed in [59] – the so called "spurious" modes the study of the frequencies in the interval $\varepsilon = -0.9..0.9$ for $a = 0$ showed that indeed when varying ε one may observe a number of frequencies around a certain mode. While the definition of "spurious" is unclear, in the case $a = 0$, $n = 2$, for example, one finds 3 frequencies (we omit here the separation constant which also differs): $0.3716378885 + 1.0257637188i, 0.3610740790 + 1.0392917852i, 0.3495471352 + 1.0503751987i$ (corresponding to $\varepsilon = -0.22, -0.21, -0.2$, respectively), where the precision in all cases is 15 digits. Such examples occur for all modes, with different roots found stable in different intervals for ε. In some cases, one may consider those results as dependence of the frequency on ε since the transition between those roots appears to be smooth [9]. In other cases, however, the transition appears to be step-wise in the scale of variation of ε we studied. While there is no analytical explanation for this behavior yet, it appears to be related to the branch cut in the radial function which is moved by the parameter ε. Thus, even if the phenomena of the "spurious" modes in [59] could indeed be blamed to numerical problems of the algorithm used in that article ([59]), exploring the roots with the ε-method showed that a similar result can be obtained also in the EM case using a very different method. The reason for the observed peculiarities in the behavior of the spectrum of QNMs, due to the variation of epsilon, may be the complex character of the used analytical functions (the confluent Heun functions) in the vicinity of the irregular singular point $r = \infty$ in the complex r-plane.

Considering all the numerical peculiarities demonstrated above, the use of the ε-method poses a very serious question in front of the astrophysical application of the spectra – if one is to compare the numerical results with some observational frequencies, which ε should be trusted? In our numerical experiments, we were able to obtain both the frequencies obtained with well-established methods with a precision higher than 7 digits, and also other, significantly deviating from them frequencies, which have qualitatively different behavior with respect to changes in the

[9] In the mentioned above case ($n = 2$) one observes such smooth transitions: for $\varepsilon = -0.3..-0.25$ one finds the root $.3901344442 + .9754977543i$ which has 9 stable digits in this interval, which then goes smoothly to the "official" mode $.3495471352 + 1.0503751987i$, stable in the widest interval – $\varepsilon = -0.2..0.7$, through the numbers mentioned above for $\varepsilon = -0.22, -0.21, -0.2$

rotation of the KBH. Both results are stable in different ranges for ε, thus requiring new criteria for sifting out the physical modes based on better understanding of the behavior of the radial function in the complex plane of the radial variable. Such a study is outside the scope of the current work which aims to demonstrate the dependence of the method for obtaining the frequencies with respect to changes in the phase-condition and thus to provoke work in this area.

4.2.6 Summary of the results

From the recent developments in the field of gravitational waves detection it is clear that finding the EM counterpart to those events can prove to be very useful. In this case, it is needed to better understand the fundamental physics of quasi-normal ringing. In this section again were demonstrated the advantages of the new approach to finding the QNMs for the KBH based on directly solving the system obtained by the analytical solutions of the TRE and TAE in terms of the confluent Heun function. This approach is more traditional (i.e. imposing directly the corresponding boundary conditions on the exact analytical solutions of the problem) and hence it should allow better understanding of the peculiar properties of the EM QNMs and the physics they imply.

It was shown that using this approach, one can reproduce the frequencies already obtained by other authors, but without relying on approximate methods. Particularly important is the ability to impose the boundary condition *directly* on the solutions of the differential equations. We require the standard regularity condition on the TAE and we explore in detail the radial boundary condition (the BHBC). Critical in it is the use of the direction of steepest descent, which secures the purely outgoing wave at infinity. By using small deviations from this direction (and the phase-condition it defines), we were able to move around the branch cut in the solutions of the radial equation and thus to study its effect on the so obtained spectra. While this movement had no significant effect for the lower modes $n < 3$, for the higher modes it led to significant deviations from the already published results. This behavior is persistent for the modes with $m = 0, 1, 2$ and $l = 1, 2$. This observation raises the important question: What are the electromagnetic QNMs for which one has to look in astrophysical data. Also interesting is that while the ε-method leads to significant changes of the frequencies $\omega_{m,n}$, it affects much less the separation parameter $E_{m,n}$ which here for the first time was obtained directly as a solution of the two-dimensional system without any prior approximations for it.

Another general result is that the confluent Heun function proved to be an effective tool for physical problems. Even though its MAPLE realization still has many flaws, its precision proved to be good enough to repeat the already published results, and also studying the solutions, we were able to reveal new properties of the numerical stability of the EM QNMs with respect to changes in the phase-condition.

An interesting question is the results obtained using this method for $a > M$ or the so called naked singularity regime. Preliminary results show that the method is applicable in this case as well and the results will be published elsewhere.

.1 Appendix: Electromagnetic QNMs

.1.1 Tables of the obtained QNMs

In the table 2 are presented some of the values obtained for the EM QNM, converted to physical units using the relations:

$$\omega^{phys} = \Re(\omega)\frac{c^3}{2\pi\, G\, M}$$

$$\tau^{phys} = \frac{1}{\Im(\omega)}\frac{GM}{c^3}.$$

Note that in those formulas a factor of 2 is missing because the EM QNMs were obtained for $M_{KBH} = 1/2$ and not for $M_{KBH} = 1$. Then if M is the mass of the object in physical units, $M_\odot$ – the mass of the Sun ($M_\odot = 1.98892\,10^{30}[kg]$) and $G = 6.673\,10^{-11}[\frac{m^3}{kg\,s^2}], c = 2.99792458\,10^8[m/s]$, one obtains

$$\omega^{phys} \approx \frac{32310}{M/M_\odot}\Re(\omega)[Hz],$$

$$\tau^{phys} \approx \frac{0.4925\,10^{-5}\,M/M_\odot}{\Im(\omega)}[s].$$

The frequencies and the damping times in the table are calculated for $M = 10M_\odot$.

.1.2 The ε-method for $a = 0$

Let us denote the dependence $\omega(\varepsilon)$ as ω_n^ε (so that it differs from $\omega_n(a)$).

First, one can compare the frequencies obtained for $\varepsilon = 0, 0.05, 0.15$ for different m:

for the case $m = 0$: $|\omega_n^0 - \omega_n^{0.05}| \approx 10^{-10}$ for all n, but $|\omega_n^0 - \omega_n^{0.15}| \approx 10^{-10}$ only for modes with $n < 4$, and $|\omega_n^{0.05} - \omega_n^{0.15}| \approx 10^{-10}$ for $n < 6$.

for the case $m = 1$: $|\omega_n^0 - \omega_n^{0.05}| \approx 10^{-10}$ and $|\omega_n^0 - \omega_n^{0.15}| \approx 10^{-10}$ for $n = 0..3$ and $n = 6..11$, and $|\omega_n^{0.05} - \omega_n^{0.15}| \approx 10^{-12}$ for $n < 12$.

for the case $m = 2$: $|\omega_n^0 - \omega_n^{0.05}| \approx 10^{-10}$ for $n = 0..3$ and $n = 6..14$, $|\omega_n^0 - \omega_n^{0.15}| \approx 10^{-10}$ for $n < 4$, and $|\omega_n^{0.05} - \omega_n^{0.15}| \approx 10^{-10}$ for $n < 6$.

The modes not enlisted above, such as ω_n^0 and $\omega_n^{0.15}$ for $n > 4$, $m = 1$, show significant deviation from the control results.

Clearly, the modes for different m demonstrate different properties with respect to ε. Such dependence on m is unexpected, since in equation (4.3), m is always coupled with a, so for $a = 0$, those frequencies should coincide. This indeed happens with precision 10^{-12} for frequencies evaluated for the same ε. For $\varepsilon \neq 0$, however, deviation may occur because different signs of ε may lead to different roots. [10]

[10] A peculiar case is the difference between $m = 0$ and $m = 1$, for $\varepsilon = 0.15$, where while most of the modes coincide with at least 11 digits, the frequencies $n = 6..11$ show small deviation (≈ 0.1), which is probably due to numerical instability in the subroutine evaluating the confluent Heun function in MAPLE.

$n=0$									
	$m=0$			$m=-1$			$m=1$		
a/M	$\omega^{phys}_{m=0}$[Hz]	$\tau^{phys}_{m=0}$[ms]	$\delta(\omega^{\varepsilon})$	$\omega^{phys}_{m=-1}$[Hz]	$\tau^{phys}_{m=-1}$[ms]	$\delta(\omega^{\varepsilon})$	$\omega^{phys}_{m=1}$[Hz]	$\tau^{phys}_{m=1}$[ms]	$\delta(\omega^{\varepsilon})$
0	802.1512449166	0.5325890917	10^{-10}	802.1512449166	0.5325890917	10^{-10}	802.1512449167	0.5325890917	10^{-10}
0.2	804.9393652797	0.5343356142	10^{-10}	849.8315682698	0.5388677452	10^{-10}	763.6902591869	0.5299212818	10^{-10}
0.6	829.2637578502	0.5526525743	10^{-10}	996.9258848852	0.5772488810	10^{-10}	704.6451920585	0.5313970112	10^{-9}
0.98	884.6086875757	0.6427140687	10^{-9}	1445.8841670353	1.2178343064	10^{-11}	661.8628389523	0.5373275077	10^{-4}
$n=3$									
	$m=0$			$m=-1$			$m=1$		
a/M	$\omega^{phys}_{m=0}$[Hz]	$\tau^{phys}_{m=0}$[ms]	$\delta(\omega^{\varepsilon})$	$\omega^{phys}_{m=-1}$[Hz]	$\tau^{phys}_{m=-1}$[ms]	$\delta(\omega^{\varepsilon})$	$\omega^{phys}_{m=1}$[Hz]	$\tau^{phys}_{m=1}$[ms]	$\delta(\omega^{\varepsilon})$
0	472.3043572607	0.0638131626	10^{-10}	472.3043572599	0.0638131626	0.3	472.3043572609	0.0638131626	10^{-11}
0.2	479.7880705182	0.0641624606	10^{-10}	549.5382706431	0.0658306413	0.3	415.5213067645	0.0624052214	10^{-11}
0.6	530.3546588895	0.0677548111	10^{-11}	792.4033820584	0.0741706889	–	–	–	–
0.98	408.1590806664	0.0756272782	–	–	–	–	–	–	–
$n=7$									
	$m=0$			$m=-1$			$m=1$		
a/M	$\omega^{phys}_{m=0}$[Hz]	$\tau^{phys}_{m=0}$[ms]	$\delta(\omega^{\varepsilon})$	$\omega^{phys}_{m=-1}$[Hz]	$\tau^{phys}_{m=-1}$[ms]	$\delta(\omega^{\varepsilon})$	$\omega^{phys}_{m=1}$[Hz]	$\tau^{phys}_{m=1}$[ms]	$\delta(\omega^{\varepsilon})$
0	254.8509577191	0.0275665662	0.03	254.8509577190	0.0275665662	0.34	254.8509577194	0.0275665662	0.03
0.2	264.6648749590	0.0277638854	0.31	334.8615860768	0.0285332670	0.44	251.7604458626	0.0268474465	0.04
0.6	268.3651895175	0.0294003836	0.02	610.5848397689	0.0318459819	–	291.2755338407	0.0263079796	0.06
0.98	–	–	–	–	–	–	–	–	–

Table 2: Table of the frequencies, ω^{phys}, in Hz , the damping times, τ^{phys}, in miliseconds for some of the modes $n = 0, 4, 7$ and for some chosen values of the rotational parameter in the case $l = 1$. Presented is also $\delta(\omega^{\varepsilon})$, the maximal difference between the modes obtained for the 3 values of $\varepsilon = 0, 0.05, 0.15$ for each a, n, m. The numbers presented here correspond to 10 $M_{\odot}$.

$n=0$						
	$m=0$		$m=-1$		$m=1$	
a/M	$E_{m=0}$	$\delta(E^\varepsilon)$	$E_{m=-1}$	$\delta(E^\varepsilon)$	$E_{m=1}$	$\delta(E^\varepsilon)$
0	$2.0000000000 + 9.410^{-63}i$	10^{-64}	$2.0000000000 + 4.8210^{-63}i$	10^{-64}	$2.0000000000 + 4.8310^{-60}i$	10^{-64}
0.2	$1.9991429248 - 0.0007350608i$	10^{-12}	$1.9460508578 + 0.0193509134i$	10^{-11}	$2.0462372214 + 0.0176327659i$	10^{-11}
0.6	$1.9916552351 - 0.0066017264i$	10^{-11}	$1.7970919424 + 0.0620215234i$	10^{-10}	$2.1232126190 + 0.0478089014i$	10^{-10}
0.98	$1.9734060595 - 0.0162271167i$	10^{-10}	$1.4500680177 + 0.0605778034i$	10^{-11}	$2.1833506585 + 0.0705481152i$	10^{-5}
$n=3$						
	$m=0$		$m=-1$		$m=1$	
a/M	$E_{m=0}$	$\delta(E^\varepsilon)$	$E_{m=-1}$	$\delta(E^\varepsilon)$	$E_{m=1}$	$\delta(E^\varepsilon)$
0	$2.0000000000+9.4410^{-31}$i	10^{-64}	$2.0000000000+4.82\ 10^{-30}$i	10^{-64}	$2.0000000000+4.83\ 10^{-30}i$	10^{-64}
0.2	$2.0090686631 - 0.0036398098i$	10^{-12}	$1.9778301381 + .1550332409i$	0.003	$2.0389149509 + .1531306042i$	10^{-11}
0.6	$2.0717320628 - 0.0337575846i$	10^{-12}	$1.9332832523 + .4598448835i$	10^{-11}	–	–
0.98	$2.1483751533 - 0.0584019594$	–	$1.6286222388 + .6109228338i$	–	–	–
$n=7$						
	$m=0$		$m=-1$		$m=1$	
a/M	$E_{m=0}$	$\delta(E^\varepsilon)$	$E_{m=-1}$	$\delta(E^\varepsilon)$	$E_{m=1}$	$\delta(E^\varepsilon)$
0	$2.0000000000+9.4410^{-31}$i	10^{-64}	$2.0000000000+4.82\ 10^{-30}$i	10^{-64}	$2.0000000000+4.83\ 10^{-30}i$	10^{-64}
0.2	$2.0499475534 - 0.0045930025i$	10^{-3}	$2.0450200861 + .3500363139i$	0.04	$2.0888497837 + .3569822795i$	0.004
0.6	$2.3836324485 - 0.0361782348i$	0.004	$2.3691252941 + .9806955183i$	–	$2.7122160605 + .9492827382i$	0.03
0.98	–	–	–	–	–	–

Table 3: Table of the separation parameter E for some of the modes $n = 0, 4, 7$ and for some chosen values of the rotational parameter in the case $l = 1$. Presented is also $\delta(E^\varepsilon)$, the maximal difference between the E obtained for the 3 values of $\varepsilon = 0, 0.05, 0.15$ for each a, n, m.

Moreover, one should not forget that the modes are obtained through numerical algorithms with certain numerical zero. In this case, the factors in front of this number (i.e. m) may influence the final results for the frequencies, even though theoretically, one should expect the frequencies in the case $a = 0$ not to depend on m. Another hint for this is that the modes obtained from the radial spectral function for $a = 0$ $\varepsilon = 0, 0.05, 0.15$ coincide with those obtained from the spectral system when $a \to 0$ and that the points for $a = 0$ seem not to deviate from the curves $\omega_{n,m}(a)$.

Another important result concerns which sign of $|\Re(\omega_n)|$ can be obtained using positive or negative ε. The study of two cases ($m = \pm 1$) for $n = 0..19$ shows that while for lower modes $n < N$ one can obtain both signs of $|\Re(\omega_n)|$ for any ε, for higher modes: $\omega_n(\varepsilon) = \text{sgn}(\varepsilon)|\Re(\omega_n)^| + i\Im(\omega_n)$. It turns out that for $n \geq N$, in order to find modes with positive real parts, one should use $\varepsilon > 0$ and vice versa. This result is also confirmed in the case $a \neq 0$. Here N depends on m and ε and for $m = \pm 1$, N=3 or N=5.

From the use of the ε-method for gravitational perturbations ($s = -2$) of non-rotating BH, both in the RWE and in the TRE ($a = 0$), it is known that deviations from the results obtained with the continued fraction method occur are due to the branch cuts in the numerical realization of the confluent Heun function. The results of a similar study of $\omega_n(\varepsilon)$ for the electromagnetic QNMs, for $a = 0$, can be found on Fig.17. The numerical data show that the change in ω_n due to the variation of ε occurs in the 11^{th} digit of the real and imaginary parts of ω_n, thus it is a very small effect. This effect, however, is two orders of magnitude above the numerical error for the confluent Heun function expected to have at least 13 stable digits. The dependence $\omega_{n,m}(\varepsilon)$ looks chaotic, but some kind of periodic behavior may be suspected. If one approximates $\omega_{n,m}(\varepsilon)$ with a periodic function, its amplitude decreases with the increase of n (see Fig.17 a), where the results for $n = 0..5$ are plotted). This seems to imply that the observed numerically effect becomes less pronounced for the higher modes, even though one can expect an increase of the error of the numerical integration in the complex plane with n. This line of reasoning, however, applies only to the intervals where the dependence $\omega_n(\varepsilon)$ is smooth (see the discussion on page 12).

Additional details on $\omega_{n,m}(\varepsilon)$ for $n = 7$ can be seen on Fig. 17 b). The observed behavior is not isolated, but it repeats in all modes and all m and also when one includes rotation (i.e. $a > 0$).

.1.3 The behavior of the modes for different ε for $a > 0$

Studying the modes $n = 0..10$ in the case of different $\{l, m, n\}$ and different values of ε one obtains the following results:

- The case $m = 0, l = 1$. For modes with $n < 4$, the results for the 3 values of ε coincide and they can be seen on Fig. 18. Comparing with the control frequencies, one obtains $\|\omega_{n,0} - \omega^B_{n,0}\| < 10^{-10}, \|E_{n,0} - E^B_{n,0}\| < 10^{-10}$ confirming

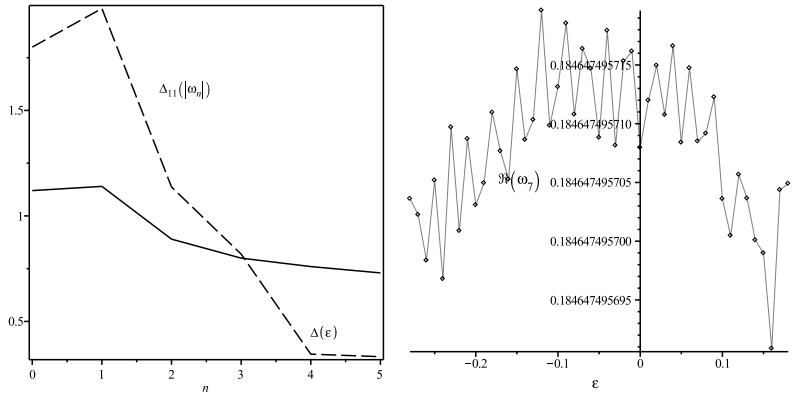

(a) (b)

Figure 17: a) Dashed line: the decrease of the average deviation $\Delta_{11}(\omega_n) = 5 \times 10^{11}|\omega^{\varepsilon}_{0,n} - \omega^{-0.12}_{0,n}|$ with n for $n = 0..5$, $m = 0$. Here, to obtain the average deviation, we have used the average value of $\omega_{0,n}$ in the whole interval for ε subtracted by the value of $\omega_{0,n}$ at $\varepsilon = -0.12$, scaled with the factor of 5×10^{11}. In the intervals of ε considered here $\omega^{\varepsilon}_{0,n}$ has at least 9 stable digits. Solid line: the width of the intervals in question. Both the deviation and the width of the intervals decrease with n.
b) The dependence of $\Re(\omega_{0,n}$ on ε in the interval $\varepsilon = -0.28..0.18$, for $m = 0, n = 7, a = 0$. The average deviation is 10^{-10}

that in this case the two methods – the continued fraction and our method– work comparably well.

For $n \geq 4$, the frequencies obtained for different ε split up in a way that $\omega^0(a) = \omega^{0.05}(a)$, while $\omega^{0.15}(a)$ differs from them (excluded from this "rule" are '$n = 4, 5$ for which $\omega^0(a)$ differs from the other two (Fig. 4.8). The numerical comparison with the control results $\omega^B_{n,m}, E^B_{n,m}$ show that they are closer to the results obtained for $\varepsilon = 0.15$.

Modes with $\Re(\omega_{0,n}) < 0$: as mentioned in the previous section, for modes with $n > 2$ the choice of sign of ε becomes critical for the sign of the real part of the frequency and so we used $\varepsilon = 0, -0.05, -0.15$. [11] The results are symmetrical to those obtained for $\Re(\omega_{0,n}) > 0$ with respect to the imaginary axis for $\omega_{0,n}$ and with respect to the real axis for $E_{0,n}$ (for $\Re(\omega_{0,n}) > 0$, $\Im(E_{0,n}) < 0$ and vice versa).

- The case $m = 0, l = 2$.

  In this case, the modes obtained for $\varepsilon = 0, 0.05, 0.15$ do no split up until $n = 7$, where $\omega^{0.05}(a) = \omega^{0.15}(a)$, while $\omega^0(a)$ differs. This behavior continues until

[11] Using positive ε in this case shows that for $n = 3$, the results for $\varepsilon = 0$ and $\varepsilon = 0.05$ split up ($\varepsilon = 0.15$ can not be used at all), but it is for $n = 6$ where $\varepsilon = 0.05$ can no longer be used for finding frequencies with negative real parts and only $\varepsilon = 0$ lead to the desired modes.

$n = 12$, where it is $\omega^{0.15}(a)$ that deviates from the other two. The results for $l = 2$ can be seen on Fig. 4.11.

- The case $m = 1, l = 1$.

  The modes obtained for the three values of ε coincide up to $n < 4$. For $n = 4$ (Fig. 19), the mode with $\varepsilon = 0$ differs. For $n = 6$, however, it is $\varepsilon = 0.15$ that differs, while the other two coincide and this behavior continues for higher modes. Note, here the deviation for different ε is much more significant than the case $m = 0$ (Fig. 4.8).

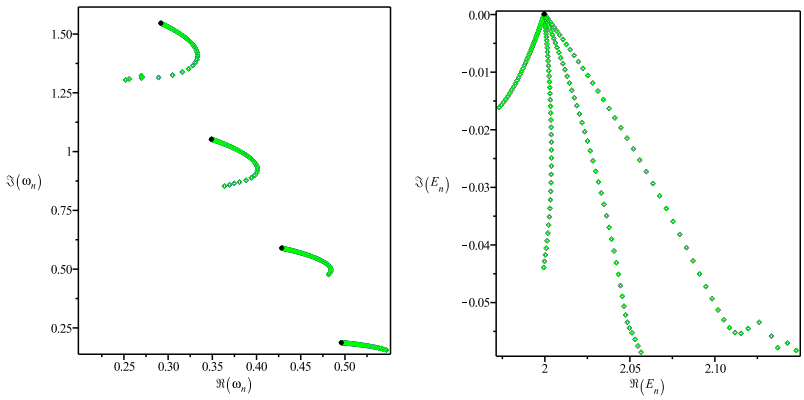

Figure 18: Complex plots of $\omega_{0,n}(a)$ and $E_{0,n}(a)$ in $a = [0, M)$, $l = 1$ for the first 4 modes $n = 0..3$. The points obtained for $\varepsilon = 0, 0.05, 0.15$ coincide with more than 10 digits thus only $\varepsilon = 0$ is plotted. The black solid circle denotes $a = 0$

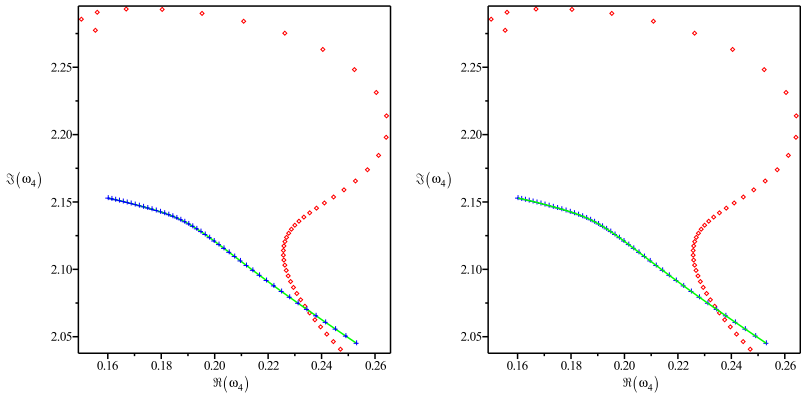

Figure 19: Complex plots of $\omega_{1,4}(a)$ and $E_{1,4}(a)$ in $a = [0, M)$, $l = 1$, for $\varepsilon = 0$ (red diamonds), $\varepsilon = 0.05$(blue crosses) and $\varepsilon = 0.15$ (green line). There is dramatical difference in the points obtained for the different values of ε

These results show that the peculiarities observed when there is no rotation are inherited by the modes for $a > 0$. Studying the dependence of $\omega_{m,n}(\varepsilon)$ for each mode

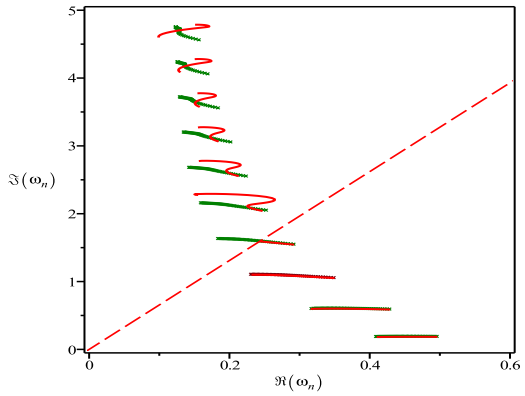

Figure 20: Complex plot of the modes $\omega_{1,n}(a)$ in $a = [0, M)$ for $m = 1, l = 1, n = 0..9$. On the plot are the points obtained for two values of ε: $\varepsilon = 0$ with red lines and $\varepsilon = 0.15$ with green crosses. The red dashed line corresponds to the branch cut with equation $\Im(\omega)/\Re(\omega) \approx \tan(1.419 + \varepsilon\pi/2)$ for $\varepsilon = 0$. One can see that the modes with different ε coincide before reaching the branch cut (i.e. for $n \leq 3$), and then, the $\varepsilon = 0$ points begin to differ

for a certain interval of ε is computationally expensive, so we did it only for the case $n = 10$, $a = 0.01$. The results from the specific interval $\varepsilon = 0.0785..0.088$ can be seen on Fig. 21. Besides the characteristic dependence $\omega(\varepsilon)$, here, for the first time one finds two pairs of points $[\omega_n, E_n]$ as roots for the *same* ε (for $\varepsilon \in [0.07862..0.088034]$), namely:

$$[0.0680207667 + 5.1463791539i, 2.0021361645 + 0.0514150701i],$$
$$[0.1419210235 + 5.0686957246i, 2.0028302584 + 0.0505980908i].$$

Such unexpected result has yet to be explained, considering the big difference between the two frequencies. In any case it points to a behavior which must be studied more carefully in order to better understand the numerical dependence of the EM QNMs with respect to the branch cuts in the radial function.

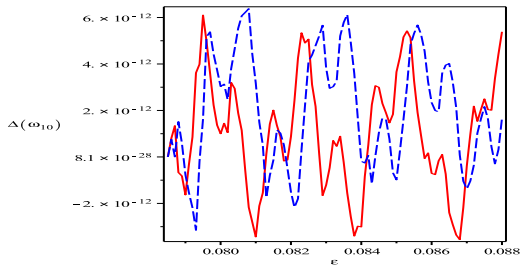

Figure 21: The dependence of $\Delta(\omega_{1,10})$ on ε for $\varepsilon = 0.0785..0.088$, $a = 0.01$. The solid line denotes the real part, the dotted line – the imaginary part and $\Delta(\omega_{1,10})(\varepsilon) = \omega^{\varepsilon}_{1,10} - \omega^{0.0785}_{1,10}$. The dependence $E_{1,10}(\varepsilon)$ is similar

4.3 The Spectrum of Electromagnetic Jets from Kerr Black Holes and Naked Singularities in the Teukolsky Perturbation Theory

In this section we give a theoretical basis for application of the idea of studying the nature of the central engine of GRBs, AGN, etc., based on the spectra of their jets ([35]). Here we examine the jet spectra of the KBH and the KNS supposing that the gravitational field of the central engine is described *exactly* by the Kerr metric.

In series of articles ([125], [126],[97]), we presented a very simple model inspired by the properties of GRBs, that aims to show the strength of purely gravitational effects in the formation of jets. Our toy model is based on linearized electromagnetic (spin-one) perturbations of the Kerr black holes with original boundary conditions. While we keep the BHBC imposed on TRE, we drop the regularity condition on TAE choosing to work with specific *singular* solutions of TAE instead. To achieve this, we impose a polynomial condition on the solutions of TAE. This new angular condition reflects a change in the physical problem at hand which now describes a jet (angular singularity) on one of the poles of the black hole. It is easy to impose the polynomial condition using the properties of the confluent Heun functions, which enter in the exact analytical solutions of the Teukolsky equations (for more on the use of confluent Heun functions in Teukolsky equation see: [35], [66] and [67]). Here, we focus on the $\mid s \mid = 1$ case (electromagnetic perturbations) which seems to be most relevant for the GRB theory.

We study in detail the *complex* spectra of frequencies and their dependence over the rotational parameter of the Kerr metric, a. The parameter a in our calculations varies from $a = 0$ to $a = M$ and then from $a = M$ to $a >> M$. The case $a \in (0, 1)$ corresponds to *normally spinning* Kerr spacetime, and the case $a \in (1, \infty)$ – to *overspinning* Kerr spacetime.

Much like in flat spacetime, we can consider given physical problems in Kerr spacetime with different M and a. Imposing BHBC for $0 < a < M$ we obtain the well studied case of KBH. Under proper boundary conditions which have to be specified for $a \in (M, \infty)$ we obtain different physical problem related with Kerr naked singularity (KNS). The case $a = M$ under BHBC corresponds to extremal KBH. This case is beyond the scope of the present work.

In our numerical study of jet spectra, there is a special frequency ($n = 0$), which has a real part that coincides with the critical frequency of superradiance in the QNM case. In our case, this frequency, however, is complex, and its imaginary part is of the same order of amplitude as the real part, yielding an exponential damping of the superradiance-like emission in jets, created by KBH or KNS. We track the nontrivial change of this critical superradiance-like frequency with the change of a. It is shown that the analytical formula (4.18) (found in [67]) fits the numerical results for the two lowest modes, $n = 0, m = 0, \pm 1, \pm 2, N = 0, 1$ with high precision in the whole range of a.

Our main result is the qualitative change of the behavior of the jet frequencies

under the transition from KBH to KNS. Moreover, we discover for the first time that the stability condition in our jet spectra (positive imaginary part ensuring damping of the perturbations with time) remains fulfilled even in the KNS regime ($a > M$). This happens even though, the imaginary part of those frequencies tends to zero for $a \to M$ – after this critical point, when increasing a, the imaginary part of the frequencies stay positive and grows until it reaches constant value for $a >> M$.

As for the other frequencies, they are possibly an infinite set as in the QNM case. They differ from the QNM frequencies due to the different condition imposed on TAE. The dependence of those frequencies of a is also presented for the first time. The results are being discussed in comparison with the QNM case.

4.3.1 A toy model of central engine

For the solutions of the TAE, we use the new requirement that the confluent Heun functions should be polynomial. The polynomiality condition reads (see (2.8)):

$$\frac{\delta}{\alpha} + \frac{\beta+\gamma}{2} + N + 1 = 0,$$
$$\Delta_{N+1}(\mu) = 0.$$

and it is proven to yield collimated singular solutions ([35]). Here, the integer $N \geq 0$ is the degree of the polynomial and $\Delta_{N+1}(\mu)$ is the three-diagonal determinant (2.9). The degree of the polynomial N depends on the considered class of the solutions of the TAE (recall that one obtain 16 classes of solutions of the TAE, [67]) and in general, it depends on s and m. In our case, $N = 0, 1$ with $N = 0$ obtained for some of the solutions for $m = 0$. Then from $\Delta_{N+1} = 0$ it follows that the power series would be cut after its $N + 1$th term i.e after the first or the second term.

Therefore, from the properties of TAE, the polynomial requirement for the angular solutions fixes the following relation between E and ω:

$$_{s=-1}E_m^{\pm}(\omega) = -(a\omega)^2 - 2\,a\omega\,m \pm 2\sqrt{(a\omega)^2 + a\omega\,m}. \tag{4.6}$$

This simple *exact* relation demonstrates the technical advantage of the polynomial requirement – instead of working with a complicated connected system of spectral equations (as in the QNM case), we have to solve only one spectral equation for the variable ω. Thus we drastically simplify the calculations and we obtain interesting from physical point of view new results.

Examining this simple form of the relation $E(\omega)$ and using the polynomial solutions, we plotted $S(\theta)$ which controls the angular behavior of the solution and we were able to obtain different type of collimated outflows, generated by electromagnetic perturbations of Kerr metric for arbitrary ω ([125], for example, see fig. (4.22)). In the present work, we are studying numerically the spectrum of ω, defined by KBH and KNS jet conditions.

It is important to emphasis that in the case of the angular equation, we work with the *singular* solutions of the differential equation. The question of the physics

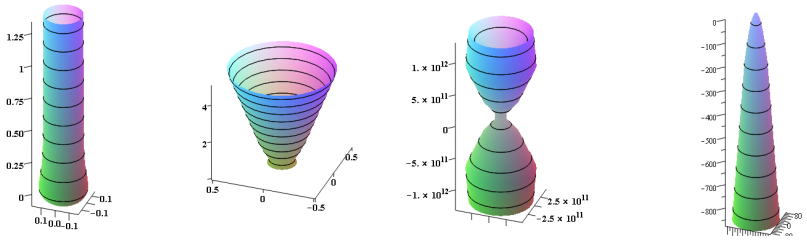

Figure 4.22: Collimated outflows obtained by plotting the solutions of the angular equation for certain values of ω. Here on the horizontal axes are the Cartesian coordinates x and y, on the vertical – the real part of the angular solution

behind the use of such singularity is answered in [67] who argues that by looking for a solution in a specific factorized form $\Psi = e^{i(\omega t+m\phi)}S(\theta)R(r)$, the function we obtain in general isn't the physical quantity ${}_s\Psi(t,r,\theta,\phi)$. Instead it defines a factorized kernel $({}_sK_{E,\omega,m}(t,r,\theta,\phi) \sim e^{i(\omega t+m\phi)}\,{}_sS_{E,\omega,m}(\theta)\,{}_sR_{E,\omega,m}(r))$ of the general integral representation for the physical solutions of the TME:

$$ {}_s\Psi(t,r,\theta,\phi) = \sum_{m=-\infty}^{\infty} \frac{1}{2\pi} \int d\omega \int dE\; {}_sA_{\omega,E,m}\; {}_sK_{E,\omega,m}(t,r,\theta,\phi). \tag{4.7} $$

This form of the mathematical representation of the physical solution is written as the most general superposition of all particular solutions of TME and it assumes summation over all admissible values of E and ω. If one wants to work only with the solutions corresponding to certain boundary conditions, then one has to account for the specific admissible form of the spectra of E and ω in those cases – for example if we have obtained a discrete spectra for ω, this leads to the use of singular kernel proportional to $\sum_n \delta(\omega-\omega_n)$, where δ is the Dirac function. This reduces the integral over ω to a summation over ω_n. Similarly for solutions with definite total angular momentum, we have $E = l(l+1)$ and the integral over E is replaced by summation over l–integer (or half integer), because of singular factor $\sum_l \delta(E - l(l+1))$ in Eq. (4.7).

From Eq. (4.7) it becomes clear that the singular solutions of the angular equation do not cause physical difficulties, only if we are able to find appropriate amplitudes ${}_sA_{\omega,E,m}$ that will make the physical solution ${}_s\Psi(t,r,\theta,\phi)$ regular. It is clear that this formula justifies the use of singular solutions of TAE (for $s = -1$ the singularity is on one of the poles of the sphere, for $s = 1$ – on the another one).

The problem of finding amplitudes turning the singular kernel into a regular physical solution is not a simple one. Here, we will give one example, obtained for the case $s = 1/2$ by Fiziev ([67]), for which such amplitude has been found for the so-called double polynomial solutions (i.e. both the solutions of the TRE and the TAE satisfy the polynomial conditions). While this example proves that in principle it is possible to find such amplitudes, it is important to note that for the double polynomial solutions, the spectra is not discrete but continuous and thus, this is

qualitatively different problem from the one we consider.

The case s=1/2 *For the double polynomial solutions, the degree of the polynomial is* $N = 0$ *and both confluent Heun functions in the solutions of the TAE and the TRE are then equal to constant=1 with separation constant* $E = -a^2\omega^2 + 2a\omega m - 1/4$. *Then the integration over* E *in the kernel* (4.7) *gives:*

$$ {}_{\frac{1}{2}}\mathcal{K}_{\omega,E,m}(t,r,\theta,\varphi) = \delta\left(E + a^2\omega^2 - 2ma\omega + 1/4\right)\Delta^{-\frac{1}{2}} e^{i\omega T}\frac{W^m}{\sqrt{\sin\theta}}, \tag{4.8} $$

with $T = t + (r_* - ia\cos\theta)$, $W = e^{i\phi}\cot\frac{\theta}{2}$, $\phi = \varphi + \frac{1}{2p}\ln\left|\frac{r-r_+}{r-r_-}\right|$. *The new variables come from the factors in the explicit solutions of TRE and TAE for* $s = 1/2$.

Because of the transition from the real variables $\{\theta,\phi\}$ *to the complex* W, *one must make a transition from half-integer to integer values of the azimuthal number* m *and so to replace* $m \to m \pm 1/2$ *in the factor* $\delta\left(E + a^2\omega^2 - 2ma\omega + 1/4\right)$.

Using ${}_{\frac{1}{2}}\mathcal{K}_{\omega,E,m}(t,r,\theta,\varphi)$ *in Eq.* (4.7), *one can integrate:*

$$ {}_{\frac{1}{2}}\Psi(t,r,\theta,\varphi) = \Delta(r)^{-\frac{1}{2}}\sqrt{\left(|W| + |W|^{-1}\right)/2}\sum_{m=-\infty}^{\infty}\left(\frac{1}{2\pi}\int\limits_{\mathcal{L}_\omega} d\omega\; e^{i\omega T}\,{}_{\frac{1}{2}}A_{\omega,m}\right)W^m. \tag{4.9} $$

Accounting for the stability condition $\Im(\omega) > 0$, *the otherwise arbitrary integration contour* $\mathcal{L}_\omega \in \mathbb{C}_\omega$ *must lie in the upper complex half-plane.*

If the amplitudes ${}_{\frac{1}{2}}A_{\omega,m}$ *and the contour* $\mathcal{L}_\omega$ *are chosen in such way that for all* $m \in \mathbb{Z}$ *there exist well defined integrals:*

$$ \frac{1}{2\pi}\int\limits_{\mathcal{L}_\omega} d\omega\; e^{i\omega T}\,{}_{\frac{1}{2}}A_{\omega,m} = {}_{\frac{1}{2}}\mathfrak{A}_m(T), \tag{4.10} $$

then the physical solution will be:

$$ {}_{\frac{1}{2}}\Psi(t,r,\theta,\varphi) = \Delta(r)^{-\frac{1}{2}}\sqrt{\left(|W| + |W|^{-1}\right)/2}\sum_{m=-\infty}^{\infty}{}_{\frac{1}{2}}\mathfrak{A}_m(T)\,W^m. \tag{4.11} $$

In this case, one must ensure that the sum in Eq. (4.11) *is convergent. This can happen, if one requires in some ring domain* $|W| \in (|W|', |W|'')$, $0 < |W|' < |W|'' < \infty$ *that this sum is a convergent Laurent series of some analytic function* ${}_{\frac{1}{2}}\mathfrak{A}(T,W)$. *The convergence criteria will impose certain conditions on the coefficients* ${}_{\frac{1}{2}}\mathfrak{A}_m(T)$ *in Eq.* (4.11).

Then one arrives to the solution to the TME with spin $1/2$ *(to check that it is a solution, one has to return to the Boyer-Lindquist coordinates) depending on an arbitrary analytic function* ${}_{\frac{1}{2}}\mathfrak{A}(T,W)$ *of the two variables* T *and* W*:*

$$ {}_{\frac{1}{2}}\Psi(t,r,\theta,\varphi) = \Delta(r)^{-\frac{1}{2}}\sqrt{\left(|W| + |W|^{-1}\right)/2}\;{}_{\frac{1}{2}}\mathfrak{A}(T,W). \tag{4.12} $$

The explicit form of the variable T shows that for $r > r_+$ these solutions describe one-way-running *waves: incoming from space infinity running waves.*

The singularities on the poles $\theta = 0, \pi$ can be removed by suitable choice of variables. For example: for ${}_{\frac{1}{2}}\mathfrak{A}(T,W) = 1/\sqrt{(W+W^{-1})/2}$, ${}_{\frac{1}{2}}\Psi(t,r,\theta,\varphi) = \Delta(r)^{-\frac{1}{2}}/\sqrt{1-\sin^2\phi\sin^2\theta}$ which don't have any singularities on the poles $\theta = 0, \pi$. However, one obtain two new singular lines $\phi = \varphi + \frac{1}{2p}\ln\left|\frac{r-r_+}{r-r_-}\right| = \pm\pi/2$ on the equatorial plane $\theta = \pi/2$. Therefore, the singularities were just moved to another location. This result repeats also for functions of more general type. In any case, this special form of the function ${}_{\frac{1}{2}}\mathfrak{A}(T,W)$ yields finite nonzero values of the solution on the poles $\theta = 0, \pi$.

Furthermore, in order to secure a correct application of the linear perturbation theory, one must know whether one can find a regular analytical function ${}_{\frac{1}{2}}\mathfrak{A}(T,W)$ without singularities in the complex plane $\mathbb{C}_W/\{0,\infty\}$, which, in addition, can remove the unbounded increase of the solutions due to the singularities of the factor $\sqrt{(|W|+|W|^{-1})/2}$ in (4.12). At least two cases were found, for which the answer is positive. We will consider in detail only one of them:

Using the basic equality $\sum_{m=-\infty}^{\infty} W^m I_m(z) = \exp\left(\frac{1}{2}\left(W+W^{-1}\right)z\right)$ for the modified Bessel functions $I_m(z)$ [132] we choose the coefficients in (4.11) in the specific form ${}_{\frac{1}{2}}\mathfrak{A}_m(T) = \exp\left(-\frac{\bar\sigma}{2}\omega^2T^2\right)I_m(\omega T)$, where $\omega = \omega_R + i\omega_I$ is a fixed frequency and $\bar\sigma = sign(|\omega_R| - |\omega_I|)$. Then

$$ {}_{\frac{1}{2}}\Psi_\omega(t,r,\theta,\varphi) = \Delta(r)^{-\frac{1}{2}}\sqrt{(|W|+|W|^{-1})/2}\ \exp\left(-\frac{\bar\sigma}{2}\omega^2T^2\right)\exp\left(\frac{1}{2}\left(W+W^{-1}\right)\omega T\right) \tag{4.13} $$

is a stable solution, since by construction it goes to zero when $t \to +\infty$. Its limit for $\theta \to 0, \pi$ is:

$$ \lim_{\theta\to 0,\pi}\left({}_{\frac{1}{2}}\Psi_\omega(t,r,\theta,\varphi)\right) = \Delta(r)^{-\frac{1}{2}}e^{\left(-\frac{\bar\sigma}{2}\omega^2T_{0,\pi}^2\right)}\lim_{\theta\to 0,\pi}\left(\frac{1}{\sqrt{\sin\theta}}e^{\left(\frac{|\omega|\sqrt{(t+r_*)^2+a^2}}{\sin\theta}e^{i\Upsilon_{\omega;0,\pi}}\right)}\right). \tag{4.14} $$

where

$$ \Upsilon_{\omega;0,\pi} = \pm\left(\varphi + \frac{1}{2p}\ln\left|\frac{r-r_+}{r-r_-}\right| - \arctan\left(\frac{a}{t+r_*}\right)\right) + \arg(\omega),\ \ for\ \theta = 0,\ or\ \pi \tag{4.15} $$

is the limit of the total phase of the term $\frac{1}{2}\left(W+W^{-1}\right)\omega T$ and $T_{0,\pi} = t + (r_* \mp ia)$. In Eq. (4.15) the sign $(+)$ corresponds to the limit $\theta \to 0$ and the sign $(-)$ – to $\theta \to \pi$. From (4.14) one can see that if $\Upsilon_{\omega;0,\pi} \in \left(-\frac{\pi}{2}, \frac{\pi}{2}\right)$ the solution ${}_{\frac{1}{2}}\Psi_\omega(t,r,\theta,\varphi)$ is bounded everywhere in the interval $\theta \in [0,\pi]$, (since in this case $\lim_{\theta\to 0,\pi}\left({}_{\frac{1}{2}}\Psi_\omega(t,r,\theta,\varphi)\right) = 0$), while otherwise the limit diverges and the solution is singular and unbounded around the poles.

Since the value of the angle φ is arbitrary on the poles $\theta = 0, \pi$, $\Upsilon_{\omega;0,\pi}$ is not defined from a geometrical point of view and one can choose any value for it without changing the geometrical points associated with the poles. In our case, fixing the parameter $\Upsilon_{\omega;0,\pi} \in \left(-\frac{\pi}{2}, \frac{\pi}{2}\right)$ makes the solutions (4.14) to the TME for spin $1/2$ smooth and bounded everywhere in the interval $\theta \in [0, \pi]$ – it is physically acceptable.

For another solution, finite *everywhere in the interval $\theta \in [0, \pi]$, but with an infinite number of bounded oscillations around the poles $\theta = 0, \pi$, see [67]. A superpositions of those two solutions can describe a more general bounded solutions to the TAE with spin $1/2$.*

Knowing $E(\omega)$, we can find numerically the frequencies ω by imposing boundary condition on the radial equation. The Kerr spacetime can be considered as a background for different physical problems. As in flat spacetimes, one has to fix the physics imposing the corresponding boundary conditions. A specific peculiarity of Kerr spacetime is that in general TRE has 3 different singular points (Eq. (3.28)) – r_+, r_- and ∞. To fix the correct physical problem we have to specify the boundary conditions on two of them (the asymptotic behavior of the solution in these points). This represents the so-called *central two-point connection problem* (as described in [105]). In principle, we can impose boundary conditions on different pairs of singular points (on r_- and r_+; on r_- and $\pm\infty$; on r_+ and $\pm\infty$; on $-\infty$ and $+\infty$) and each of them will fix different type of physical situation.

Note that choosing a specific central two-point connection problem we are fixing the physical problem independently of the bifurcation parameter b. This way, we are able to study the bifurcation phenomenon in the given physical problem in the whole range of b. Since we want to study jets from KBH and KNS, we start with imposing BHBC on r_+ and ∞ for the first case ($a < M$), where the regular singularities are *real*. These boundary conditions are physically well motivated ([51], [43]) and the central two-point connection problem for KBH has a clear physical meaning. The same central two-point connection problem exists in the overspinning case, nevertheless that its two regular singularities $r_\pm$ are *complex*. We use the same boundary conditions for the case of jets from KNS, since the physics of the problem is defined by its them. Thus we transform the BHBC to a naked singularity boundary conditions using analytical continuation of the central two-point connection problem.

BHBC can be summarized to:

1. On the horizon ($r \to r_+$), we require only ingoing (in the horizon) waves. This specifies which one of the two solutions of TRE (R_1 or R_2) works in each interval for the frequency ω. In our case for any integer m, R_1 is valid for $Re(\omega) \in (\mp m\omega_{cr}, 0)$, R_2 is valid in $Re(\omega) \in (\mp\infty, \mp m\omega_{cr}) \bigcup (0, \pm\infty)$ where $\omega_{cr} = a/2Mr_+$ and the first sign corresponds to $m > 0$.

2. On infinity ($r \to \infty$) we allow only outgoing waves. Explicitly, on infinity we have a linear combination of an ingoing ($R_\leftarrow$) and an outgoing ($R_\rightarrow$) wave:

$$R = C_\leftarrow R_\leftarrow + C_\rightarrow R_\rightarrow$$

where $C_\leftarrow$, $C_\rightarrow$ are unknown constants. In order to have only outgoing waves, we

need to have $C_{\leftarrow} = 0$. Since this constant is unknown, we find it indirectly from:

$$C_{\leftarrow} = \frac{R}{R_{\leftarrow}} - C_{\rightarrow}\frac{R_{\rightarrow}}{R_{\leftarrow}}. \tag{4.16}$$

If in this equation we set $\lim_{r\to\infty} \frac{R_{\rightarrow}}{R_{\leftarrow}} = 0$, this will eliminate the second term in Eq. (4.16). To do this, we complexify r and ω and choose the direction in the complex plane $\mathbb{C}_r$ in which this limit tends to zero most quickly. This direction turns out to be $arg(r) = 3\pi/2 - arg(\omega)$ i.e $r =\mid r \mid e^{3/2i\pi - i\,arg(\omega)}$ connecting the arguments of the complexified r and ω ([39]). Having fixed that, it is enough to solve

$$C_{\leftarrow} = \lim_{|r|\to\infty} \frac{R}{R_{\leftarrow}} = 0. \tag{4.17}$$

in order to completely specify the spectra ${}_s\omega^{jet}_{n,m}$. For KNS we use the same boundary conditions in the complex domain (see above).

Since in this paper we calculate only the case $s = -1$, for jets from KBH and KNS, we will omit the prefix $s = -1$ in front of $\omega_{n,m}$ and also the index "jet".

4.3.2 Numerical results

In [125] and [126], we presented some preliminary results for the solutions of TAE. They showed that the polynomial angular solution describes collimated structures from various types for some arbitrary ω. In this work we will focus on the solutions of the radial equations, thus fixing the spectrum $\omega_{n,m}$ for jets from KBH and KNS.

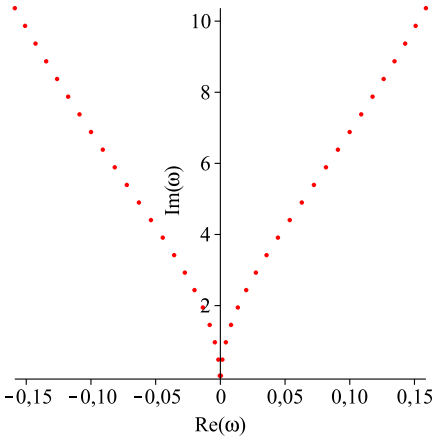

Figure 4.23: Complex plot of the frequencies ω_n for $a = 0$, with $n = 0, 1...$ increasing with the distance to the origin. For every n there are 2 roots with equal $\mid Re(\omega) \mid$.

4.3.2.1 Numerical methods

To find the zeros of Eq. (4.17), we use the software package MAPLE which currently is the only one able to work with Heun's functions.

The roots presented here are found with modified by the team Müller algorithm, with precision 13 digits. Although the results for different versions of MAPLE may vary in some cases due to improvements in the numerical algorithm, key values were checked to match with at least 6 digits, in most cases – with more than 8 digits.

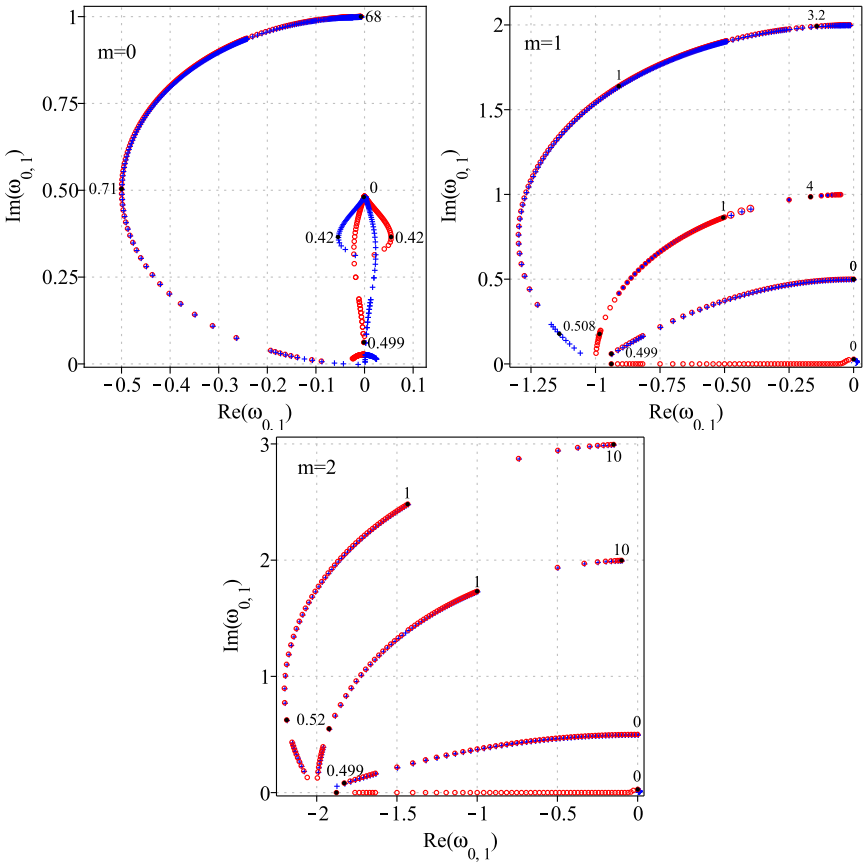

Figure 4.24: Complex plot of $\omega^{\pm}_{0,m}(a)$, $n = 0$ mode, for $m=0, 1, 2$. With red is $\omega^{+}_{0,m}$, with blue crosses: $\omega^{-}_{0,m}$, on the curve we mark some values of a. It's clear that for $m>0$, $\omega^{+}_{0,m}$ and $\omega^{-}_{0,m}$ coincide almost everywhere. For $m \neq 0$ and $a > 0$, only one of the frequencies in each pair $\omega_{1,m}(a = 0)$ continues to be a root.

The parameters are fixed as follows : $s = -1$, $M = 1/2$, $r = 110$. This value for the radial variable r is chosen so that it represents the actual numerical infinity –the closest point at which the frequencies found by our numerical method stop changing significantly for further increase of r (for fixed a, m, n). In study of the dependence on a, the step for the rotational parameter is $\delta a = 0.01$ for $a < M$ and becomes adaptive for $a > M$.

In our work, we have studied in detail cases with $m = 0$, $m = \pm 1, 2$, covering the cases $\mid m \mid < \mid s \mid$, $\mid m \mid = \mid s \mid$, $\mid m \mid > \mid s \mid$. The complete set of our numerical results are available on request.

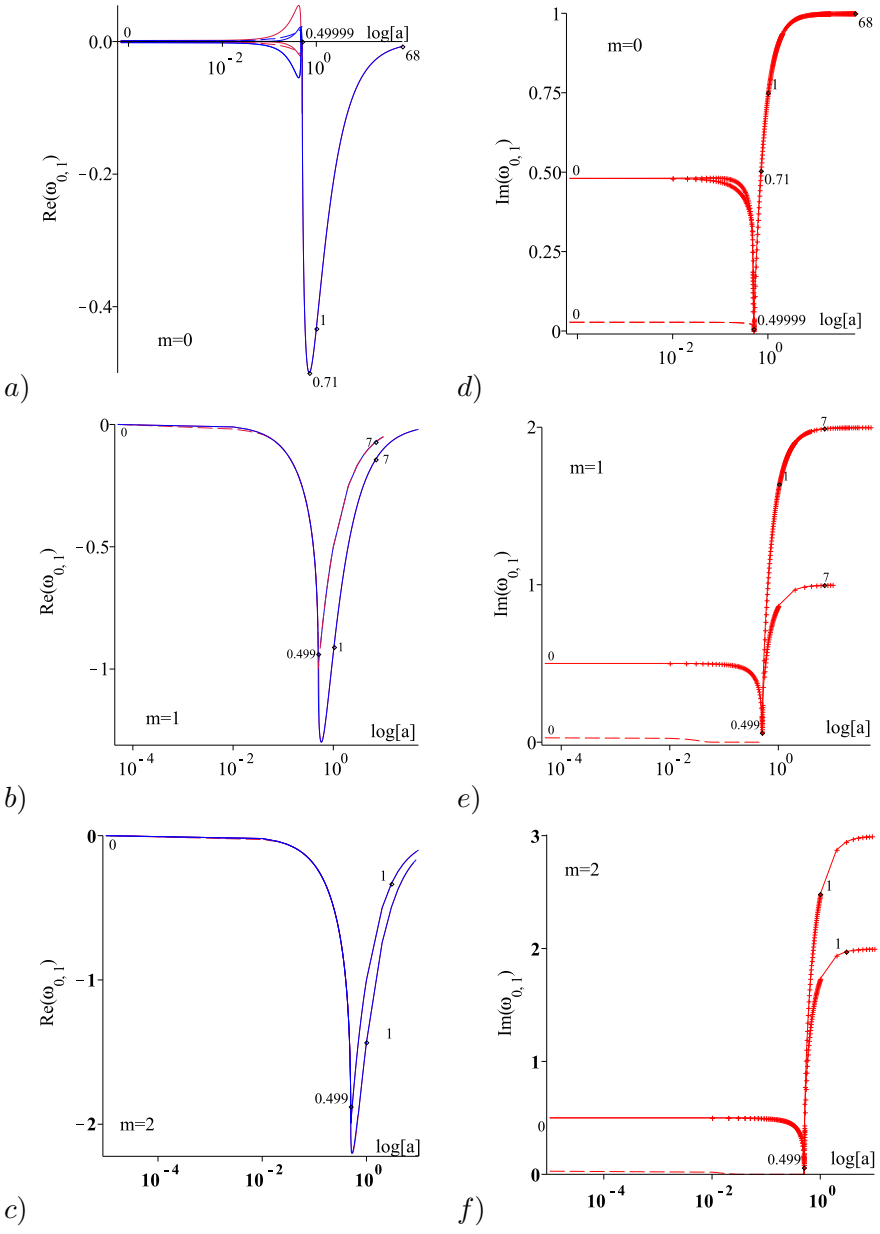

Figure 4.25: The dependence $Re(\omega)(a)$ and $Im(\omega)(a)$ for $m = 0, 1, 2; n = 0$. One can see that $Im(\omega) \to 0$ for the bifurcation point $b = 1$ ($a = M = 0.5$) implying a critical event in this point. $Re(\omega) \equiv \omega_{cr}$ for $a < M$ for this mode.

4.3.2.2 Summary of the results

Graphical representation of our results can be seen on the figures 2-11. For the case $a = 0$ when no rotation is present, we find a set of pairs of frequencies with equal imaginary parts and symmetrical in respect to the imaginary axis real parts. This set (Fig. 4.23), looks infinite and it is independent from m (for $a = 0$) as it should be. Frequencies are numbered with n according to their distance from the origin $\mid \omega_n \mid$, starting with $n = 0$ for the lowest.

Although Fig. 4.23 shows the case without rotation, it drastically differs from the results obtained by solving the Regge-Wheeler Equation for the Schwarzschild metric in the QNM case ([39], [133] or see figure 4.6 in the next section), because of the change of the conditions for the solutions of TAE.

Using the so found initial frequencies, we track their evolution with the change of the rotational parameter a, following both pairs of frequencies for each n and both signs in front of the square root in $E(\omega) = -(a\omega)^2 - 2\,a\omega\,m \pm 2\sqrt{(a\omega)^2 + a\omega\,m}$, which we denote $\omega^+_{n,m}$ and $\omega^-_{n,m}$ accordingly. On the figures, the number of points we present is limited by the abilities of the MAPLE numerical procedures evaluating the confluent Heun function.

The relation $\omega_{n,m}(a)$ is nontrivial as can easily be seen on Fig. 4.24 and Fig. 4.25.

The results we obtained can be summarized as follows:

- The cases $n = 0, 1$ are special, because for them $Re(\omega^+_{0,m}) \sim Re(\omega^\pm_{1,m})$ (for $m > 0$) while $Im(\omega^+_{0,m}) << Re(\omega^\pm_{1,m})$ (for $a = 0$, $Im(\omega^+_{0,m}) \approx 0.024459i$ and it decreases quickly to less than $10^{-7}i$ for $a > 0$ and $m = 1, 2$; in the case $m = 0$ it decreases more slowly). Since the real parts of the two pairs are close for $a < M$, and the imaginary part of the one is negligible, in our figures in that range, we use only the complex frequencies $\omega^\pm_{1,m}$) . This can be done without loss of information, because for $a > 0.1$, $Im(\omega'^{1,2}_{0,m}) < 10^{-10}$ (for $m \neq 0$ and $a < M$), which is less than the precision of our algorithm. $\omega^-_{0,m}$ (for $m > 0$) however is different from $\omega^+_{0,m}$ and have very small real and imaginary parts and since our numerical precision for it is low, we would not discuss it. The situation reverses for $m < 0$ when $Re(\omega^-_{0,m}) \sim Re(\omega^\pm_{1,m})$.

- For $m > 0$, the real part of $\omega_{1,m}$ decreases steadily with the increase of a, having minimums at the points $a = M$ and $a \geq M$, but close to it – see Fig. 4.25 c), e). In the case $m = 0$, $Re(\omega_{1,0})$ has a maximum for $a < M$ and then has a minimum for $a > M$ (Fig. 4.25 a)).

- The imaginary part of $\omega_{1,m}$ (Fig. 4.25 b), d), f)) for all the cases is positive, it decreases for $a < M$ and it tends to zero for $a = M$. For $a = M$, the solutions of TRE can no longer be expressed in terms of confluent Heun functions. In this case one has to use double confluent Heun function ([67]). We didn't calculate at this point. When $a > M$, $Im(\omega_{n,m})$ increases again until it reaches almost constant value at high a.

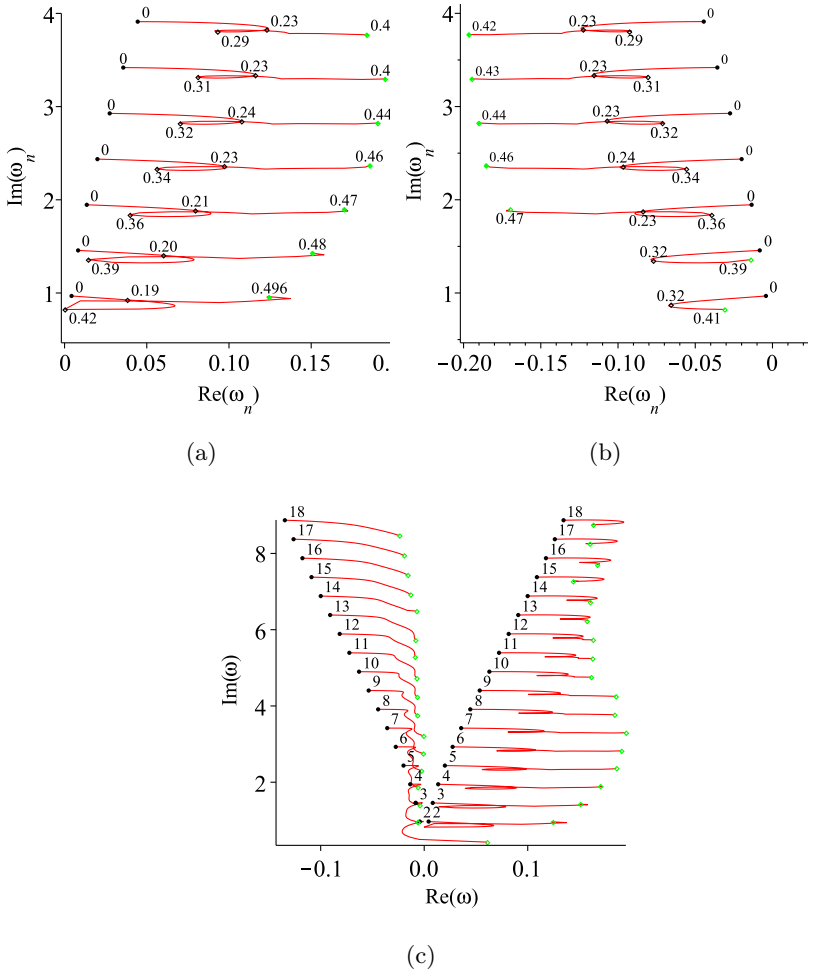

Figure 4.26: Complex plot of some of the frequencies with different n ($n = 1-7$) we obtained in the case $m = 0$, a) $\omega^{+}_{n,0}$, b)$\omega^{-}_{n,0}$. It's clear that for $m = 0$, the symmetry observed for $n = 1$, continues in the higher modes. c) $\omega^{+}_{n,0}$ for $n = 1-17$ (the black dot stays for $a = 0$, green diamond – the last a where a root was found). The $n = 0$ mode isn't plotted.

- At $a > M$, $m \neq 1$ we obtain two modes, with different values of the real and imaginary parts. The real part of the first mode has a minimum at $a = M$, while the real part of the other has a minimum "later": at $a > M$. The imaginary part of both modes tends to zero for $a \to M$, but for $a >> M$, they reach to constant with $Im(\omega_{0,m}) - Im(\omega_{1,m}) \approx 1$. These two modes appear for $m = \pm 1, \pm 2, \pm 3$ (Fig. 4.24 and Fig. 4.25). We couldn't find other modes for $a > M$ using our numerical methods.

- Modes with $n > 1$ demonstrate highly nontrivial behavior and strong dependence of the parameter a, even though numerically, they cannot be traced to $a > M$ and in some cases we are able to fix very limited number of points.

  For $m = 0$, those modes persistently demonstrate signs of loops (see Fig. 4.26 and Fig.4.28), which seem to disappear for $m \neq 0$(Fig. 4.30, Fig. 4.31).

  The real parts of the modes with $n > 1$ seem to form a surface whose physical meaning is yet unknown, while their imaginary parts are splitting in two with increasing of the rotation (Fig.4.29, Fig.4.31).

- The frequencies $\omega^{+}_{n,m}$ and $\omega^{-}_{n,m}$ are symmetric for the case $m = 0$ (Fig. 4.27), any n and they coincide for the cases $m \neq 0$, $n = 1$ for $a \geq a_m$, where a_m tends to zero for sufficiently big m (for $m = 1$, $a_m = 0.1$, for $m = 2$, $a_m = 0.04$, for $m = 5$, $a_m = 0.02$, for $m = 10$, $a_m = 0$). For $n > 1$, $\omega^{+}_{n,m}$ and $\omega^{-}_{n,m}$ do not coincide.

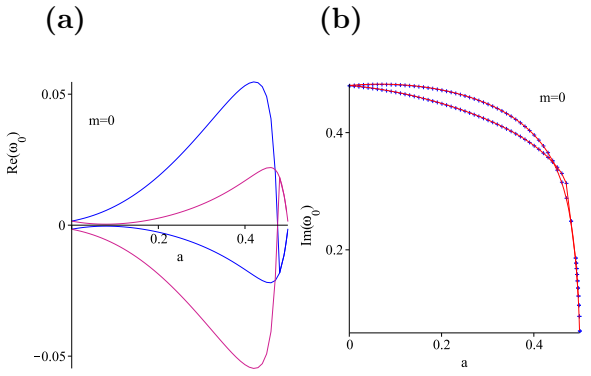

Figure 4.27: A particular case of the symmetry observed in the frequencies, for $n = 0$, $m = 0$, $a < M$, for $\omega^{\pm}_{n,m}$. For $m \neq 0$ $\omega^{+}_{n,m}$ and $\omega^{-}_{n,m}$ coincide for $a > a_m$.

- There is a symmetry in our spectra, which is confirmed for $m = \pm 0, 1, 2$ for all of the modes (except for some points):

$$Re(\omega^{1,2}_{m,n}) = -Re(\omega^{2,1}_{-m,n}),\ Im(\omega^{1,2}_{m,n}) = Im(\omega^{2,1}_{-m,n}),$$

  where here the index $1, 2$ numbers the frequency from the pair corresponding to each m, n (frequencies with positive and negative real part for each m, n on Fig. 4.23).

This symmetry allows us to study for example only the case $m > 0$ if or when it works numerically better.

From the figures, one can clearly see that the relation $\omega_{1,m}(a)$ demonstrates systematic for every m behavior characterized by some form of critical event at the bifurcation point $a = M$, where the damping of the perturbation ($Im(\omega_{n,m})$) tends to zero. Physically, this transition corresponds to the change of the topology of the ergo-surface visualized on Fig. 3.1.

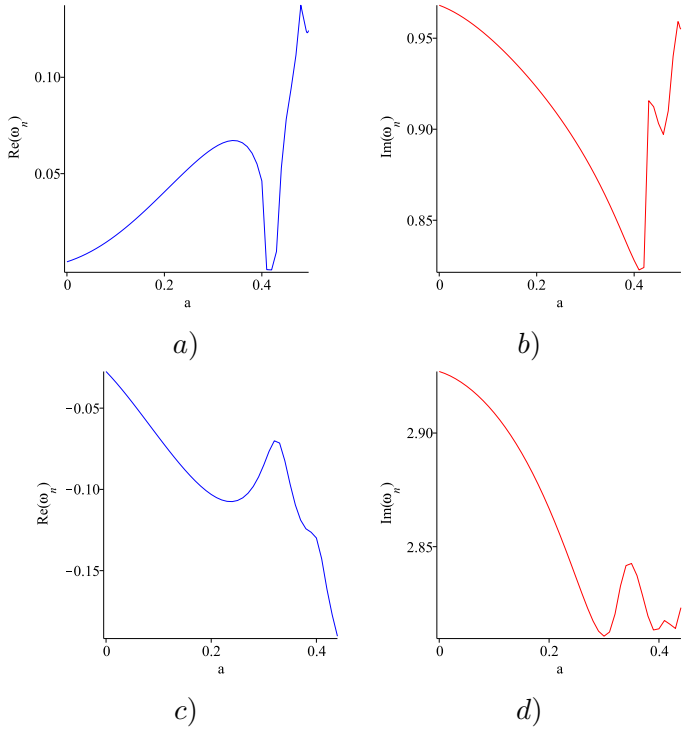

Figure 4.28: 2 cases showing the detailed behavior of modes with $n > 1$ for $m = 0$. a),b) correspond to $n = 1$ and c),d) to $n = 5$, for $\omega^{-}_{n,0}$

4.3.2.3 Analysis of the results

The spectra we presented demonstrates a clear transition at the bifurcation point $a = M$, matching the transition from a rotating black hole to an extremal black hole demanded by the theory of black holes. Since we can approach the point $a = M$ from both directions, it seems natural to speak also of extremal naked singularity, for $a \to M$, but $a > M$. From our figures it is clear that the behavior of the spectra when $a \to M$ from both sides is similar – the imaginary part of the critical frequency tends to zero at that points, and quickly rises to a (different) constant for $a \neq M$. We couldn't find any frequencies with negative imaginary parts in this case, thus it seems that the jets from KBH and KNS are stable even in the regime

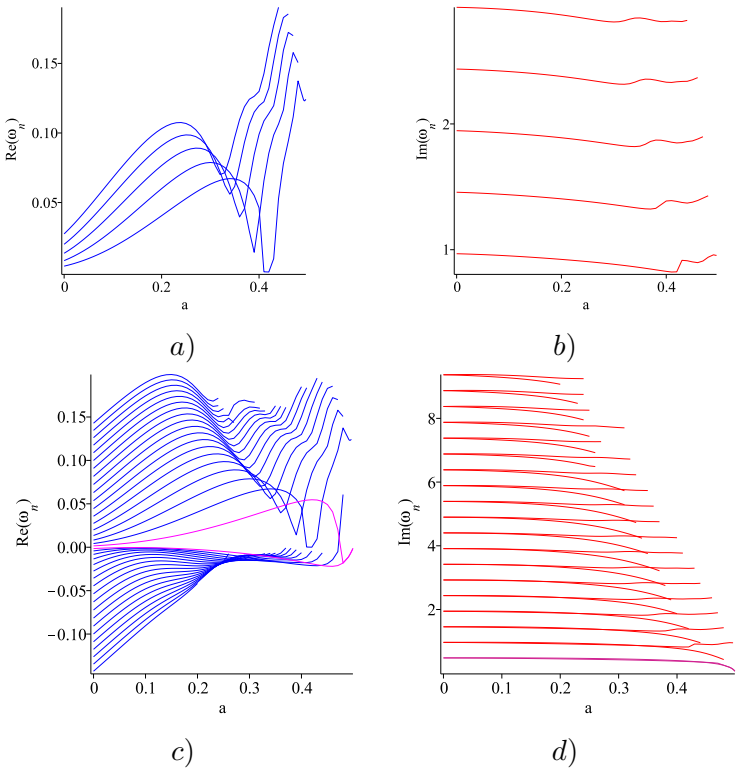

Figure 4.29: a), b) - $Re(\omega)$ and $Im(\omega)$ with $n = 1..5$, $m = 0$, $\omega^{+}_{n,0}$ c),d): $Re(\omega)$ and $Im(\omega)$ with $n = 0..18$ for $m = 0$. In c) and d) we plotted the two conjugate roots on one plot. The violet lines correspond to the $n = 0$ mode.

of naked singularities. This differs from the QNM case, in which QNM from naked singularities are unstable.

Another example of unstable spectra is the one in [134] where a completely different boundary conditions for overspinning Kerr space-time are considered. There, the authors have analyzed central two-point connection problem on the singular interval $r \in (-\infty, \infty)$. As we see, the jets in our case are stable and there is no contradiction since we study a completely different physical problem. Not only for our jets the stability condition remains fulfilled, but the discrete level of the spectra of the jets from KBH and KNS appear to be smooth in the whole interval (except for the bifurcation point $a = M$) thus implying that jets from naked singularities defined by the polynomial condition of TAE generate numerically of a spectra of stable perturbation.

Another surprise is that $Re(\omega_{0,m}) \equiv m\omega_{cr}$ for $a < M$ for both cases in $n = 0$, where ω_{cr} is the critical frequency of superradiance. Supperradiance is a process in which the energy of the reflected from the horizon wave is bigger than the energy of the in-falling wave and it leads to extraction of energy from the black hole at expense of its rotational energy. For the QNM case, superradiance occurs when

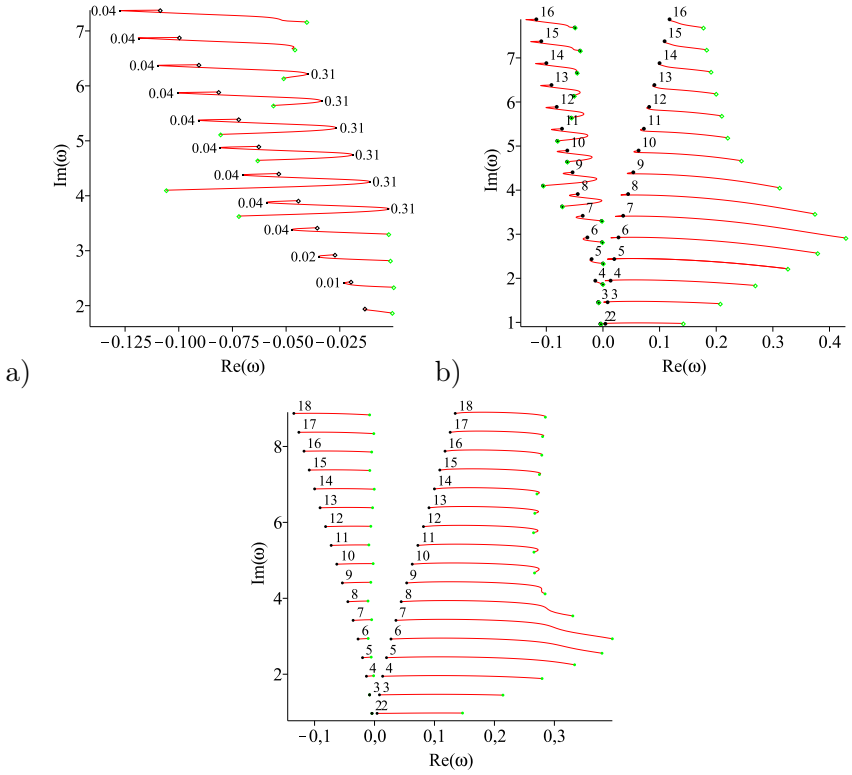

Figure 4.30: a) Complex plot of all of the frequencies with $n > 1$ for $m = -1$ a) more detailed plot of the first few modes ($n = 3 - 14$) for $\omega^{+}_{0,m}$ – there are no loops for $\mid m \mid = 1$, b) a plot of frequencies $n = 1 - 17$ for $\omega^{+}_{n,-1}$, c) frequencies $n = 1 - 17$ for $\omega^{-}_{n,-1}$.

$\omega < m\omega_{cr} = ma/2Mr_{+}$ (for real frequencies ω_{cr}!) and it leads to the interesting phenomena that although in local frame, the wave is ingoing to the horizon, at infinity it is actually seen as outgoing (following from the signs of the group and phase velocities) (see [42], and also [20], [135], [136], [137], [138], [24]).

In our case, we observe two frequencies whose real parts coincide with the critical frequency of superradiance, however, only one of them is real, the other also has an imaginary part with similar magnitude. To the best of our knowledge this is the first time that an imaginary part of this quantity is discovered solving BH boundary conditions in pure vacuum (i.e. without any mirrors, additional fields, etc).

Another hint of the importance of the obtained in QNM studies critical frequency is that in our results, it represents the two lowest modes in our spectra and the only ones, which we can trace to $a > M$. Although this certainly can be due to the numerical routines we use, its persistence for every m speaks of possible deeper physical meaning.

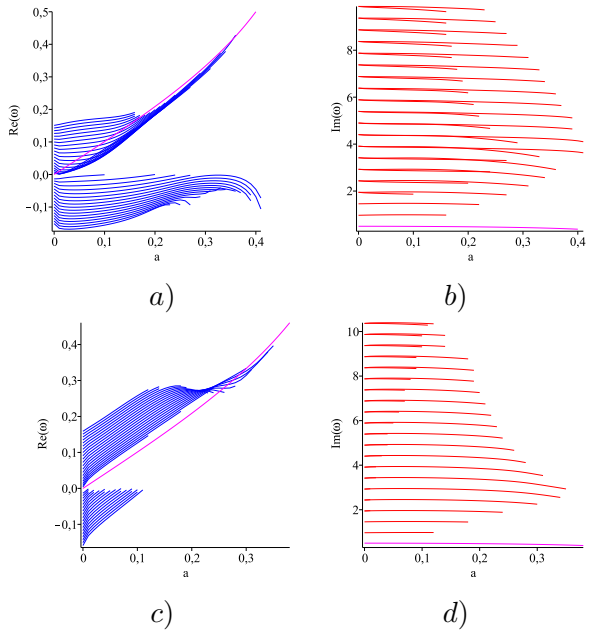

Figure 4.31: $Re(\omega)$ and $Im(\omega)$ for modes with $n > 1$, $m = -1$: a) and b) are the real and imaginary parts of $\omega^{+}_{n,-1}$, c) and d) are the real and imaginary part of $\omega^{-}_{n,-1}$. There is a clear asymmetry between the cases.

The complexity of the critical frequency shows an essential difference between our jets-from-KBH and KNS solutions and standard QNM, obtained using regular solutions of the angular equation (Eq. (3.27)) ([51]). The fact that in general the real and imaginary parts of $\omega^{jets}_{n,m}$ are with the same magnitude (which can be easily verified on all of our complex plots) means that the perturbations will damp with time on the same time scale on which they oscillate (or shorter for the bigger $Im(\omega)$, following from $\Psi \sim e^{-Im(\omega)t}e^{iRe(\omega)t}$), thus preventing in most cases such systems from turning into a gravitational bomb (a system of KBH or KNS and mirrors in which the wave will reflect from the horizon becoming more and more energetic until the whole system becomes unstable and explodes [63]; in nature, a role of such "mirror" may be played for example a massive scalar field [139]). Although the perturbation in general damps quickly for $a \neq M$, this situation changes at the limit $a \to M$ – the imaginary part of ω then tends to zero, both for $a < M$ and $a > M$ near the bifurcation point $a = M$. At this case the perturbation will damp very slowly with time while oscillating violently, opening the possibility for interesting physical phenomena which deserve an additional detailed consideration.

The best fit for our numerical data for the lowest modes ($n = 0$) turns out to be formula (3.4a) in [67]:

$$\omega_{0,m} = (-m + 4iN\sqrt{M^2/a^2 - 1}\,)\,\omega_{cr}, N = 0, 1 \tag{4.18}$$

Here, the formula is written in terms of ω^{QNM}_{cr} since it is more relevant to the

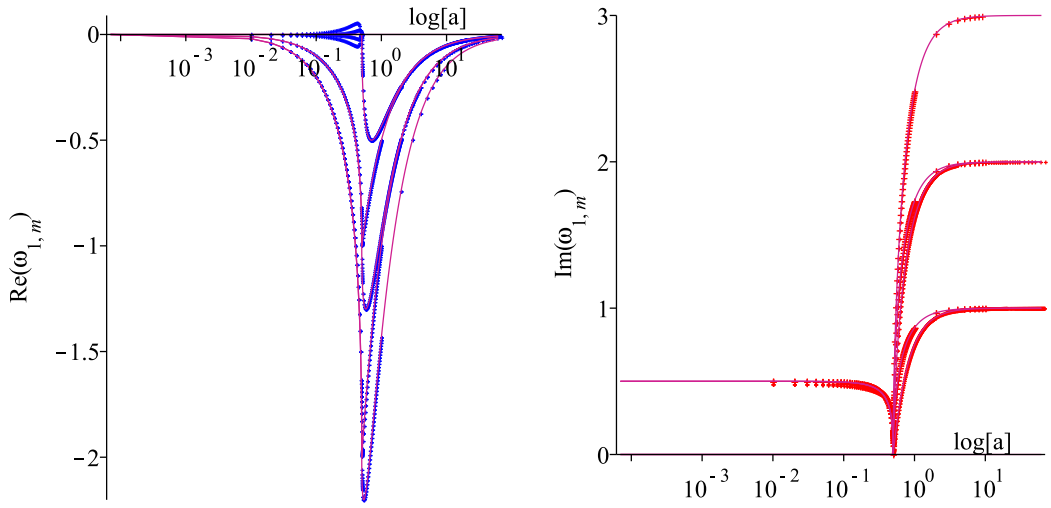

Figure 4.32: Comparison between our numerical results plotted with blue (red) circles and the analytical formula (magenta lines). The excellent fit is spoiled only for $m = 0$, $a < 0.5$

problem at hand. The fit can be seen on Fig. 4.32. Clearly this formula offers a very good fit to the data, except for the case $m = 0$, $a < M$ where this formula gives zeros, differing from our numerical results. Numerically, if we compare ALL the points obtained in our numerical evaluations (the two lowest $n = 0$ modes for $a < M$ corresponding to $N = 0, 1$ in Eq. (4.18) and the only two modes available for $a > M$, which corresponds to $N = 0, 1$ in Eq. (4.18), for $m = 0, \pm 1, \pm 2$) with the values calculated with formula (Eq. (4.18)) for the corresponding a, the two sets coincide with at least 5 digits in the worst few cases, and with at least 10 digits for most of the points. Taking into account that this exact formula is analytically obtained from the properties of the confluent Heun functions in the case of polynomial condition imposed on the *TRE* and not on TAE and that the routines with which MAPLE evaluates the Heun function and their precision are unknown, this match is extremely inspiring. Besides, it poses many questions about the physics behind this formula.

The formula (4.18) appears without derivation also in [59] (also in [140]), where the authors impose QNM boundary conditions meaning they work with the *regular* solutions of TAE. In their paper, the formula (Eq. (4.18)) is written in terms of the temperature of the horizon and according to the authors it fits very well the frequencies they obtained for the case $l = m = 2$ $(=| s |)$ and also it matches the imaginary parts of the modes $(n = 1, 2, 3...)$ when $m > 0$ (for the other cases it doesn't work).

In contrast, in our numerical results, formula (Eq. (4.18)) describes the lowest mode $(n = 0)$ of all the m equally well (except $m = 0$, $a < M$), while it fails to describe the modes with $n > 0$ – the formula ω for $N = n$ or $N = n + 1$ matches only the relative magnitude of the modes and has no resemblance to their highly

nontrivial behavior. The fit doesn't improve even for the highest mode ($n = 20$) we were able to obtain. A surprising similarity between the two cases (jets and QNM) is that the real parts of the higher modes ($n > 0$) in our results also seem to tend to the lowest mode $\omega_{0,m} \equiv \omega_{cr}^{jet}$. However, since in our case, the frequencies come in pairs, the frequencies with opposite to ω_{cr}^{jet} sign do not tend to ω_{cr}^{jet}, but they have a definite limit.

Despite the differences, the appearance of formula (Eq. (4.18)) in the two cases corresponding to different physical problems is interesting and raises questions about the underlying physics it represents. It also contributes to the validity of our approach, since our results are comparable in some points with [59] who use a completely different, but well established in QNM physics numerical approach (Leaver's method of continued fractions).

Additionally, one may use the so-obtained spectrum, to plot how the angular solution changes with the rotational parameter a. Example for one of those frequencies $m = 0, N = 1$ can be found on fig. 4.33. Clearly, there is some form of critical event at $a = M$, which can be seen even in the angular solution. Furthermore, the primary jets, seem to appear around both the horizontal and the vertical axes, in contrast with the expectation of jets only in the direction of the rotation. (Here, we plot the cross-section $\phi = const$, where on the axes we have the Cartesian coordinates – x, y [12]).

4.3.3 Summary of the results

We presented new results of the numerical studies of our model of central engine inspired by the properties of GRB. We have already showed that the polynomial requirement imposed on the TAE leads to a collimated jet-like shapes observed in the angular part of the solution, thus clearly offering a natural mechanism for collimation due to purely gravitational effects([36]).

Continuing with the TRE, we impose standard black hole boundary conditions and we obtain a highly nontrivial spectra $\omega_{n,m}(a)$. The numerical spectra for the lowest modes $n = 0$ is best described by the analytical result in [67], where, however, the polynomial conditions are imposed on TRE instead. Although unexpected, this fit serves as a confirmation of both our numerical approach and the analytical result and it is a hint for the deeper physics at work in those cases. Interestingly, the formula in question (Eq. (4.18)) works only for the lowest mode ($n = 0$) for each m and correctly describes two frequencies with coinciding for $a < M$ real parts and different imaginary parts (zero and comparable to the real part accordingly). The modes with higher n are not described by it and have highly nontrivial behavior – they seem to have a definite limit, which coincides with the critical frequency in some of the cases.

[12] Note that in MAPLE, the spherical coordinates are defined by $x = r\sin(\phi)\cos(\theta), y = r\sin(\phi)\sin(\theta), z = rcos(\phi)$ and thus the intervals for the angles are $\phi = [0, \pi], \theta = [0, 2\pi)$ and one should be careful with the change of variables

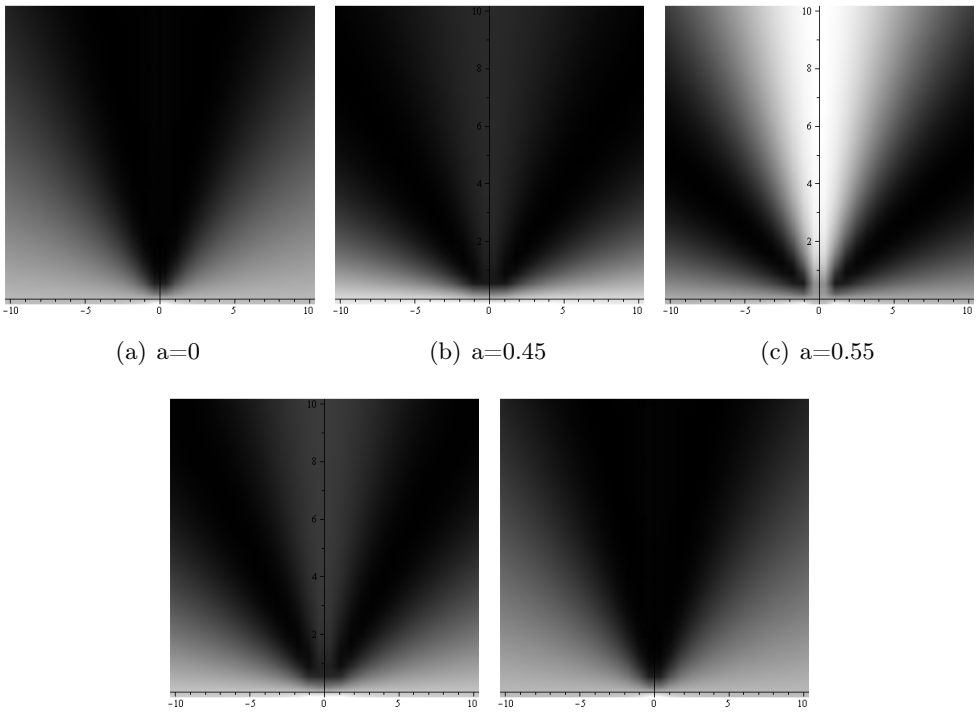

(a) a=0 (b) a=0.45 (c) a=0.55

(d) a=0.7 (e) a=1.5

Figure 4.33: Density plot of the value of the solution for one of the roots of the radial equation – $\omega = -m + 4i\sqrt{1/4a^2 - 1}$ for $m = 1$, $a = 0..1.5$, $\phi = const$

The imaginary part of our complex frequencies remains positive, ensuring stability of the solutions in direction of time-future infinity and indicating an explosion in direction of time-past infinity. There is, however, an obviously critical transition when $a \to M$, where the imaginary part of the frequency decrease to zero suggesting slower damping with time. This could have interesting implications for rapidly-rotating black holes or naked singularities close to the extremal regime. As we have shown the value $M/a = 1$ describes a bifurcation of Kerr metric. For $a >> M$, the imaginary part remains approximately constant in both directions. This is surprising, since according to theory of QNM of KNS, the naked-singularity regime should be unstable. There is no contradiction, because the different boundary conditions we use, define different physical situation – we work with jets from KBH or KNS. Our numerical results suggest that these jets are stable even for a KNS.

Chapter 5

Summary and conclusions

In this thesis we have presented our study of the spectra of linearized perturbations of rotating and non-rotating black holes in the following cases:

1. Jets from rotating black holes: electromagnetic perturbations.

2. Quasi-normal modes of non-rotating black holes: electromagnetic and gravitational perturbations.

3. Quasi-normal modes of rotating black holes: electromagnetic perturbations.

The spectra were obtained for the first time, using the novel approach of imposing the boundary conditions directly on the exact analytical solutions of the differential equations, instead of to some their approximation, thus allowing a more physically clear interpretation of the results and also more control over the problematic regions in the complex plane, such as branch cuts.

In this work, two types of boundary conditions were considered – **the quasi-normal boundary conditions** consisting of the black hole boundary conditions and the angular *regularity* condition; and **the jet-boundary conditions** consisting of the black hole boundary conditions and the angular *singularity* condition. As expected, the different boundary conditions led to different spectra, which can be used as a characteristic signature of the astrophysical object which produced them. This is particularly important in view of the recent developments in observational astrophysics, which ask for a reconsideration of the theory of the central engines of GRBs. To facilitate the application of the results in astrophysics, the spectra of the electromagnetic quasi-normal modes of the Kerr black hole were presented in physical units.

The summary of the results is:

1. The spectrum for the modes of the BH primary jets, was obtained for the first time. It was demonstrated that it is qualitatively different from the QNM spectrum, even though they differ only by the condition imposed on the solutions of the angular equation. Its important property is that it is stable in both the black hole and the naked singularity regime. We also showed that not all the obtained modes obey the black hole boundary condition – some of them correspond to white-hole boundary condition. An analytical formula was found which fits with very high precision the two lowest modes in this case.

2. The quasi-normal frequencies of non-rotating BH described by the Regge-Wheeler equation and also the Teukolsky radial equation for $a = 0$ (for $s = -2$) were calculated, solving both the corresponding radial equations or the transcendental system of spectral equations featuring the confluent Heun functions. In the so-obtained spectrum, the modes with $n < 3$ coincide with high precision with the

already-published by other authors frequencies. The modes with higher n, however, show important deviations. Those differences are partially due to the existence of branch cuts in the solutions of the radial equation.

3. To study the effect of the branch cuts on the numerically obtained frequencies, the epsilon-method was introduced. Using this method, one can move the branch cuts and thus to study the dependence of the frequencies on the argument of the complex radial variable. This method was used in the case of gravitational QNMs of non-rotating black hole to confirm $n = 8$ that is not an algebraically special mode. Also, with the ε-method, for the first time here is studied the dependence of the so-obtained frequencies on small deviations in the phase condition and it is shown how this non-trivial dependence evolves with n. In this case, some of the modes are independent of ε, which should be expected since the frequencies should not depend on the radial variable. Other modes, however, depend critically on the value of ε and they can differ seriously from the already published results.

4. The quasi-normal frequencies of KBH were calculated for the first time, solving directly the two-dimensional transcendental system of spectral equations featuring the confluent Heun functions. For low n, the so-obtained results also repeat with high precision the already published by other authors results. For high n, the frequencies once again demonstrate a dependence on the proximity of a branch cut of the solution of the radial equation. This dependence persists with the increase of the rotation and it may lead to profiles in the complex plane, significantly deviating when obtained for different values of ε. Therefore, using the ε-method, we were able to produce new QNM spectra, different from the already known one. Such new spectra poses the question which one should be compared with astrophysical observations and why.

As a conclusion, the exploration of the application of the confluent Heun functions in studying the QNMs and the primary jet modes of the Schwarzschild and the Kerr metric showed that by using the exact solutions of the differential equations, one can obtain different spectra for different boundary conditions and values of the parameters and thus to obtain both more complete picture of the already known spectra and also qualitatively new information.

Additionally to the physical problems we considered, to obtain the quasi-normal spectra, we developed a new root-finding algorithm for solving two-dimensional systems of two complex-valued transcendental equations. The new method was tested in different elementary systems and it was successfully used to obtain the QNM spectra presented here. Since the Heun-type equations occur in various physical problems (discussed in Chapter 2: "The confluent Heun Equation and its solutions"), the method can have numerous applications.

The epsilon-method which we used to move the branch cuts in the solutions of the TRE can be further used to study the stability of the solutions around the singular point at infinity in the whole complex plane. The stability of the solutions around this point, is still an open question, since the frequencies we obtained depend seriously of the value of the parameter ε, i.e. of the position in the radial complex plane.

Finally, this work was also a test for the numerical realization of the confluent Heun functions in MAPLE, which currently is the only software package able to work with them. Our results show that although flawed, the MAPLE subroutines evaluating the confluent Heun function are able to produce the expected from the theory results and also qualitatively new results, thus they can be used in other fields of the physics and the science as a whole. Our work also showed the importance of the Heun functions to the physics and the need of better algorithms for their evaluation.

Appendix A

Numerical methods

A.1 Overview of the problems in front of root-finding algorithms

From the previous chapters, it is clear that the Heun functions offer many opportunities to the physics. The work with them, however, is more than complicated, due to the lack of well developed analytical theory of those functions. In this situation, the best approach is to rely on the numerical realization of those functions in the software package MAPLE. This realization, however, has some important problems which were discussed in the chapter dedicated to those functions. The key problems are:

1. There are points for which the routines which evaluate those functions break down, thus one cannot rely on the analytical properties of the function in the whole complex plane.

2. The derivative of the confluent Heun functions outside of the unit-circle $|z| < 1$ has lower precision than the function at the same point.

3. The evaluation of the confluent Heun function in the complex domain relies on numerical integration, which means that it can be significantly slower than the evaluation of other special functions (for example, the hypergeometric function). This happens only for $|z| > 1$, since for $|z| < 1$ there are appropriate power-series expansions. This, however, means that when solving equations featuring those functions, the convergence of the root-finding algorithm is essential.

An example of application of the confluent Heun functions is the problem of quasi-normal modes (QNM) of rotating and non-rotating black holes. In this case, one has to solve a two-dimensional connected spectral problem with two complex equations in each of which one encounters the confluent Heun functions.

Solving such system of two complex-valued nonlinear transcendental equations numerically is a task with varying difficulty, depending on the non-linearity of the system, the types of functions involved and the dimension of the space determined by the system. There are many well-known iterative root-finding algorithms, but most of them are specialized and optimized to work with a narrow set of functions – for example polynomials or functions with real-valued roots. The two most heavily relied upon one-dimensional algorithms – the secant method and Newton's method (or the Newton-Raphson method, [143, 144, 145, 146]) can work with a wide set of complex valued functions under proper conditions (see [146]), but they have their weak sides. Newton's method requires the evaluation of the function and its first derivative at each iteration. This increases the computational cost of the

algorithm and it makes the algorithm unusable when the procedure evaluating the derivative of the function has numerical problems (for example see the discussion for the Heun functions below) or when derivative becomes zero or changes sign. The secant method avoids this limitation, but in the general case, it has lower order of convergence (~ 1.618) compared to that of Newton's method ($= 2$) and the convergence of both of them is strongly dependent on the initial guess.

These problems of the algorithms are inherited by their multi-dimensional versions such as the generalized Newton-Raphson method ([145]) and the generalized secant method (Broyden's method, [147]). Although those problems can have varying severity, there are systems in which those algorithms cannot be used effectively. There are also some novel approaches (see [148], [149]), but when they rely on the same one-dimensional algorithms, they are likely to share their weaknesses as well. Clearly there is a need for new algorithms that will enlarge the class of functions we are able to work with efficiently.

Particularly, for systems featuring confluent Heun functions, the Newton's method cannot be used as a root-finding algorithm. Broyden's algorithm works well in most cases, but it is slowly convergent even close to a root. It is clear, then, that we need a novel algorithm, that will offer quicker convergence than Broyden's algorithm, but without relying on derivatives. One such algorithm, in the case of a system of two equations in two variables, is the two-dimensional generalization of the Müller algorithm which out team developed. The one-dimensional Müller algorithm ([150]) is a quadratic generalization of the secant method, that works well in the case of a complex function of one variable. It has very good convergence for a large class of functions (~ 1.84) and it is very efficient when the starting point (the initial guess) is close to a root. It is also well convergent when working with special transcendental functions. The two-dimensional Müller algorithm seems to inherit some of the advantages of its one-dimensional counterpart like good convergence and usability on large class of functions as our tests show. The new algorithm was used to solve the QNM problem in the case of a Schwarzschild black hole and it proved to work without significant deviations from the results published by Andersson ([58]) and Fiziev ([62]). Also, preliminary results for the QNM of the Kerr black hole are discussed and for them we also obtain a very good coincidence with published results [94].

The chapter is organized as follows: Section 2 reviews the one-dimensional Müller algorithm and its two-dimensional generalization, in Section 3 we discuss some physical application of the method and the numerical results obtained with it and in Section 4 we summarize our results. In the Appendix, the new algorithm is tested on various additional and more simple examples to verify its functionality.

A.2 The Müller algorithm

A.2.1 One-dimensional Müller's algorithm

The one-dimensional Müller algorithm ([145, 150]) is iterative method which at each step evaluates the function at three points, builds the parabola crossing those points and finds the two points where that parabola crosses the x-axis. The next iteration is the the point farthest from the initial point.

Explicitly, for every three points x_{j-2}, x_{j-1}, x_j and the corresponding values of the function $f(x) \to f_{j-2}$, f_{j-1}, f_j, the next iteration x_{j+1} is:

$$x_{j+1} = x_j - (x_j - x_{j-1}) \frac{2C}{max(D_1, D_2)}, \text{ where}$$
$$A = f_j\, q - q(1+q) f_{j-1} + q^2 f_{j-2},\ B = (2\,q+1)\, f_j - (1+q)^2\, f_{j-1} + q^2 f_{j-2},$$
$$C = (1+q)\, f_j,\ D_{1,2} = B \pm \sqrt{B^2 - 4\,AC} \text{ and } q = \frac{x_j - x_{j-1}}{x_{j-1} - x_{j-2}}.$$

We will indicate the one-dimensional Müller algorithm by the map:

$$\mu: \quad \mu(x^{in}, F(x)) \underset{P}{\longrightarrow} x^{fin},$$

where x^{in}, x^{fin} are the starting and end points of the algorithm and the integer P is the number of iterations in which the algorithm completes.

The exit-condition for the one-dimensional Müller algorithm is $|\, x_P - x_{P-1}\, | < 10^{-d}$, where d is the number of digits of precision we require. This we found to be the best exit-condition since it works independently of the actual numerical zero in use, which may vary for the confluent Heun function.

The advantages of this algorithm are that it does not use derivatives and generally it has higher convergence than the secant method, especially when used on special functions such as the confluent Heun function. For example the spectra in [62] and [97] was obtained by the authors using that method.

A.2.2 Two-dimensional Müller's algorithm

The two-dimensional Müller method comes as a natural extension of the one-dimensional Müller method.

For two complex-valued functions $F_1(x, y)$ and $F_2(x, y)$ we want to find such pairs of complex numbers (x_I, y_I) which are solutions of the system:

$$\begin{cases} F_1(x_I, y_I) = 0 \\ F_2(x_I, y_I) = 0 \end{cases} \tag{A.1}$$

where $I = 1, \ldots$ numbers the solution in use. From now on, we will omit the index I, considering that we work with one arbitrary particular solution. Finding all the solutions of a system is beyond the scope of this article.

Consider the functions $F_1(x, y)$, $F_2(x, y)$ as two-dimensional *complex* surfaces $z = F_1(x, y)$ and $z = F_2(x, y)$ in a three-dimensional space of the *complex* variables $\{x, y, z\}$[1]. Normally, to solve the system, one expresses the relation $y(x)$ from one of the equations, then by substituting it in the other equation, one solves it for x and from $y(x)$ one finds y. In the general case, however, this is not possible. The idea of our code is to approximately follow that procedure by finding an approximate linear relation $y(x)$ between the two variables and then using it to find the root of function of one variable trough the one-dimensional Müller algorithm.

To find the linear relation $y(x)$, at each iteration we form the plane passing trough three points of one of the functions and then the equation of the line of intersection between that plane and the plane $z = 0$ is used as the approximate relation $y(x)$. This basically means that the so found $y(x)$ is an approximate solution of one of the equations which ideally should be near the real solution in the $z = 0$ plane. Substituting this relation in the other function, we run the one-dimensional Müller algorithm on it to fix the value of one of the variables, say x. Using the value of x in the first function, we again run the one-dimensional Müller algorithm on it to fix the value of the other variable – y. Alternatively one can substitute the value of x directly in $y(x)$ to obtain y. This ends one iteration of the algorithm. The process repeats until the difference between two consecutive iterations becomes smaller than certain pre-determined number. This process is systematized on Fig. (A.1).

Explicitly, the code starts by evaluating the two functions $F_{1,2}(x_i, y_i)$ in three starting pairs of points ($i = 1, 2, 3$) that ideally should be near one of the roots of the system. In our case, those three *initial* pairs are obtained from one starting pair to which we add and subtract certain small complex number. This artificial choice is done only in the first iteration ($n = 3$), afterwards we use the output of the last three iterations to form $(x_{n-2}, y_{n-2}), (x_{n-1}, y_{n-1})$, (x_n, y_n) and the respective $F_{1,2}(x, y)$. Thus on every iteration after $n = 3$ the actual complex functions $F_{1,2}(x_n, y_n)$ are evaluated only once outside of the one-dimensional Müler subroutines.

Next we construct the plane passing trough those three points for one of the functions, say F_2 by solving the linear system:

$$\begin{aligned} C_1 x_{n-2} + C_2 y_{n-2} + C_3 &= F_2(x_{n-2}, y_{n-2}) \\ C_1 x_{n-1} + C_2 y_{n-1} + C_3 &= F_2(x_{n-1}, y_{n-1}) \\ C_1 x_n + C_2 y_n + C_3 &= F_2(x_n, y_n). \end{aligned}$$

From it one obtains the coefficients C_1, C_2, C_3 of the plane $z = C_1 x + C_2 y + C_3$.

This plane is intersected with the plane $z = 0$ (i.e. $C_1 x + C_2 y + C_3 = 0$) and the equation of the line between those two planes is the approximate relation $y(x)$ of the two variables.

We substitute that relation in the first function $F_1(x, y) \to F_1(x, y(x))$ and we start the one-dimensional Müller on that "linearized" function of only one variable,

[1] Equivalently, we can consider four *real* surfaces in five-dimensional *real* hyperspace, which are defined by four *real* functions of four *real* variables

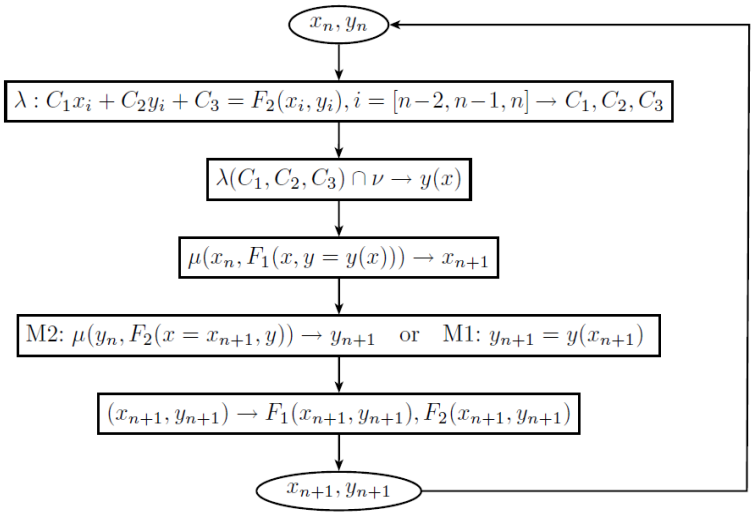

Figure A.1: A block scheme of the two-dimensional Müller algorithm. $\lambda(C_1, C_2, C_3)$ is the plane with equation $z = C_1x + C_2y + C_3$ that crosses trough the 3 pairs of points (x_i, y_i) and the function F_2 evaluated in them. The plane ν is defined by the equation $z = 0$. The one-dimensional Müller algorithm, $\mu(t^{in}, F(t)) \rightarrow t^{fin}$, is applied on the function of *one variable* $F(t)$ with starting point t^{in} and final point t^{fin}.

x. After some pre-determined maximal number of iterations, the exiting point is chosen for x_{n+1} ($\mu(x_n, F_1(x, y = y(x))) \rightarrow x_{n+1}$ [2]) .

Then, there are two possibilities.

Algorithm M1: one could use directly the relation $y(x = x_{n+1})$ to find $y = y_{n+1}$. Or,

Algorithm M2: One can substitute $x = x_{n+1}$ in the other function $F_2(x, y) \rightarrow F_2(x = x_{n+1}, y)$ in order to find y_{n+1} using again the one-dimensional Müller algorithm ($\mu(y_n, F_2(x_{n+1}, y)) \rightarrow y_{n+1}$).

Our numerical experiments showed that both approaches lead to convergent procedure.

After (x_{n+1}, y_{n+1}) are fixed, the two functions $F_{1,2}(x_{n+1}, y_{n+1})$ are evaluated and if the new points are not roots, the iterations continue.

The exit-strategy in the two-dimensional Müller algorithm is as follows:

1. To avoid hanging of the algorithm or its deviation from the actual root of the system, we fix maximal number of iterations for the one-dimensional Müller subroutine, P. From our experience small P (3–10) gives best convergence.

2. The precision-condition ($\mid x_j - x_{j-1} \mid < 10^{-d}$) remains in force for the one-dimensional Müller. Usually the algorithm exits, because of $j > P$ during the

[2] Since the maximal number of iterations in the one-dimensional Müller algorithm is fixed, for simplicity we will omit the index P in this sub-section. The index of the iterations of the two-dimensional Müller algorithm is n.

first few iterations of the two-dimensional Müller and the closer to the roots it gets, the smaller number of iterations are needed in the one-dimensional Müller to reach d and to exit.

3. The precision d defined by the absolute value of the difference between two consecutive pairs (x_n, y_n) (combined with the values of functions $F_1(x, y), F_2(x, y)$ at them) – $\mid x_n - x_{n-1} \mid < 10^{-d}, \mid y_n - y_{n-1} \mid < 10^{-d}$ is the primary exit-condition of the two-dimensional Müller. When d becomes smaller than certain value, the algorithm exits with a root.

4. To keep the two-dimensional Müller algorithm from hanging, a maximal number of iterations N is set after which the algorithm reaches exits without fixing a root.

5. A common problem occurs when one of the functions becomes zero before the other function. In those cases, the algorithm accepts the fixed value for a root, say x^{fin}, and runs the one-dimensional Müller on the other variable until it fixes a root – $\mu(y_n, F_2(x^{fin}, y)) \to y^{fin}$. The algorithm then exits with a possible root: (x^{fin}, y^{fin}).

The procedure can be fine-tuned trough change in the starting pair of points, the initial deviation or by switching the places of the functions, or even by replacing the functions with their independent linear combinations.

As we will show in what follows, this method inherits some of the advantages of the one-dimensional Müller algorithm, like the quick convergence in proximity of the root and the vast class of functions that it can work with. The major disadvantage comes from the complicated behavior of the two-dimensional complex surfaces defined by the functions $F_{1,2}(x, y)$ which require one to find the best combination of starting points and number of iterations in the one-dimensional Müller subroutine so that the algorithm converges to the required root (if it is known or suspected). Generally, it is hard to tell when one point is "close" to a root. In some cases, even if certain starting pair of points is close to a root in terms of some norm, using it as a starting point in the algorithm may still lead to convergence to another root or simply to require more iterations to reach the desired root than if other pair of starting points were used.

It is important to note that unlike Broyden's algorithm and Newton's algorithm which are not dependent on the order of the equations in the system, our two-dimensional Müller algorithm depends on the order of the equations. The numerical experiments show that while for some systems, changing the places of the equations has little or no effect on the convergence, in other cases, it slows down or completely breaks down the convergence. While such inherent asymmetry certainly is a weakness of the algorithm, there are ways around it. For example, one may alternate the places of the equations at each iteration or use their independent linear combinations ($F^*_{1,2} = \alpha_{1,2}F_1 + \beta_{1,2}F_2$). Those approaches make the algorithm more robust, but since they may cost speed, we prefer to set the order of the equations manually.

A technical disadvantage is that the whole procedure is more CPU-expensive than Newton's method and Broyden's method, since it generally makes more evaluations of the functions – each one-dimensional Müller makes at least 1 iteration on every step of the two-dimensional Müller, thus it makes at least 4 evaluations of each function. This is because on each iteration of the two-dimensional Müller algorithm the functions in use change and thus one cannot use previous evaluations to reduce time. Still, in some cases, as demonstrated in [128] for some simple examples and also below, the so-constructed algorithm is quicker or comparable to Newton's or Broyden's method.

A.3 Numerical testing

All the algorithms are realized as procedures on the software package MAPLE, the tests are done on MAPLE 15, on Linux x64, CPU Intel Centrino Core 2 Duo, on 2.2GHz. The number of digits that MAPLE uses when making calculations with software floating-point numbers is set to 64. For Newton's method and Broyden's method we used the analytical formulas [145], where the Jacobian in both cases is evaluated exactly or with finite differences respectively (i.e. without the Sherman-Morrison formula).

The times presented below are obtained after running each procedure 10 times using the garbage collection function $gc()$; in MAPLE on each calculation, so that each run represents an independent numerical experiment. The total time for each method is then divided by 10 and rounded to 3 digits of significance. This way, even though the times depend on the system load at the moment, they are representative for the four methods in each example. The notable exception of this "averaging" are all the systems featuring Heun functions, where such procedure would require too much time and thus they are evaluated only once, using the function $gc()$;.

The precision in all the examples is 15 digits, but only the first 10 after the decimal point are presented here. In all the cases, the initial deviation where needed is 0.001. Some of the examples are from [151] p.617-618.

The numerical results for the test-systems are summarized in Table A.1 in the Appendix. In it, we compare Newton's method, Broyden's method and the two versions of the two-dimensional Müller algorithm discussed in section 2.2. – $M2$ which uses *two* one-dimensional Müller subroutines to fix the (x_{n+1}, y_{n+1}) and $M1$ which uses *one* one-dimensional Müller subroutine to find x_{n+1} and then it evaluates directly $y_{n+1} = (-C_3 - C_1 x_{n+1})/C_2$. The number in the brackets in the N_{M1} and N_{M2} columns is P, the maximal iterations in the one-dimensional Müller subroutine. Everywhere in the table, for each (x^{in}, y^{in}), the four algorithms exit with the same (x^{fin}, y^{fin}) with precision of 15 digits.

A.3.1 Elementary functions

1. $F_1(x, y) = y^2 + 3x - 5 + x^2 = 0$
   $F_2(x, y) = x^2 + 3y - 1 = 0$

2. $F_1(x,y) = x(1-x) + 4y = 12$
   $F_2(x,y) = (x-2)^2 + (2y-3)^2 = 25$

For those systems (rows S=1,2 in table A.1), the number of iterations and the time needed to find a root in the two-dimensional Müller algorithms (for M1 in particular) are generally close to those of Broyden's algorithm ($t_N < t_B \approx t_{M1} < t_{M2}$). For real roots, however, the algorithms M1 and M2 are the *quickest* of the four.

A.3.2 Trigonometric, exponential and logarithmic functions

3. $F_1(x,y) = y - 1/4\sin(x) - 1/4\cos(y) = 0$
   $F_2(x,y) = 5x^2 - y^2 = 0$

4. $F_1(x,y) = exp(-3x)\cos(y) + x = 0$
   $F_2(x,y) = x^2 - 3yx + y^2 = 0$

Again, for real roots, the two-dimensional Müller methods are quicker than both other methods (rows S=3,4 in table A.1). Newton's method is much quicker when the initial conditions and the roots are complex.

It is important to discuss the dependency of two-dimensional Müller methods (M1 and M2) from the maximal number of iterations in the one-dimensional Müller subroutine, P. In many cases, changing P only affects the time needed for the algorithms to complete. There are cases, however, where this parameter becomes critical. For example, when one uses as starting points (4.4-5.0i, 8.5-16i) on the system $S = 5$, the following 7 roots are obtained:

$$r_0 = (0.3487096094 + 0.4633971546i, 0.9129336096 + 1.2131895010i)$$
$$r_1 = (3.0248444374 - 4.3689275542i, 7.9191455477 - 11.4380008313i)$$
$$r_2^{\pm} = (0.1632674377 \pm 0.6065137375i, 0.0623626119 \pm 0.2316676331i)$$
$$r_3 = (1.1119158619 - 1.8296636950i, 2.9110335191 - 4.7901217415i)$$
$$r_4 = (4.0158133827 - 5.6039287836i, 10.5135359284 - 14.6712760260i)$$
$$r_5 = (-5.3999170768 - 3.12 \times 10^{-37}i, -14.1371664435 - 4.38 \times 10^{-43}i)$$

From them, Newton's method converges to the root r_0 (after 25 iterations), Broyden's method – to r_1 (after 27 iterations). With the two-dimensional Müller methods (M1 and M2) depending on the parameter P one obtains:

- with M2: r_2^+ for $P = 3, 9, 10, 12 - 14$ and $P > 16$, r_0 for $P = 5$, r_5 for $P = 6$, and r_2^- for $P = 8$ (after averagely 10 iterations),
- with M1: r_3 for $P = 3$, r_4 for $P = 4 - 10$ and $P > 16$ and r_1 for $P = 11 - 14$ (after averagely 11 iterations).

Similar behavior is observed in the next example:

5. $F_1(x,y) = \ln(x^2+y^2) - \sin(yx) - \ln(2) + \ln(\pi) = 0$
   $F_2(x,y) = e^{x-y} + \cos(yx) = 0.$

For real starting points, Newton's method is not convergent, since it remains locked to the real axis. Broyden's method also did not exit with a root for real starting points. The two-dimensional Müller methods on the other side, when started from (0.5,0.5) gave the root r_1^- (see below). Other purely real initial conditions either gave a root or the algorithm did not converge.

Using the complex initial conditions (2.27+0.001i, 1.27), the following four roots were found:

$$r_0 = (0.2129109625 - 2.4380400935i, -1.3216238026 - 4.6551486236i)$$
$$r_1^{\pm} = (0.9203224533 \pm 0.7487874838i, 1.4188731053 \mp 0.5453380689i)$$
$$r_2 = (-1.6645201248 + 1.380553001i, 1.66452012482 + 1.38055300197i)$$

Newton's method exits with r_0 after 24 iterations. Broyden's algorithm is not convergent. From the two-dimensional Müller algorithms one obtains:

- with M2 after averagely 12 iterations: r_1^- for $P = 3$, r_2 for $P = 4$ and r_1^+ for $P \geq 5$.
- with M1 after averagely 14 iterations: r_1^+ for $P = 3$ and $P \geq 5$ and r_1^- for $P = 4$.

From the last two systems it is clear that P represents an additional parameter of the two-dimensional Müller algorithm. It can be used to improve convergence, but in some cases, it can lead to different roots for the same initial conditions. Such instability depends on the system and it can be avoided by starting the algorithm closer to the root.

A.3.3 Special functions

Finally, we consider the following two systems:

6. $F_1(x,y) = x^2 - y + 5\sin(x-2) = 0$
   $F_2(x,y) = \mathrm{J}(3,y) + 5x - 3 = 0$

7. $F_1(x,y) = x^7 - e^y + {}_2F_2([1],[3],x^2-3x) = 0$
   $F_2(x,y) = H^1(7, y+1-x) = 0$

where $J()$ is the Bessel functions of the first kind, $H^1()$ is the Hankel function of the first kind and ${}_2F_2$ is the generalized hypergeometric function.

In this case (rows S=6,7 in table A.1) the two-dimensional Müller algorithms are comparable to Newton's algorithm, while Broyden's algorithm is often the quickest of the four. This is likely due to the computational burden of the derivative or of

each additional function evaluation. Note, however, that our goal is not to have an algorithm that is better than Newton's method, but to have an algorithm that has good convergence and that does not need to evaluate derivatives. In that, the performance of the new algorithms is satisfactory, especially since in some cases like 6.2 and 6.3, Müller's algorithms are the quickest.

A.3.4 Discussion

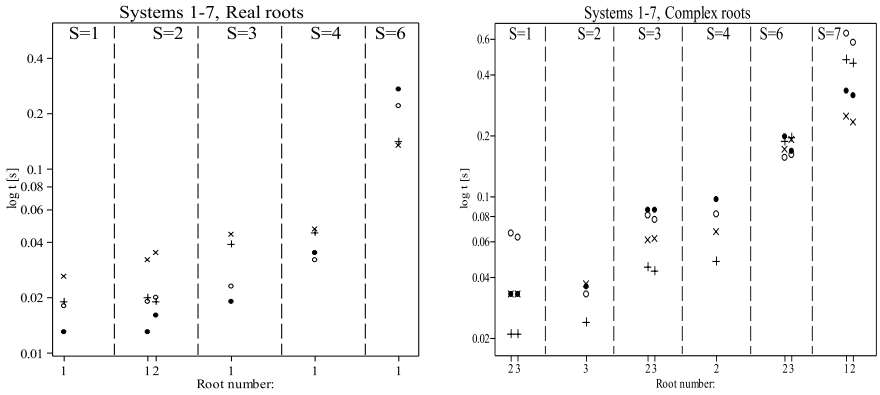

Figure A.2: A graphical comparison between the times needed by the Newton method, the Broyden method and the Müller methods M1 and M2. With red we denote Newton's method, with green – Broyden's method, with blue – M1, with black – M2.

The numerical investigations above (see Fig.A.2 and also table A.1) show that in general, the two modifications of the two-dimensional Müler algorithm work comparably well to the more established algorithms – Newton's and Broyden's, even if sometimes they require more time and iterations to fix a root. In some specific cases, like those with real roots or those featuring confluent Heun functions (see Section 3), however, the two-dimensional Müler algorithms are often the quickest of the four.

It was demonstrated that while in Newton's and Broyden's algorithms the exit points depend only on the starting points (when the initial deviation is fixed), the two-dimensional Müller algorithm depends also on the number of iterations in the one-dimensional Müller subroutine (P). Surprisingly, the time for fixing a root do not depend in a straight-forward way from P, since sometimes increasing P leads to decreasing of the total time. This can be expected, because P is the maximal number of iterations in the one-dimensional Müller subroutine, but the actual number of iterations depends on the precision. Therefore, this is one more way to fine-tune the algorithm to achieve a known or suspected root.

The examples also showed the importance of the order of the functions in the system (see the systems in the table A.1 marked with * and †). While in most cases all the four algorithms find at least one root of the system, there are initial conditions

which lead to a divergence or to "undesired" root. This problem can be avoided by starting the procedure closer to the root, changing the places of the equations in the system or using a linear combination of the functions (say $F_1 \to F_1+F_2$, $F_2 \to F_1-F_2$). We conclude that even though the new algorithms admit some further improvements and developments, they work well enough to be tested in real physics problem.

S	$(x)^{initial}$ $(y)^{initial}$	$(x)^{final}$ $(y)^{final}$	t_{Newton}[s] N_{Newton}	$t_{Broyden}$[s] $N_{Broyden}$	t_{M2}[s] N_{M2}	t_{M1}[s] N_{M1}
1	1.689 -0.637	1.1890465736 -0.1379439181	0.019 8	0.026 10	0.018 10*(3)	0.013 8(3)
	$1.321+3.520i$ $3.738-1.927i$	$0.8214691720+3.5201983985i$ $4.2389950548-11.9278229759i$	0.021 8	0.033 10	0.066 12(3)	0.033 8(3)
	$1.321-3.520i$ $3.738+1.927i$	$0.8214691720-3.5201983985i$ $4.2389950548+1.9278229759i$	0.021 8	0.033 10	0.063 12(3)	0.033 8(3)
2	$-.5$ 3	-1.0000000000 3.5000000000	0.020 8	0.032 10	0.019 9(4)	0.013 9(3)
	3.046 3.484	2.5469464699 3.9849974627	0.019 8	0.035 10	0.020 10(3)	0.016 9(3)
	$0.726+4.335i$ $-2.242–0.592i$	$0.2265267650+4.3352949767i$ $-1.7424987313-0.5927935709i$	0.024 8	0.037 9	0.033 7(6)	0.036 8(6)
3	0.621 -0.228	0.1212419114 0.2711051557	0.039 10†	0.044 13†	0.023 9(3)†	0.019 8(4)*†
	$-0.422+1.476i$ $-2.562+3.301i$	$-.9222203725+1.4764038337i$ $-2.062147443+3.3013393343i$	0.045 9	0.061 11	0.081 8(4)	0.086 11*(3)
	$1.468-1.635i$ $-2.665+3.656i$	$0.9685241736-1.6351708695i$ $-2.1656858901+3.6563532190i$	0.043 9	0.062 11	0.077 7(5)	0.086 11*(3)
4	$-.35$ -1.05	-0.5600551872 -1.4662435158	0.045 11	0.047 12	0.032 7(4)	0.035 10(4)
	$0.55-0.6i$ $1.14-1i$	$0.3487096094-0.4633971546i$ $0.9129336096-1.213189501i$	0.048 10	0.067 12	0.082 7(6)	0.097 13*(3)
6	$1.2+0.09i$ $-5.5+0.01i$	.6863031247 -4.3646459533	0.141 9†	0.134 11†	0.220 9*(4)†	0.271 11(3)†
	$7.2-3.6i$ $-11.9+5.001i$	$5.8404591703-3.0854927956i$ $-10.6712592035+5.7445552813i$	0.188 11	0.171 14	0.156 10*(3)	0.198 14*(4)
	$-5.1-1.006i$ $16.0+5.51i$	$-4.9297777922-1.1922443124i$ $17.4620338366+5.7870418188i$	0.196 11	0.191 15	0.161 11(3)	0.168 13(3)
7	$1.1-.45i$ $-2.4-4.2i$	$0.8288091244-0.4046494664i$ $-2.3507488745-4.6830120304i$	0.476 10	0.249 13	0.640 11(3)	0.333 12(3)
	$.5-.87i$ $-3.21-5.14i$	$0.2656154750-0.8757700972i$ $-2.9139425238-5.1541326612i$	0.457 10	0.233 13	0.577 8*(4)	0.316 11*(3)

Table A.1: S numbers the system in use, t and N label the time and the iterations needed for the algorithms to exit. * denotes the roots dependent on the order of the equations in M1 and M2. In the † case, the places of the equations were switched to obtain that root.

A.4 Some applications of the method – QNMs of non-rotating and rotating black holes

We will work only with the confluent Heun functions, which are much better studied than the other types of Heun functions, due to their numerous physical applications. Besides their numerical implementation was used successfully in previous works by the authors. For details on the numerical testing, see [128].

A.4.1 First example: Non-rotating black hole

First, we consider the problem of the gravitational QNMs of a nonrotating black hole so that the precision of the new method can be tested on a very well studied physical problem. The physical results in this case were published in [110], so here we will focus on the numerical details instead.

To find the QNMs, one uses the exact solutions of the Regge-Wheeler equations, describing the linearized perturbations of Schwarzschild metric, in terms of confluent Heun functions([62]). From [62], when the mass of the BH is set to $2M=1$, we obtain the following system of the type (A.1):

$$F_1 = (\cos(\theta)-1)(\cos(\theta)+1)\text{LegendreP}(l,2,\cos(\theta)) = 0 \tag{A.2}$$
$$F_2 = \text{HeunC}\Big(-2\,i\omega, 2\,i\omega, 4, -2\,\omega^2, 4-l-l^2+2\,\omega^2, 1-|\,r\,|\,e^{-i((\pi+\varepsilon)/2+arg(\omega))}\Big) = 0,$$

where ω is a complex frequency, l is the angular momentum of the perturbation, $\theta \in [0,\pi]$ is the angle which we set to $\theta = \pi - 10^{-7}$ and $|r| = 20$. HeunC is the confluent Heun function ([106]) in MAPLE notations

Using Eqs. (A.2), we run the two-dimensional Müller algorithm to find the unknown l and ω with precision of the algorithms set to 15 digits.

From the theory, it is known that l is an integer and $l = 2, 3....$ Comparing with the results obtained by the two-dimensional Müller algorithm, for the first root $l = 2$, one has $l = 1.99(9) + 1 \times 10^{-17} i$, with the first different from 9 digit being the 17^{th}. This shows that the new algorithm is capable of solving systems with one purely integer root in the pair with the expected precision.

A comparison of the new algorithm with the well-known Newton's and Broyden's methods, can be found in Table A.2.

Mode:	0	1	2	3	4	5	6	7	8	9	10
t_B [s]	100	99	156	196	386	240	253	282	302	368	398
t_{M2} [s]	317	413	595	741	1175	799	874	892	1364	971	1355
t_{M1} [s]	202	218	335	357	497	457	396	613	623	594	667

Table A.2: The times needed for Broyden's method (t_B) and the two-dimensional Müller methods (t_{M1} and t_{M2}) to fix a root. Note that while the precision of the former is 10 digits, the precision of the other two is $14-15$ digits. To obtain those times, we solve the system: $[F_1+F_2, F_1-F_2]$ with starting points: $\omega[n]+0.01+0.01i, 2.1+0.01i$, where $n = 0..10$.

Because the phase condition $r =\mid r \mid e^{-i(1+\epsilon)\pi/2-iarg(\omega)}$ includes the complex argument in non-analytical way, which cannot be differentiated, this problem cannot be solved directly using Newton's method. Broyden's method works but with serious limitation of its precision. This happens, because one of the roots y in the pair (x, y) is a real integer, while the other is complex and the algorithm fixes the integer root very quickly, thus the finite differences in the Jacobian become infinity. Because of this, the algorithm is able to fix only the first $10-11$ digits, while the other algorithms fix $14-15$ digits. Therefore, although Broyden's algorithm gives better times (see Table A.2) than the two-dimensional Müller algorithms, its precision is much lower and for modes with big imaginary part, it cannot be increased even by raising the software floating-point number to very high values. Furthermore, from Table A.2, one can see that the time needed for the each algorithm to exit with a root dramatically increases with n. This emphasize on the importance of the convergence of the algorithm, which may become critical in physical problems where multiple roots must be found (see the second example).

The numerical results for the QNMs are summed in Table (A.3). In it, the QNM frequencies obtained from Sys. (A.2) are compared to those found by Andersson ([58]) with the phase amplitude method. Recently, those results were confirmed by Fiziev (see [62]) with the one-dimensional Müller method applied on the exact solutions of the radial equation in terms of the confluent Heun function for $l = 2$. To check the accurateness of the new method, we evaluate $\Delta =\mid \omega_{Muller2d}-\omega_{Andersson} \mid$.

n	Our ω	Andersson's ω	Δ
0	0.7473433689+0.177924631i*	0.747343368+0.177924630i	1.68×10^{-9}
1	0.6934219938+0.547829750i*	0.693421994+0.547829714i	3.60×10^{-8}
2	0.6021069092+0.956553966i*	0.602106910+0.956553966i	1.02×10^{-9}
3	0.5030099245+1.410296405i*	0.503009924+1.410296404i	1.01×10^{-9}
4	0.4150291596+1.893689782i*	0.415029160+1.893689782i	4.41×10^{-10}
5	0.3385988064+2.391216108i	0.338598806+2.391216108i	9.67×10^{-10}
6	0.2665046810+2.895821253i	0.266504680+2.895821252i	1.48×10^{-9}
7	0.1856446684+3.407682345i	0.185644672+3.407682344i	3.90×10^{-9}
8	0.030649006+3.996823690i	0+3.998000i**	0.0306
9	0.1265270180+4.605289542i	0.126527010+4.605289530i	1.44×10^{-8}
10	0.1531069502+5.121653272i	0.153106926+5.121653234i	4.52×10^{-8}

Table A.3: A list of the frequencies we obtained for the QNMs of Schwarzschild black hole compared with the numbers found by Andersson. $\Delta =\mid \omega_{Muller2d} - \omega_{Andersson} \mid$. The first 5 frequencies ($n = 0-4$, marked with *) were obtained also by Fiziev using the confluent Heun functions and coincide with the presented here except for the $n = 1$ where the published by Fiziev value is $0.693421994 + 0.547829750i$. The 8th mode, marked with **, was obtained by Leaver [45]. Note that in the table, our results are with negative sign of the imaginary part only to facilitate the comparison. Because of the different sign-convention, the actual sign in front of the imaginary part of our frequencies is *positive*

From the table, it is clear that in most cases, the modes obtained with the

two-dimensional Müller algorithm coincide with those obtained by Andersson with more than 8 digits of precision in most cases and for modes $n = 4, 5, 6$, there are 9 coinciding digits. Since Andersson published 9 digits of his frequencies, such precision is certainly encouraging and shows that both the new method and the confluent Heun functions work satisfactory in this case. These results also confirm the roots for $n = 0, 1, 2, 3, 4$ published in [62].

The mode with biggest deviation from the expected value is $n = 8$ in table A.3 and it was already discussed in the Section "Quasi-normal modes of nonrotating black holes". In brief it is due to the branch cuts in the radial function, which also lead to non-trivial dependence of the frequencies on ε (where $\arg(\omega)+\arg(r) = -\Pi/2$ and $\varepsilon < 1$): for $n < 4$ $\omega_n = \pm|\Re(\omega_n)|+\Im(\omega_n)i$); for $n > 4$ $\omega_n(\varepsilon) = -\mathrm{sgn}(\varepsilon)|\Re(\omega_n)|+\Im(\omega_n)i$ and for $n = 8$, $|\varepsilon| < 0.75$, $\omega_{n=8} = \mathrm{sgn}(\varepsilon)\, 0.030649006 + 3.996823690i$.

Because of this, the value for $n = 8$ in the table A.3 was obtained for *positive* ε ($\varepsilon = 0.3$), unlike the other modes with $n \geq 5$, which were obtained for $\varepsilon = -0.3$.

The applicability of the second equation in the system Eqs.(A.2), F_2, may depend on the parameter ε, so the behavior of the solutions of Eqs.(A.2) under the variation of ε is still an open problem studied here for the first time. The frequencies presented here are stable with precision of 6 digits at the worst and usually around 9 digits with respect to a change of ε in the corresponding intervals.

A.4.2 Second example: Rotating black holes

A more complicated system to solve can be found in the case of QNMs from rotating black holes. The two-dimensional Müller algorithm was applied successfully in this case too and the complete results can be found in [133]. Here, one can find some details on the numerical procedures used in this case.

To find the QNMs of a rotating black hole, one uses the exact solutions of the Teukolsky radial and angular equations, describing the linearized electromagnetic perturbations of the Kerr metric, in terms of confluent Heun functions, as stated for the first time in full detail in [62]. From [67], for the values of the parameters: s=-1, M=1/2, $|r| = 110$, m=0, a=0.01, $\theta = \pi/3$, one obtains:

$$F_1(x,y) = \mathrm{HeunC}(-1.9996ix, 2.0002ix+1.0000, 0.0002ix-1.0000, -1.9996x(i+x), 1.9995x^2-y +0.5000+1.9998ix, -110.02e^{(4.7124i-iarg(x))}+1.0000).(110.00e^{(4.7124i-iarg(x))})^{(2.00+0.0002ix)} = 0$$

$$F_2(x,y) = \frac{\mathrm{HeunC}'(0.04x, -1.00, 1.00, -0.04x, 0.50-1.00y+0.02x-0.0001x^2, 0.25)}{\mathrm{HeunC}(0.04x, -1.00, 1.00, -0.04x, 0.50-1.00y+0.02x-0.0001x^2, 0.25)} + \frac{\mathrm{HeunC}'(-0.04x, 1.00, -1.00, 0.04x, 0.50-1.00y-0.02x-0.0001x^2, 0.75)}{\mathrm{HeunC}(-0.04x, 1.00, -1.00, 0.04x, 0.50-y-0.02x-0.0001x^2, 0.75)} = 0$$

where HeunC' is the derivative of the confluent Heun function ([106]) as defined in MAPLE.

For brevity, here the radial equation $F_1(x, y)$ was rounded to only 4 digits of significance. In our numerical experiments, we used the complete system with software floating-point number set to 64, where the derivatives of the confluent Heun functions HeunC$'$ were replaced with the associate δ_N confluent Heun function according to equation (3.7) of [104]. This was done to avoid the numerical evaluation HeunC$'$ so that the peculiarities of the numerical implementation of the confluent

Heun function (i.e. the use of MAPLE *fdiff* procedure) are minimized. The difference in the times needed to fix a root when HeunC$'$ is used and when it is not used is small for the modes (i.e.x) with small imaginary part ($\Delta t \sim 15s$), but it increases with the mode number, until it becomes significant for modes with big imaginary part (for the 10^{th} mode – $R = 3$ in table A.4 – the difference is already $\Delta t \sim 100s$). This slowdown is due to the time-consuming numerical integration in the complex domain, needed for the evaluation of HeunC$'$.

R	$(x)^{initial}$ $(y)^{initial}$	$(x)^{final}$ $(y)^{final}$	$t_{Broyden}$[s] $N_{Broyden}$	t_{M2}[s] N_{M2}	t_{M1}[s] N_{M1}
1	$0.49 + 0.18i$ $2.001 + 0.1i$	0.4965436315+0.1849695292i 1.9999915063–0.7347653.$10^{-5}i$	208 23	102 9(5)*	92 11(4)*
2	$0.17 + 0.97i$ $2.001 + 0.1i$	0.3495869222+1.0503235984i 2.0000392386 − 0.2937407.$10^{-4}i$	449 34	229 12(5)*	244 15(5)*
3	$0.07 + 5.147i$ 2.001+0.051i	0.0608496029+5.1191008697i 2.0010479243–0.2491318.$10^{-4}i$	868 36	568 11(5)*	489 17(5)*

Table A.4: QNMs of Kerr BH for $s = -1$. R numbers the root, t and N label the time and the iterations needed for the algorithms to exit. * denotes the roots dependent on the order of the equations in M1 and M2.

For that system, three pairs of starting points were used:$(0.49 + 0.18i, 2.001 + 0.1i)$, $(0.17 + 0.97i, 2.001 + 0.1i)$, $(0.069 + 5.146i, 2.001 + 0.051i)$. The results can be found in table A.4. One sees that the two modifications of the two-dimensional Müller algorithm M1 and M2 are much quicker than the Broyden algorithm ($t_{M1} \sim t_{M2} < t_B$). Newton's method cannot be used.

The supremacy of the Müller algorithms is clear and it is not isolated – it is observed for other modes or values of the parameters (for example, for $m = 1$). To check the precision of the method, the first two modes were compared with the already published results of electromagnetic QNMs of a Kerr black hole (see [94]) and were found to coincide with at least 9 digits of significance with them. We could not find a published value for the third mode.

This example show that the two-dimensional Müller method is much better suited for solving systems involving the Heun functions than the already known algorithms.

A.5 Conclusion

We presented the general idea of a method for solving a system of two complex-valued nonlinear transcendental equations with complex roots based on the one-dimensional Müller method. The new method is aimed to provide adequate way to deal with systems featuring Heun functions, which cannot be solved efficiently by the known root-finding methods. Tests on such systems from the QNM physics proved that in those cases, the new method indeed work better than the other methods (For examples including elementary functions and simple special functions see [128].). The complete mathematical investigation of the proposed new method,

and especially its theoretical order of convergence under proper conditions on the class of functions F_1, F_2 is still an open problem.

With the two-dimensional Müller algorithm one can find the roots of the Regge-Wheeler equation [62], the Zerilli equation [66], the Teukolsky radial and angular equations [67], all of which are solved analytically in terms of confluent Heun functions. Using this algorithm, we were able to solve *directly* the problem of quasi-normal modes of a Schwarzschild and Kerr black hole with higher precision than that of the Broyden method. The so found solutions agree to great extent with previous published numerical results thus confirming the usefulness of the method.

The method has already been used independently, see the recent references [141, 142].

Bibliography

[1] R. Mundt, C. M. Hamilton, W. Herbst, C. M. Johns-Krull, and J. Winn, "Bipolar jets produced by a spectroscopic binary," *ApJ* **708** (2010) L5, arXiv:0912.1740 [astro-ph.SR]. (Cited on page 1.)

[2] M. Livio, "Astrophysical Jets," *Baltic Astronomy* **13** (2004) 273–279. (Cited on page 1.)

[3] F. Collaboration, G. Ghisellini, L. Maraschi, and F. Tavecchio, "Radio-Loud Narrow-Line Seyfert 1 as a New Class of Gamma-Ray AGN," *Astrophys.J.* **707** (2009) L 142–L147, arXiv:0911.3485 [astro-ph.HE]. (Cited on page 1.)

[4] P. Mészáros, "Gamma-Ray Bursts: Accumulating Afterglow Implications, Progenitor Clues, and Prospects," *Science* **291** (2001) 79–84, astro-ph/0102255. (Cited on page 1.)

[5] B. Zhang and P. Mészáros, "Gamma-Ray Bursts with Continuous Energy Injection and Their Afterglow Signature," *ApJ* **566** (2002) 712–722, astro-ph/0108402. (Cited on page 1.)

[6] D. N. Burrows, P. Romano, A. Falcone, *et al.*, "Bright X-ray Flares in Gamma-Ray Burst Afterglows," *Science* **309** (2005) 1833–1835, astro-ph/0506130. (Cited on page 1.)

[7] L. A. Antonelli, P. D. Avanzo, R. Perna, *et al.*, "GRB090426: the farthest short gamma-ray burst?," *A&A* **507** (2009) 3:.L45–L48, arXiv:0911.0046 [astro-ph.HE]. (Cited on page 1.)

[8] Nysewander, M. and Fruchter, A. S. and Pe´er, A. , "A Comparison of the Afterglows of Short- and Long-Duration Gamma-Ray Bursts," *ApJ* **701** (2009) 824–836, arXiv:0806.3607 [astro-ph]. (Cited on pages 1 and 4.)

[9] A. Shahmoradi and R. Nemiroff, "Hardness as a Spectral Peak Estimator for Gamma-Ray Bursts," *MNRAS* **407** (2010) I.4:2075–2090, arXiv:0912.2148 [astro-ph.HE]. (Cited on page 1.)

[10] H. Lv, E. Liang, B. Zhang, and B. Zhang, "A New Classification Method for Gamma-Ray Bursts," *ApJ* **725** (2010) 1965–1970, arXiv:1001.0598 [astro-ph.HE]. (Cited on pages 1 and 4.)

[11] LIGO Scientific Collaboration and Virgo Collaboration, "Search for gravitational-wave inspiral signals associated with short Gamma-Ray Bursts during LIGO's fifth and Virgo's first science run," *ApJ* **715** (2010) 1453, arXiv:1001.0165 [astro-ph.HE]. (Cited on page 1.)

[12] LIGO Scientific Collaboration and K. Hurley, "Implications for the Origin of GRB 070201 from LIGO Observation," *ApJ* **681** (2008) 1419–1428, arXiv:0711.1163 [astro-ph.HE]. (Cited on page 1.)

[13] T. Piran, "Gamma-Ray Bursts and the Fireball Model," *Physics Reports* **314** (1999) 575–667, astro-ph/9810256. (Cited on page 2.)

[14] M. Lyutikov, "Gamma Ray Bursts: back to the blackboard," in *proceedings of the The Shocking Universe meeting, Venice, September 2009*. 2009. arXiv:0911.0349 [astro-ph.HE]. (Cited on page 2.)

[15] A. Maxham and B. Zhang, "Modeling Gamma-Ray Burst X-Ray Flares within the Internal Shock Model," *ApJ* **707** (2009) 1623, arXiv:0911.0707 [astro-ph.HE]. (Cited on page 2.)

[16] J. Granot, "Structure & Dynamics of GRB Jets," *Talk given at the Conference 'Challenges in Relativistic Jets', Cracow, Poland, June 27, 2006,* (2006) . http://www.oa.uj.edu.pl/2006jets/talks.html. (Cited on page 2.)

[17] R. Shen, P. Kumar, and T. Piran, "The late jet in gamma-ray bursts and its interactions with a supernova ejecta and a cocoon," *MNRAS* **403** (2010) I.1:229â245, arXiv:0910.5727 [astro-ph.HE]. (Cited on page 2.)

[18] R. Willingale, F. Genet, J. Granot, and P. T. O'Brien, "The spectral-temporal properties of the prompt pulses and rapid decay phase of GRBs," *MNRAS* **403** I.3:1296â1316, arXiv:0912.1759. (Cited on page 2.)

[19] Y.-Z. Fan, "The spectrum of γ-ray Burst: a clue," *MNRAS* **403** (2010) I.1:483â490, arXiv:0912.1884 [astro-ph.CO]. (Cited on page 2.)

[20] J. Wheeler, "Study Week on Nuclei of Galaxies," in *Proceedings of a Study Week on Nuclei of Galaxies, held in Rome, April 13-18, 1970*, D. J. K. O'Connell, ed., vol. 35, p. 539. American Elsevier, 1971. (Cited on pages 2 and 76.)

[21] W. H. Press and S. A. Teukolsky, "Floating Orbits, Superradiant Scattering and the Black-hole Bomb," *Nature* **238** (1972) I.5361:211–212. (Cited on page 2.)

[22] R. D. Blandford and R. L. Znajek, "Electromagnetic extraction of energy from Kerr black holes," *MNRAS* **179** (1977) 433. (Cited on page 2.)

[23] R. D. Blandford, "Black Holes and Relativistic Jets," *Progress of Theoretical Physics Supplement* **143** (2001) 182–201, astro-ph/0110394. (Cited on page 2.)

[24] R. Wald, "Energy Limits on the Penrose Process," *ApJ* **191** (1974) 231–233. (Cited on pages 2 and 76.)

[25] J. Bardeen, W. H. Press, and S. A. Teukolsky, "Rotating Black Holes: Locally Nonrotating Frames, Energy Extraction, and Scalar Synchrotron Radiation," *ApJ* **178** (1972) 347–370. (Cited on pages 2 and 3.)

[26] R. da Silva de Souza and R. Opher, "Origin of $10^{15} - 10^{16}$ G Magnetic Fields in the Central Engine of Gamma Ray Bursts," *JCAP* **02** (2010) 022, arXiv:0910.5258 [astro-ph.HE]. (Cited on page 2.)

[27] S. Nagataki, "Development of General Relativistic Magnetohydrodynamic Code and its Application to Central Engine of Long Gamma-Ray Bursts," *ApJ* **704** (2009) 937–950, arXiv:0902.1908 [astro-ph.HE]. (Cited on page 2.)

[28] H. K. Lee, R. A. M. J. Wijers, and G. E. Brown, "Blandford-Znajek process as a gamma ray burst central engine," in *ASP Conference Series*, J. Poutanen and R. Svensson, eds. (Cited on page 2.)

[29] M. V. Barkov and S. S. Komissarov, "Central engines of Gamma Ray Bursts. Magnetic mechanism in the collapsar model," in *HIGH ENERGY GAMMA-RAY ASTRONOMY: Proceedings of the 4th International Meeting on High Energy Gamma-Ray Astronomy*, vol. 1085 of *AIP Conference Proceedings*, pp. 608–611. 2008. arXiv:0809.1402 [astro-ph]. (Cited on page 2.)

[30] M. V. Barkov and S. S. Komissarov, "Close Binary Progenitors of Long Gamma Ray Bursts," *MNRAS* **401** (2010) I.3:1644–1656, arXiv:0908.0695 [astro-ph.HE]. (Cited on page 2.)

[31] W.-H. Lei, D.-X. Wang, Y.-C. Zou, and L. Zhang, "Hyperaccretion after the Blandford-Znajek Process: a New Model for GRBs with X-Ray Flares Observed in Early Afterglows," *Chin. J. Astron. Astrophys.* **8** (2008) 404–410, arXiv:0802.0419 [astro-ph]. (Cited on page 2.)

[32] J. H. Krolik and J. Hawley, *General Relativistic MHD Jets*, vol. 794, pp. 265–287. Springer-Verlag Berlin Heidelberg,ISBN 978-3-540-76936-1, 2010. arXiv:0909.2580 [astro-ph.HE]. (Cited on page 2.)

[33] S. S. Komissarov and M. V. Barkov, "Activation of the Blandford-Znajek mechanism in collapsing stars," *MNRAS* **397** (2009) I.3:1153â1168, arXiv:0902.2881 [astro-ph.HE]. (Cited on page 2.)

[34] A. Köenigl, "Jet Launching - General Review," *Talk given at the Conference 'Challenges in Relativistic Jets', Cracow, Poland, June 27, 2006* (2006) . http://www.oa.uj.edu.pl/2006jets/talks.html. (Cited on page 3.)

[35] P. P. Fiziev, "Classes of Exact Solutions to Regge-Wheeler and Teukolsky Equations," (2009) , arXiv:0902.1277 [gr-qc]. (Cited on pages 3, 13, 15, 26, 62 and 63.)

[36] P. P. Fiziev, "To the theory of astrophysical relativistic jets," *to be published* (2010) . (Cited on pages 3 and 79.)

[37] S. Detweiler, "Black holes and gravitational waves. III - The resonant frequencies of rotating holes," *ApJ* **239** (1980) 292–295. (Cited on pages 3 and 29.)

[38] O. Dreyer, B. Kelly, B. Krishnan, L. S. Finn, D. Garrison, and R. Lopez-Aleman, "Black-hole spectroscopy: testing general relativity through gravitational-wave observations," *Class. Quantum Grav.* **21** (2004) 787â803. gr-qc/0309007. (Cited on page 3.)

[39] P. P. Fiziev, "On the Exact Solutions of the Regge-Wheeler Equation in the Schwarzschild Black Hole Interior," *Class. Quant. Grav.* **23** (2006) 2447–2468, gr-qc/0603003. (Cited on pages 3, 68 and 71.)

[40] C. B. M. H. Chirenti and L. Rezzolla, "How to tell a gravastar from black hole," *Class. Quant. Grav.* **24** (2007) 4191–4206, arXiv:0706.1513 [gr-qc]. (Cited on pages 3, 5 and 29.)

[41] C. B. M. H. Chirenti and L. Rezzolla, "Ergoregion instability in rotating gravastars," *Phys.Rev.D* **78** (2008) 084011, arXiv:0808.4080 [gr-qc]. (Cited on pages 3, 5 and 29.)

[42] S. A. Teukolsky, "Perturbations of a rotating black hole I Fundamental Equations for Gravitational, Electromagnetic and Neutrino-field Perturbations," *ApJ* **185** (1973) 635–648. (Cited on pages 3, 19, 20, 21, 23, 25 and 76.)

[43] S. Chandrasekhar, *The mathematical theory of black holes*. (Cited on pages 3, 7, 29, 50, 51 and 67.)

[44] S. A. Teukolsky and W. H. Press, "Perturbations of a rotating black hole. III - Interaction of the hole with gravitational and electromagnetic radiation," *ApJ* **193** (1974) 443. (Cited on page 3.)

[45] E. W. Leaver, "An analytic representation for the quasi-normal modes of Kerr black holes," *Proc. Roy. Soc. London A* **402** (1985) 285–298. (Cited on pages 3, 7, 29, 33, 38 and 99.)

[46] T. Regge and J. A. Wheeler, "Stability of a Schwarzschild Singularity," *Phys.Rev* **108** (1957) 1063–1069. (Cited on page 3.)

[47] F. J. Zerilli, "Effective Potential for Even-Parity Regge-Wheeler Gravitational Perturbation Equations," *Phys.Rev. Lett.* **24** (1970) 737–738. (Cited on page 3.)

[48] C. V. Vishveshwara, "Stability of the Schwarzschild Metric," *Phys.Rev. D* **1** (1970) 2870–2879. (Cited on page 3.)

[49] S. A. Teukolsky, "Rotating Black Holes: Separable Wave Equations for Gravitational and Electromagnetic Perturbations," *Phys.Rev.Lett.* **29** (1972) 1114–1118. (Cited on pages 3 and 20.)

[50] W. Press and S. A. Teukolsky, "Perturbations of a Rotating Black Hole. II. Dynamical Stability of the Kerr Metric," *ApJ* **185** (1973) 649–674. (Cited on pages 3 and 20.)

[51] S. A. Teukolsky and W. H. Press, "Perturbations of a rotating black hole. III – Interaction of the hole with gravitational and electromagnetic radiation," *ApJ* **193** (1974) 443. (Cited on pages 3, 6, 20, 29, 39, 67 and 77.)

[52] S. Chandrasekhar, "On the Equations Governing the Perturbations of the Schwarzschild Black Hole," *Proc. Roy. Soc. London A* **343** (1975) 289–298. (Cited on page 3.)

[53] S. Chandrasekhar and S. L. Detweiler, "The quasi-normal modes of the Schwarzschild black hole," *Proc. Roy. Soc. London A* **344** (1975) 441–452. (Cited on pages 3, 7, 29 and 33.)

[54] S. Chandrasekhar, "On a transformation of Teukolsky's equation and the electromagnetic perturbations of Kerr black hole," *Proc. R. Soc. Lond. A* **348** (1976) 39–55. (Cited on page 3.)

[55] S. Detweiler, "On the equations governing the electromagnetic perturbations of the Kerr black hole," *Proc. R. Soc. London A* **349** (1976) 217–230. (Cited on page 3.)

[56] S. Chandrasekhar, "On the equations governing the perturbations of Reissner-Nordström black hole," *Proc. R. Soc. London A* **3365** (1976) 453–465. (Cited on page 3.)

[57] E. W. Leaver, "Solutions to a generalized spheroidal wave equation: Teukolsky's equations in general relativity, and the two-center problem in molecular quantum mechanics," *J.Math. Phys.* **27** (1986) 5:1238. (Cited on pages 3, 7 and 38.)

[58] N. Andersson, "A numerically accurate investigation of black-hole normal modes," *Proc. Roy. Soc. London A* **439, no.1905** (1992) 47–58. (Cited on pages 3, 7, 33, 88 and 99.)

[59] E. Berti, V. Cardoso, K. D. Kokkotas, and H. Onozawa, "Highly damped quasinormal modes of Kerr black holes," *Phys.Rev. D* **68** (2003) 124018, `hep-th/0307013`. (Cited on pages 3, 5, 47, 51, 53, 78 and 79.)

[60] E. Berti, "Black hole quasinormal modes: hints of quantum gravity?," in *the Proceedings of the Workshop on 'Dynamics and Thermodynamics of Black Holes and Naked Singularities'*. 2004. `gr-qc/0411025v1`. (Cited on pages 3, 7, 29, 33, 35 and 52.)

[61] S. Hod and U. Keshet, "Intermediate Asymptotics of the Kerr Quasinormal Spectrum," *Class.Quant.Grav.* **22** (2005) L71–L76, gr-qc/0505112. (Cited on pages 3 and 48.)

[62] P. P. Fiziev, "Exact Solutions of Regge-Wheeler Equation and Quasi-Normal Modes of Compact Objects," *Class. Quant. Grav.* **23** (2006) 2447–2468. arXiv:0509123v5[gr-qc]. (Cited on pages 3, 7, 8, 28, 29, 31, 34, 41, 88, 89, 98, 99, 100 and 102.)

[63] V. Ferrari and L. Gualtieri, "Quasi-normal modes and gravitational wave astronomy," *Gen.Rel.Grav.* **40** (2008) 945–970, arXiv:0709.0657 [gr-qc]. (Cited on pages 3, 7, 29 and 77.)

[64] S. Hod, "Slow relaxation of rapidly rotating black holes," *Phys.Rev.D* **78** (2008) 084035, arXiv:0811.3806 [gr-qc]. (Cited on pages 3 and 48.)

[65] E. Berti, V. Cardoso, and A. O. Starinets, "Quasinormal modes of black holes and black branes," *Class. Quantum Grav.* **26** (2009) 163001, 108pp, arXiv:0905.2975 [gr-qc]. (Cited on pages 3, 5, 7, 29, 33 and 44.)

[66] P. P. Fiziev, "Teukolsky-Starobinsky identities: A novel derivation and generalizations," *Phys. Rev. D* **80** (2009) , arXiv:0906.5108 [gr-qc]. (Cited on pages 3, 7, 26, 28, 29, 30, 62 and 102.)

[67] P. P. Fiziev, "Classes of exact solutions to the Teukolsky master equation," *Class. Quantum Grav.* **27** (2010) 135001, arXiv:0908.4234 [gr-qc]. (Cited on pages 3, 7, 13, 25, 26, 28, 29, 30, 39, 40, 41, 62, 63, 64, 67, 71, 77, 79, 100 and 102.)

[68] S. Hod and O. Hod, "Analytic treatment of the black-hole bomb," *Phys. Rev. D, Rapid communication* **81** (2010) 061502, arXiv:0910.0734 [gr-qc]. (Cited on pages 3 and 6.)

[69] R. A. Konoplya and A. Zhidenko, "Quasinormal modes of black holes: from astrophysics to string theory," *Reviews of Modern Physics* **83, Issue 3** (2011) 793–836, arXiv:1102.4014 [gr-qc]. (Cited on pages 3, 7 and 29.)

[70] S. Hod, "Quasinormal resonances of a massive scalar field in a near-extremal Kerr black hole spacetime," *Physical Review D* **84** (2011) 044046, arXiv:1109.4080 [gr-qc]. (Cited on pages 3 and 6.)

[71] J. D. Schnittman, "Electromagnetic counterparts to black hole mergers," *Classical and Quantum Gravity* **28** (2011) 094021, arXiv:1010.3250 [astro-ph.HE]. (Cited on pages 4 and 5.)

[72] B. P. Abbott, others, and LIGO scientific collaboration, "Directional limits on persistent gravitational waves using LIGO S5 science data," (2011) , arXiv:1109.1809 [astro-ph.CO]. (Cited on page 4.)

[73] The LIGO Scientific Collaboration and the Virgo Collaboration, "Search for gravitational waves from binary black hole inspiral, merger and ringdown," *Phys.Rev.D* **83** (2011) 122005, arXiv:1102.3781 [gr-qc]. (Cited on page 4.)

[74] The LIGO Scientific Collaboration, J. Abadie, *et al.*, "Search for Gravitational Wave Bursts from Six Magnetars," *Astrophys.J.* **734** (2011) L35, arXiv:1011.4079 [astro-ph.HE]. (Cited on page 4.)

[75] The LIGO Scientific Collaboration, "A search for gravitational waves associated with the August 2006 timing glitch of the Vela pulsar," *Phys.Rev.D* **83** (2011) 042001,069902, arXiv:1011.1357 [gr-qc]. (Cited on page 4.)

[76] LIGO Scientific Collaboration, "First search for gravitational waves from the youngest known neutron star," *Astrophys.J.* **722** (2010) 1504, arXiv:1006.2535 [gr-qc]. (Cited on page 4.)

[77] the LIGO Scientific Collaboration and the Virgo Collaboration, "Search for Gravitational Waves from Compact Binary Coalescence in LIGO and Virgo Data from S5 and VSR1," *Phys.Rev.D* **82** 102001, arXiv:1005.4655 [gr-qc]. (Cited on page 4.)

[78] the LIGO Scientific Collaboration and the Virgo Collaboration, "All-sky search for gravitational-wave bursts in the first joint LIGO-GEO-Virgo run," *Phys.Rev.D* **81** (2010) 102001, arXiv:1002.1036 [gr-qc]. (Cited on page 4.)

[79] A. Dietz, LIGO Scientific Collaboration, and the Virgo Collaboration, "Searches for inspiral gravitational waves associated with short gamma-ray bursts in LIGO's fifth and Virgo's first science run," (2010) , arXiv:1006.3393 [gr-qc]. (Cited on page 4.)

[80] the LIGO Scientific Collaboration and the Virgo Collaboration, "Search for gravitational-wave bursts associated with gamma-ray bursts using data from LIGO Science Run 5 and Virgo Science Run 1," *Astrophysical Journal* **715** (2010) 1438–1452, arXiv:0908.3824 [astro-ph.HE]. (Cited on page 4.)

[81] D. M. Coward, B. Gendre, P. J. Sutton, E. J. Howell, T. Regimbau, M. Laas-Bourez, A. Klotz, M. Boer, and M. Branchesi, "Toward an optimal search strategy of optical and gravitational wave emissions from binary neutron star coalescence," *MNRAS* **415** (2011) L26, arXiv:1104.5552 [astro-ph.HE]. (Cited on page 5.)

[82] T. Bogdanovic, T. Bode, R. Haas, P. Laguna, and D. Shoemaker, "Properties of Accretion Flows Around Coalescing Supermassive Black Holes," *Classical and Quantum Gravity* **28** (2011) 094020, arXiv:1010.2496 [astro-ph.CO]. (Cited on page 5.)

[83] P. Moesta, D. Alic, L. Rezzolla, O. Zanotti, and C. Palenz, "On the detectability of dual jets from binary black holes," (2011) , arXiv:1109.1177 [gr-qc]. (Cited on page 5.)

[84] L. Rezzolla, B. Giacomazzo, L. Baiotti, J. Granot, C. Kouveliotou, and M. A. Aloy, "The missing link: Merging neutron stars naturally produce jet-like structures and can power short Gamma-Ray Bursts," *Astrophys. J. Lett.* **732** (2011) L6, arXiv:1101.4298 [astro-ph.HE]. (Cited on page 5.)

[85] the LIGO Scientific Collaboration and the Virgo Collaboration, "Implementation and testing of the first prompt search for electromagnetic counterparts to gravitational wave transients," (2011) , arXiv:1109.3498 [astro-ph.IM]. (Cited on page 5.)

[86] N. L. Christensen, the LIGO Scientific Collaboration, and the Virgo Collaboration, "Multimessenger Astronomy," (2011) , arXiv:1105.5843 [gr-qc]. (Cited on page 5.)

[87] J. L. Jaramillo, R. P. Macedo, P. Moesta, and L. Rezzolla, "Black-hole horizons as probes of black-hole dynamics I: post-merger recoil in head-on collisions," *Submitted to PRD* (2011) , arXiv:1108.0060 [gr-qc]. (Cited on page 5.)

[88] L. Rezzolla, R. P. Macedo, and J. L. Jaramillo, "Understanding the anti-kick in the merger of binary black holes," *Phys.Rev.Lett.* **104** (2010) 221101, arXiv:1003.0873 [gr-qc]. (Cited on page 5.)

[89] P. Anninos, D. Hobill, E. Seidel, L. Smarr, and W.-M. Suen, "The Collision of Two Black Holes," *Phys.Rev.Lett.* **71** (1993) 2851–2854, gr-qc/9309016. (Cited on page 5.)

[90] A. Buonanno, G. B. Cook, and F. Pretorius, "Inspiral, merger and ring-down of equal-mass black-hole binaries," *Phys.Rev.D* **75** (2007) 124018, gr-qc/0610122v2. (Cited on page 5.)

[91] J. D. Schnittman, A. Buonanno, J. R. van Meter, J. G. Baker, W. D. Boggs, J. Centrella, B. J. Kelly, and S. T. McWilliams, "Anatomy of the binary black hole recoil: A multipolar analysis," *Phys.Rev.D* **77** (2008) 044031, arXiv:0707.0301 [gr-qc]. (Cited on page 5.)

[92] M. Shibata and K. Taniguchi, "Merger of black hole and neutron star in general relativity: Tidal disruption, torus mass, and gravitational waves," *Phys.Rev.D* **77** (2008) 084015, arXiv:0711.1410 [gr-qc]. (Cited on page 5.)

[93] C. O. Lousto, H. Nakano, Y. Zlochower, and M. Campanelli, "Intermediate-mass-ratio black hole binaries: intertwining numerical and

perturbative techniques," *Phys.Rev.D* **82** (2010) 104057, arXiv:1008.4360 [gr-qc]. (Cited on page 5.)

[94] E. Berti, V. Cardoso, and C. M. Will, "On gravitational-wave spectroscopy of massive black holes with the space interferometer LISA," *Phys.Rev.D* **73** (2006) 064030, arXiv:0512160 [gr-qc]. (Cited on pages 5, 29, 44, 88 and 101.)

[95] B. F. Schutz, J. Centrella, C. Cutler, and S. A. Hughes, "Will Einstein Have the Last Word on Gravity?," *Astro2010: The Astronomy and Astrophysics Decadal Survey* **265** (2009) , arXiv:0903.0100 [gr-qc]. (Cited on pages 5 and 29.)

[96] P. Pani, E. Berti, V. Cardoso, Y. Chen, and R. Norte, "Gravitational wave signatures of the absence of an event horizon: Nonradial oscillations of a thin-shell gravastar," *Phys.Rev.D* **80** (2009) 124047, arXiv:0909.0287 [gr-qc]. (Cited on pages 5 and 29.)

[97] D. Staicova and P. Fiziev, "The Spectrum of Electromagnetic Jets from Kerr Black Holes and Naked Singularities in the Teukolsky Perturbation Theory," *Astrophys Space Sci.* **332** (2011) 385–401, arXiv:1002.0480 [astro-ph.HE]. (Cited on pages 5, 7, 29, 30, 40, 46, 62 and 89.)

[98] M. Lyutikov and J. C. McKinney, "Slowly balding black holes," *Phys. Rev. D* **84** (2011) 084019, arXiv:1109.0584 [astro-ph.HE]. (Cited on page 5.)

[99] H. Gao, B.-B. Zhang, and B. Zhang, "Evidence Of Superposed Variability Components In GRB Prompt Emission Lightcurves," (2011) , arXiv:1103.0074 [astro-ph.HE]. (Cited on page 6.)

[100] B. Zhang, "Open Questions in GRB Physics," *Comptes Rendus Physique* **12** (2011) 206–225, arXiv:1104.0932 [astro-ph.HE]. (Cited on page 6.)

[101] W.-H. Lei and B. Zhang, "Black hole Spin in Sw J1644+57 and Sw J2058+05," *ApJ* **L27** (2011) 740, arXiv:1108.3115 [astro-ph.HE]. (Cited on page 6.)

[102] J. E. McClintock, R. Narayan, S. Davis, L. Gou, A. Kulkarni, J. Orosz, R. Penna, R. Remillard, and J. Steiner, "Measuring the Spins of Accreting Black Holes," *To appear in Classical and Quantum Gravity; Special volume for GR19, eds. D. Marolf and D. Sudarsky* (2011) , arXiv:1101.0811 [astro-ph.HE]. (Cited on page 6.)

[103] L. Brenneman and C. Reynolds, "Constraining Black Hole Spin Via X-ray Spectroscopy," *Astrophys.J.* **652** (2006) 1028–1043, astro-ph/0608502. (Cited on page 6.)

[104] P. P. Fiziev, "Novel relations and new properties of confluent Heun's functions and their derivatives of arbitrary order," *J. Phys. A: Math. Theor.* **43** (2010) 035203, arXiv:0904.0245 [math-ph]. (Cited on pages 7, 12, 13, 15, 16, 29 and 100.)

[105] S. Y. Slavyanov and W. Lay, *Special Functions, A Unified Theory Based on Singularities*. Oxford: Oxford Mathematical Monographs, 2000. (Cited on pages 7, 11, 12, 13, 15, 40, 41 and 67.)

[106] K. Heun, "Zur Theorie der Riemann'schen Functionen zweiter Ordnung mit vier Verzweigungspunkten," *Math. Ann.* **33** . (Cited on pages 7, 11, 13, 98 and 100.)

[107] A. Decarreau, M. C. Dumont-Lepage, P. Maroni, A. Robert, and A. Roneaux, "Formes canoniques des equations confluentes de 1'equation de Heun," *Ann. Soc. Bruxelles* **92** 53–78. (Cited on pages 7, 11, 13, 15 and 38.)

[108] A. Decarreau, P. Maroni, and A. Robert, "Heun's Differential Equations," *1978 Ann. Soc. Buxelles* **92** 151. (Cited on pages 7, 11, 12, 13, 14 and 15.)

[109] P. Fiziev and D. Staicova, "Solving systems of transcendental equations involving the Heun functions.," (2012) , arXiv:1201.0017 [cs.NA]. (Cited on pages 7, 38, 42, 43 and 45.)

[110] P. Fiziev and D. Staicova, "Application of the confluent Heun functions for finding the QNMs of non-rotating black holes," *Phys. Rev. D* **84** (2011) 127502, arXiv:1109.1532 [gr-qc]. (Cited on pages 7, 42, 43, 52 and 98.)

[111] F. W. J. Olver, D. W. Lozier, R. F. Boisvert, and C. W. Clark, eds., *NIST Handbook of Mathematical Functions*. Cambridge University Press, ISBN: 978-05211-922-55,, 2010. http://dlmf.nist.gov/31.17. (Cited on page 11.)

[112] M. Hortacsu, "Heun Functions and their uses in Physics," arXiv:1101.0471 [math-ph]. (Cited on page 12.)

[113] R. P. Kerr, "Gravitational field of a spinning mass as an example of algebraically special metric," *Phys.Rev.Lett.* **11** (1963) 237. (Cited on page 17.)

[114] J. B. Hartle and K. Thorne, "Slowly rotating relativistic stars. II. Models for neutron stars and supermassive stars," *Astrophys. J.* **153** (1968) 807. (Cited on page 17.)

[115] M. Bradley and G. Fodor, "The quadrupole moment of slowly rotating stars," *Journal of Physics: Conference Series* **229** (2010) 012025. http://iopscience.iop.org/1742-6596/229/1/012025/pdf/1742-6596_229_1_012025.pdf. (Cited on page 17.)

[116] C. Cadeau, S. Morsink, D. Leahy, and S. Campbell1, "Light curves for rapidly rotating neutron stars," *The Astrophysical Journal* **654** (2007) 458:469. http://iopscience.iop.org/0004-637X/654/1/458/pdf/65132.web.pdf. (Cited on page 17.)

[117] D. ed Wiltshire, M. Visser, and S. Scott, eds., *The Kerr Spacetime: Rotating black holes in general relativity*. Cambridge University Press, 2009. (Cited on page 19.)

[118] E. Fackerell and J. Ipser, "Weak Electromagnetic Fields Around a Rotating Black Hole," *Phys. Rev. D* **5** (1972) 2455. http://adsabs.harvard.edu/abs/1972PhRvD...5.2455F. (Cited on page 20.)

[119] R. Wald, "On perturbations of a Kerr black hole," *J. Math. Phys.* **14** (1973) 1453. http://jmp.aip.org/resource/1/jmapaq/v14/i10/p1453_s1. (Cited on page 20.)

[120] E. Newman and R. Penrose, "An Approach to Gravitational Radiation by a Method of Spin Coefficients," *J.Math.Phys.* **3** (1962) 566. http://jmp.aip.org/resource/1/jmapaq/v3/i3/p566_s1. (Cited on pages 20 and 21.)

[121] A. Petrov, "Classification of spaces defined by gravitational fields," *Uch. Zapiski Kazan Gos. Univ.* **114(8)** (1954) 55–69. (Cited on page 21.)

[122] W. Kinnersley, "Type D Vacuum Metrics," *J.Math.Phys.* **10** (1969) 1195. http://jmp.aip.org/resource/1/jmapaq/v10/i7/p1195_s1. (Cited on page 23.)

[123] E. Ching, P. Leung, W. Suen, and K. Young, "Wave Propagation in Gravitational Systems: Completeness of Quasinormal Modes," *Phys.Rev.D* **54** (1996) 3778–3791, gr-qc/9507034. (Cited on page 25.)

[124] R. Price and V. Husain, "A Model for the completeness of quasinormal modes of relativistic stellar oscillations," *Phys. Rev. Lett.* **68** (1992) 1973. http://prl.aps.org/abstract/PRL/v68/i13/p1973_1. (Cited on page 25.)

[125] P. P. Fiziev and D. R. Staicova, "A new model of the Central Engine of GRB and the Cosmic Jets," *Bulgarian Astronomical Journal* **11** (2009) 3, arXiv:0902.2408 [atro-ph.HE]. (Cited on pages 26, 62, 63 and 68.)

[126] P. P. Fiziev and D. R. Staicova, "Toward a New Model of the Central Engine of GRB," *Bulgarian Astronomical Journal* **11** 13, arXiv:0902.2411. (Cited on pages 26, 62 and 68.)

[127] R. S. Borissov and P. P. Fiziev, "Exact Solutions of Teukolsky Master Equation with Continuous Spectrum," *Bulg. J. Phys.* **37** (2010) 2:065–089, arXiv:0903.3617 [gr-qc]. (Cited on page 26.)

[128] P. Fiziev and D. Staicova, "Two-dimensional generalization of the Muller root-finding algorithm and its applications," (2010) , arXiv:1005.5375 [cs.NA]. (Cited on pages 33, 38, 43, 93, 98 and 101.)

[129] A. Maassen van den Brink, "Analytic treatment of black-hole gravitational waves at the algebraically special frequency," *Phys. Rev. D* **62** (2000) , gr-qc/0001032. (Cited on pages 34, 35, 38 and 51.)

[130] P. T. Leung, A. Maassen van den Brink, K. W. Mak, and K. Young, "Unconventional Gravitational Excitation of a Schwarzschild Black Hole," *Class.Quant.Grav.* **20** (2003) L217, gr-qc/0301018. (Cited on pages 35, 38 and 51.)

[131] H. Onozawa, "A detailed study of quasinormal frequencies of the Kerr black hole," *Phys.Rev. D* **55** (1997) 3593–3602, gr-qc/9610048. (Cited on page 51.)

[132] H. Bateman and A. Erderlyi, *Higher Transcedental Functions*, vol. 2. McGraw-Hill Inc., NY Toronto London. (Cited on page 66.)

[133] D. Staicova and P. Fiziev, "New results for electromagnetic quasinormal modes of black holes," (2011) , arXiv:1112.0310 [astro-ph.HE]. (Cited on pages 71 and 100.)

[134] G. Dotti, R. J. Gleiser, I. F. Ranea-Sandoval, and H. Vucetich, "Gravitational instabilities in Kerr spacetimes," *CQG* **25** (2008) 245012, arXiv:0805.4306 [gr-qc]. (Cited on page 75.)

[135] Y. B. Zel'dovich, "Generation of Waves by a Rotating Body," *Sov. Phys. JETP Lett* **14** (1971) 180. (Cited on page 76.)

[136] Y. B. Zel'dovich, "Amplification of Cylindrical Electromagnetic Waves Reflected from a Rotating Body," *Sov. Phys. JETP* **35** (1972) 1085. (Cited on page 76.)

[137] A. A. Starobinskiy, "Amplification of waves during reflection from a rotating 'black hole'," *Sov. Phys. JETP* **64** (1973) 49. (Cited on page 76.)

[138] A. A. Starobinskiy and S. M. Churilov, "Amplification of electromagnetic and gravitational waves scattered by a rotating black hole," *Sov. Phys. JETP* **65** (1973) 3–11. (Cited on page 76.)

[139] V. Cardoso, O. J. Dias, J. P. Lemos, and S. Yoshida, "Black-hole bomb and superradiant instabilities," *Phys. Rev. D* **70** (2004) 044039, hep-th/0404096. (Cited on page 77.)

[140] E. Berti and K. D. Kokkotas, "Asymptotic quasinormal modes of Reissner-Nordström and Kerr black holes," *Phys.Rev.D* **68** (2003) 044027, hep-th/0303029. (Cited on page 78.)

[141] M. Cadoni and P. Pani, "Holography of charged dilatonic black branes at finite temperature," *JHEP* **1104:049** (2011) , arXiv:1102.3820 [hep-th]. (Cited on page 102.)

[142] P. Pani, *Applications of perturbation theory in black hole physics.[Doctoral Thesis]*. PhD thesis, 2011. http://veprints.unica.it/553/. (Cited on page 102.)

[143] I. Newton, *Methodus fluxionum et serierum infinitarum*. Paris, Hermann, 1664-1671. (Cited on page 87.)

[144] J. Raphson, *Analysis aequationum universalis*. London, 1690. (Cited on page 87.)

[145] W. H. Press, S. A. Teukolsky, W. T. Vetterling, and B. P. Flannery, *Numerical Recipes*. Cambridge University Press, Cambridge, England, 1992. (Cited on pages 87, 88, 89 and 93.)

[146] G. E. Forsythe, M. A. Malcolm, and C. B. Moler, *Computer Methods for Mathematical Computations*. Prentice Hall (Prentice-Hall series in automatic computation), 1977. (Cited on page 87.)

[147] C. G. Broyden, "A Class of Methods for Solving Nonlinear Simultaneous Equations," *Math. Comput.* **19** (1965) 577–593. (Cited on page 88.)

[148] C. Grosan and A. Abraham, "New Approach for Solving Nonlinear Equations Systems,". (Cited on page 88.)

[149] M. Hirsch, P. Pardalos, and M. Resende, "Solving systems of nonlinear equations with continuous grasp," tech. rep., AT&T Labs Research Technical Report TD-6V6JCX, Shannon Laboratory, Florham Park,NJ 0793, November, 2006. (Cited on page 88.)

[150] D. E. Müller, "A Method for Solving Algebraic Equations Using an Automatic Computer," *MTAC* **10** (1956) 208–215. (Cited on pages 88 and 89.)

[151] L. R. Burden and D. Faires, *Numerical Analysis (7th ed.)*. Pacific Grove, CA: Brooks/Cole, ISBN 0534382169, 2001. (Cited on page 93.)

Scientific contributions

1. The spectrum of electromagnetic primary jets of rotating black holes and naked singularity is found using the exact analytical solutions of the Teukolsky angular and the Teukolsky radial equations in terms of confluent Heun functions. The perturbations remain stable for both rotating black holes and naked singularities.

2. It was shown that the two lowest modes of the jets-spectrum can be described with very high precision by previously found by Fiziev analytical formula deduced from the properties of the confluent Heun functions.

3. The quasi-normal modes spectrum of gravitational perturbations on the Schwarzschild metric has been found using the exact analytical solutions of the Regge-Wheeler equation. The so-obtained spectra matches with high precision already published results, evaluated trough different methods. Additionally, the same spectrum has been calculated from the exact analytical solutions of the Teukolsky radial equation for the first time.

4. The quasi-normal modes spectrum of rotating black hole has been obtained by solving two-dimensional spectral system of transcendental equations featuring the confluent Heun functions. For the first time, trough the exact solutions of the radial equation has been explored the dependence of those solutions and their spectra with respect to the branch cuts in those radial solutions. A new method for studying those branch cuts in the complex r-plane has been introduced.

5. A new algorithm for solving complex two-dimensional systems of transcendental equations has been developed and test in a number of non-physical and physical problems.

Publications:

In journals with impact factor:

1. Fiziev, P. P. and Staicova, D. R., *Application of the confluent Heun functions for finding the quasinormal modes of nonrotating black holes*, Phys. Rev. D. **84**, 127502 (2011), arXiv:1109.1532 [gr-qc] (2011)

2. Staicova, D. and Fiziev, P. ,*"The Spectrum of Electromagnetic Jets from Kerr Black Holes and Naked Singularities in the Teukolsky Perturbation Theory"*, Astrophys Space Sci. **332**: 385-401, arXiv:1002.0480v2 [astro-ph.HE] (2011)

3. Fiziev, P. P. and Staicova, D. R., *"A new model of the Central Engine of GRB and the Cosmic Jets"*, Bulg. Astr. Jour. **11**:3, arXiv:0902.2408 [atro-ph.HE], (2009)

4. Fiziev, P. P. and Staicova, D. R., *Toward a New Model of the Central Engine of GRB*, Bulg. Astr. Jour. **11**:13, arXiv:0902.2411 [astro-ph.HE], (2009)

E-prints:

1. Fiziev, P. and Staicova, D., *Solving systems of transcendental equations involving the Heun functions.*, arXiv:1201.0017v1 [cs.NA]

2. Staicova D. and Fiziev P., *New results for electromagnetic quasinormal modes of black holes*, arXiv:1112.0310v2 [astro-ph.HE];

3. Fiziev, P. and Staicova, D., *Two-dimensional generalization of the Muller root-finding algorithm and its applications*, arXiv:1005.5375v2 [cs.NA], (2010)

Participation at international conferences with a report:

1. "Understanding the Central Engine of GRB" (Talk at JINR, Dubna, BLTP seminar, 23th July 2009)

2. "The Spectrum of Electromagnetic Jets from Kerr Black Holes and Naked Singularities in the Teukolsky Perturbation Theory" (Talk at GR19, 5-9 July, 2010, Mexico)

3. "Solving systems of transcendental equations involving the Heun functions." (Talk at Spanish Relativity Meeting ERE2011, August 29, Madrid, 2011)

For the presentations, please see http://tcpa.uni-sofia.bg/research/.

Participation at local conferences with a report:

1. "New root-finding algorithm for systems of complex-valued equations and its application in astrophysics", talk at the Meetings in Physics, 2009

2. "Application of the confluent Heun functions in understanding the central engine of GRB", talk at the IRC-CoSiM Second Workshop, Gyulechica, 2009

3. "The Spectrum of Electromagnetic Jets from Kerr Black Holes and Naked Singularities in the Teukolsky Perturbation Theory", a IRC-CoSiM seminar, Sofia, 2010,

4. "The Spectrum of Electromagnetic Jets from Kerr Black Holes and Naked Singularities in the Teukolsky Perturbation Theory", talk at 'Trends in Particle Physics - Primorsko 2010', 2010

5. "Two-dimensional generalization of the Muller root-finding algorithm and its applications", talk at the 4th IRC-CoSIM Workshop, Tryavna, 2011